


Technische Universität München
Max-Planck-Institut für Physik


Dissertation

Measuring and Simulating Muon-Induced Neutrons in Lead and Copper at Shallow Depth

Raphael Kneißl

München, 2019

Technischen Universität München
Fakultät für Physik

Max-Planck-Institut für Physik
(Werner-Heisenberg-Institut)

Measuring and Simulating Muon-Induced Neutrons in Lead and Copper at Shallow Depth

Raphael Benedikt Kneißl

Vollständiger Abdruck der von der Fakultät für Physik der Technischen Universität München zur Erlangung des akademischen Grades eines

Doktors der Naturwissenschaften (Dr. rer. nat.)

genehmigten Dissertation.

Vorsitzender:	Prof. Dr. A. Ibarra
Prüfer der Dissertation:	1. Priv.-Doz. Dr. B. Majorovits
	2. Prof. Dr. L. Oberauer

Die Dissertation wurde am 21.03.2019 bei der Technischen Universität München eingereicht und durch die Fakultät für Physik am 07.05.2019 angenommen.

Abstract

A detailed understanding of all radiation backgrounds is crucial for the next generation of beyond standard model physics low-background experiments. Muon-induced neutrons are an important source of radiation background. Up to now, simulation tools do not reproduce the experimental findings of muon-induced neutrons consistently and reliably enough. The MINIDEX (Muon-Induced Neutron Indirect Detection EXperiment) project was initiated to help to improve Monte Carlo tools with respect to muon-induced neutrons, by providing experimental data sets that can be used to evaluate and gauge them. MINIDEX is located at the Tübingen Shallow Underground Laboratory, which yields a vertical shielding depth of (13.2 ± 0.8) meter water equivalent at the position of the setup. Neutrons induced by cosmogenic muons in the high-Z materials lead and copper were measured at a mean muon energy of (8.7 ± 0.2) GeV and (8.5 ± 0.2) GeV, respectively. The neutrons are identified with the help of two high-purity germanium detectors that measure 2.2 MeV gammas from neutron captures on hydrogen in a water tank.

Geant4 Monte Carlo simulations of the MINIDEX setup were carried out and the predictions were compared to the experimental observations. Good agreement between the measured and the predicted 2.2 MeV neutron capture gamma rate was found for lead. Based on this agreement, an external neutron yield of $(7.2\,^{+\,0.7}_{-\,0.6}) \cdot 10^{-5}\,\mathrm{g}^{-1}\,\mathrm{cm}^2$ neutrons per tagged muon was determined for lead with the help of Geant4. The measured rate of 2.2 MeV neutron capture gammas for copper was found to be by a factor of 0.72 ± 0.14 lower than the predicted rate. Taking this factor into account, an external neutron yield of $(2.1 \pm 0.4) \cdot 10^{-5}\,\mathrm{g}^{-1}\,\mathrm{cm}^2$ neutrons per tagged muon was determined for copper. Also, the measured and predicted rate of events, for which more than one 2.2 MeV neutron capture gamma was detected for the same tagged muon, was compared for lead. This comparison hints towards a too high multiplicity of neutrons that are directly emitted in muon-nuclear inelastic scattering reactions in Geant4.

In order to cross-check the Geant4 results for lead, they were compared to the predictions of a complementary simulation made with the FLUKA Monte Carlo tool. It was observed that also FLUKA predicts the measured 2.2 MeV neutron capture gamma rate for lead well. The Geant4 and FLUKA predictions for muon interactions and the subsequent production of neutrons in lead at a mean muon energy of (8.7 ± 0.2) GeV were compared in detail. Large discrepancies in the description of photo-nuclear and muon-nuclear inelastic scattering reactions were identified. These results point towards an underprediction of the neutron

production in photo-nuclear inelastic scattering reactions in Geant4. At the same time it seems that Geant4 overpredicts the neutron production in muon-nuclear inelastic scattering reactions. Furthermore, the simulation comparison study strengthens the hints for an imprecise description of the multiplicity of neutrons directly emitted in muon-nuclear inelastic scattering reactions in Geant4.

Zusammenfassung

Ein genaues Verständnis des Strahlungsuntergrunds ist wesentlich für die nächste Generationen von untergrundarmen Experimenten zur Suche nach Physik jenseits des Standardmodells. Myonen-induzierte Neutronen tragen zu diesem Untergrund bei. Jedoch beschreiben Simulationen die Messungen solcher Neutronen nicht zuverlässig. Das MINIDEX (Muon-Induced Neutron Indirect Detection EXperiment) Projekt wurde initiiert, um die Vorhersagen von Monte-Carlo-Programmen im Bezug auf Myonen-induzierte Neutronen zu überprüfen und zu verbessern. Der MINIDEX Aufbau befindet sich in einem Untergrundlabor in Tübingen, welches an der Position des Experiments eine vertikale Abschirmtiefe von (13.2 ± 0.8) Meter Wasseräquivalent bietet. Neutronen, induziert durch kosmogene Myonen in den Materialien Blei und Kupfer, wurden bei einer mittleren Myonenenergie von $(8.7 \pm 0.2)\,\mathrm{GeV}$ beziehungsweise $(8.5 \pm 0.2)\,\mathrm{GeV}$ gemessen. Die Identifikation der Neutronen geschieht mit Hilfe von zwei hochreinen Germaniumdetektoren. Diese messen Gammaquanten mit einer Energie von 2.2 MeV, welche beim Einfang von Neutronen an Wasserstoff innerhalb eines die Detektoren umgebenden Wassertanks entstehen.

Geant4 Monte-Carlo-Simulationen des MINIDEX Aufbaus wurden durchgeführt und deren Vorhersagen mit den experimentellen Beobachtungen verglichen. Für Blei wurde eine gute Übereinstimmung zwischen der gemessenen und der simulierten Rate an 2.2 MeV Gammaquanten gefunden. Basierend auf dieser Übereinstimmung wurde für Blei mit Hilfe von Geant4 eine Anzahl von $(7.2\,^{+\,0.7}_{-\,0.6}) \cdot 10^{-5}\,\mathrm{g}^{-1}\,\mathrm{cm}^2$ emittierten Neutronen pro identifiziertem Myon ermittelt. Für Kupfer wurde eine gemessene Rate an 2.2 MeV Gammaquanten bestimmt, welche um einen Faktor 0.72 ± 0.14 niedriger ist als die von der Simulation vorhergesagte. Unter Berücksichtigung dieser Diskrepanz wurde für Kupfer eine Anzahl von $(2.1 \pm 0.4) \cdot 10^{-5}\,\mathrm{g}^{-1}\,\mathrm{cm}^2$ emittierten Neutronen pro identifiziertem Myon ermittelt. Zusätzlich wurde für Blei die gemessene und die vorhergesagte Rate an Ereignissen, für welche mehr als ein 2.2 MeV Gammaquant für das selbe identifizierte Myon detektiert wurden, verglichen. Dieser Vergleich deutet auf eine zu hohe Multiplizität an Neutronen in Geant4 hin, welche direkt in inelastischen Streuungen von Myonen an Atomkernen emittiert werden.

Um die Geant4-Ergebnisse für Blei zu überprüfen, wurden diese mit den Vorhersagen einer ergänzenden Simulation des Monte-Carlo-Programms FLUKA verglichen. Auch für FLUKA wurde für Blei eine gute Übereinstimmung zwischen der vorhergesagten und der gemessenen Rate an 2.2 MeV Gammaquanten gefunden. Geant4- und FLUKA-Vorhersagen für die Wechselwirkungen von My-

onen in Blei und die darauffolgende Produktion von Neutronen bei einer mittleren Myonenenergie von (8.7 ± 0.2) GeV wurden im Detail verglichen. Es wurden signifikante Unterschiede in der Beschreibung der inelastischen Streuung von Photonen sowie Myonen an Atomkernen festgestellt. Diese Unterschiede deuten auf eine unterschätzte Neutronenproduktion in inelastischen Streuungen von Photonen an Atomkernen in Geant4 hin. Gleichzeitig scheint es, dass Geant4 die Neutronenproduktion in inelastischen Streuungen von Myonen an Atomkernen überschätzt. Darüber hinaus bestärkt die Simulationsstudie die Hinweise auf eine ungenaue Beschreibung der Multiplizität von Neutronen in Geant4, welche direkt in inelastischen Streuungen von Myonen an Atomkernen emittiert werden.

Contents

Introduction

There are currently various open questions in particle physics, including the nature of neutrinos and dark matter. To tackle these and further open questions, different low-background experiments are searching for rare event processes like neutrinoless double beta decay or direct dark matter interactions. In order to build the next generation of low-background experiments, which will have significantly increased sensitivities, a large reduction of the radiation backgrounds is necessary. All current and future low-background experiments are located in deep underground laboratories, reducing the cosmogenic muon flux by many orders of magnitude. Muons that reach an experiment lead to the production of various particles in the surroundings (e.g. cavern rock or laboratory concrete) and the experimental setup itself. A critical source of radiation backgrounds results from muon-induced neutrons, which are becoming increasingly important. Muon-induced neutrons can have energies up to several GeV and are therefore able to overcome large distances. Typically high-Z materials like lead and copper are used to shield the target detectors from ambient background radiation. As these shielding materials are often located in the vicinity of the target detectors, they act as a close-by source of muon-induced neutrons. Muon-induced neutrons can directly interact with the target detectors and thus lead to prompt signals. If the muon or any muon-induced particle is detected with one of the installed veto systems, these prompt signals can be rejected. However, muon-induced neutrons can also lead to the production of radioactive isotopes by neutron capture or inelastic scattering reactions. If the time correlation to the original muon is lost, the decays of these isotopes can result in backgrounds.

The reduction of backgrounds from muon-induced neutrons depends on a precise understanding of them. Typically, simulation tools are used to predict the background contributions of muon-induced neutrons. However, current Monte Carlo (MC) tools do not consistently and reliably enough reproduce the experimental findings of muon-induced neutrons. Consequently, large uncertainties have to be assigned to the predicted quantities, like the total number of produced neutrons as well as their energy distribution. To improve the predictive power of MC tools for muon-induced neutrons, reliable experimental data sets of them are

needed. As these data sets are quite rare, the MINIDEX (Muon-Induced Neutron Indirect Detection EXperiment) project was initiated [1]. MINIDEX is operated at the Tübingen Shallow Underground Laboratory at a vertical shielding depth of (13.2 ± 0.8) meter water equivalent[1] (mwe). The aim of the MINIDEX project is to measure muon-induced neutrons that are produced in different high-Z materials. The acquired experimental data sets are then used to evaluate the predictions of MC tools. Observed discrepancies between measured and simulated observables of MINIDEX can therefore help to improve the predictive power of the MC tools.

Several experimental runs, successfully measuring muon-induced neutrons, have been performed since the commissioning of MINIDEX in 2015. In the context of this thesis MINIDEX Run 2, Run 3 and Run 4 were carried out and the acquired data sets analysed. Muon-induced neutrons from lead have been measured in Run 2, while Run 3 allowed for a simultaneously measurement of lead and copper. The muon-induced neutrons of Run 2 and Run 3 result from through-going muons. In Run 4 the measurement of muon-induced neutrons from muon captures on lead was accomplished. Geant4-based MaGe simulations were performed for the different MINIDEX runs and the simulation predictions were compared to the experimental observations. Note that if not stated explicitly all simulations presented within this thesis were performed with Geant4.

In order to cross-check the Geant4 results for lead, they were compared to the predictions of a complementary simulation of the MINIDEX Run 2 setup with the FLUKA MC tool. A detailed comparison of muon-interactions and the subsequent neutron production in lead was performed for Geant4 and FLUKA. Note that all FLUKA simulations within the context of this thesis and the MINIDEX project were carried out separately [2].

This thesis is structured the following way: In Chapter 1 a short introduction to neutrinoless double beta decay and dark matter, including experimental searches, is given. Chapter 2 discusses the different backgrounds in underground physics experiments, focusing on muon-induced neutrons. In Chapter 3 the MC toolkit Geant4 and its reliability for muon-induced neutrons is discussed. Furthermore, the general concept of the neutron yield and its different definitions are introduced. In Chapter 4 the experimental setup, the working principle and the detectors of the MINIDEX setup are presented. Chapter 5 discusses the characterisation of the MINIDEX detectors, the data selection and the acquired

[1]The term meter water equivalent is an often used quantity to express the shielding depth of an underground laboratory in terms of a water depth. It is calculated as the product of the laboratory depth and the corresponding average overburden density.

experimental data sets. The MINIDEX Geant4 simulation predictions are presented in Chapter 6, while the strategy to determine the measured observables is introduced in Chapter 7. In Chapter 8 the measured and Geant4 simulated results are discussed, including their systematic uncertainties. A detailed comparison of Geant4 and FLUKA predicted muon-interactions and the subsequent neutron production is presented in Chapter 9. Chapter 10 gives a brief introduction to the measurement and the corresponding simulation study of muon-induced neutrons in MINIDEX that result from muon captures on lead. Finally, Chapter 11 gives a summary as well as an outlook to the future of MINIDEX.

Chapter 1

Rare Event Searches in Particle Physics

The standard model (SM) of particle physics was established throughout the 20th century. It successfully describes the elementary particles as well as the interactions between them. Furthermore, it can precisely explain most experimental observations and phenomena in particle physics. In July 2012, the discovery of the Higgs boson at the Large Hadron Collider by the CMS and ATLAS experiments showed again the success of the SM [3, 4].

Although the SM describes subatomic particles and processes to a remarkable precision, it has some serious shortcomings. Various experimental observations require an extension of the SM. An example for such an observation is the discovery of neutrino oscillations. The neutrino, postulated by Pauli in 1930 and detected experimentally for the first time in 1956, is massless in the SM. Nevertheless, from the observation of neutrino oscillations it became clear that neutrinos must have a finite (but up to now unknown) rest mass. Another example is the strong evidence for the existence of dark matter. Within the SM there is no explanation of the nature of non-baryonic dark matter.

To tackle these and further open questions, over the last decades various theories have been put forward and experiments have been planned and built trying to confirm them. Among them are searches for the neutrinoless double beta ($0\nu\beta\beta$) decay and for WIMP dark matter. In the following, a brief introduction to these searches is given. This includes the motivation, the experimental strategies as well as a selection of experiments and their results.

1.1 Neutrinoless Double Beta Decay

Since the postulation of the neutrino, three generations (electron, muon and tau neutrinos) have been experimentally detected. Neutrinos in the SM are massless spin 1/2 fermions. However, experiments that investigate neutrino oscillations showed that neutrinos are not massless. These experiments only provide information on Δm^2_{21}, Δm^2_{31} and Δm^2_{32}. Here Δm^2_{ij} represents the mass square differences, $m^2_i - m^2_j$, of the three neutrino mass eigenstates (m_1, m_2 and m_3). This means that from oscillation experiments the absolute mass scale of neutrinos can not be determined. Furthermore, up to now only the sign of Δm^2_{21} could be determined and was found to be positive [5]. This leads to the possibility of two different mass orderings. The so-called normal ordering,

$$m_1 < m_2 < m_3 \quad \text{with} \quad \Delta m^2_{21} \ll \Delta m^2_{32} \tag{1.1}$$

and the inverted ordering

$$m_3 < m_1 < m_2 \quad \text{with} \quad \Delta m^2_{21} \ll |\Delta m^2_{31}|. \tag{1.2}$$

Up to now it was neither possible to experimentally determine the absolute values of the neutrino masses nor their ordering. The search for $0\nu\beta\beta$ decay helps to tackle these open questions as well as further ones (e.g. if the neutrino is its own antiparticle or if the lepton number can be violated).

1.1.1 Physics of the Neutrinoless Double Beta Decay

Neutrino accompanied double beta ($2\nu\beta\beta$) decay is a second order weak nuclear process allowed in the SM of particle physics. In this process two neutrons in a nucleus are converted coherently into two protons under the emission of two electrons (e^-) and two electron-antineutrinos ($\bar{\nu}_e$):

$$(\mathrm{Z}, \mathrm{A}) \longrightarrow (\mathrm{Z}+2, \mathrm{A}) + 2e^- + 2\bar{\nu}_e, \tag{1.3}$$

where A is the mass number and Z the atomic number of the nucleus. As $2\nu\beta\beta$ decay is a second order weak process, the single β decay has to be energetically forbidden or strongly suppressed to observe it for a given isotope. This can be the case if an odd-odd nucleus (Z $\pm$ 1,A) is the neighbour of an even-even nucleus (Z,A) that is stronger bound due to the pairing interaction. The mass of odd-odd and even-even nuclei with a fixed A lie on a parabolically shaped curve. This is shown for the case of A = 76 in Fig. 1.1. It can be seen that single beta decay from

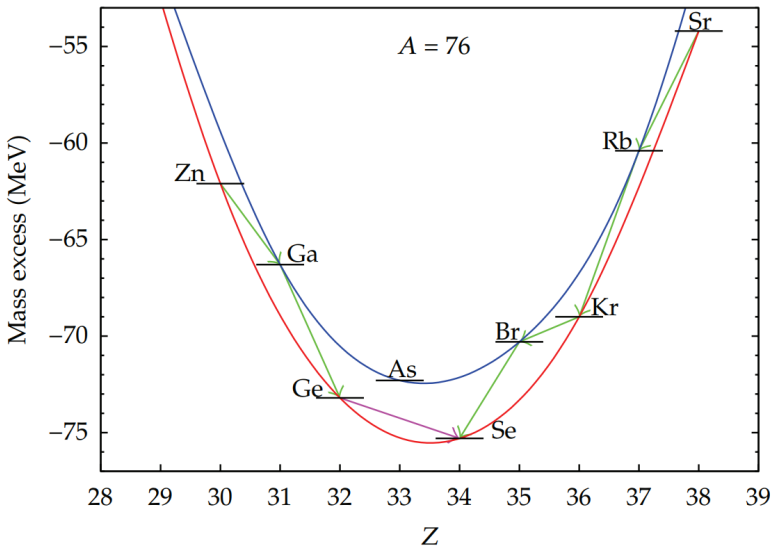

Figure 1.1: Mass parabola for nuclei with mass number of 76 together with the allowed single beta decays (green arrows). The existence of two mass parabolas results from the pairing interaction, as even-even nuclei (red parabola) have a higher binding energy compared to odd-odd ones (blue parabola). Taken from [6].

^{76}Ge to ^{76}As is energetically forbidden. However, double beta decay, indicated by a pink arrow, is allowed.

In addition to $2\nu\beta\beta$ decay there could be a neutrinoless mode of double beta decay, which was proposed by Ettore Majorana in 1937 [7]. In this lepton number violating process, called neutrinoless double beta ($0\nu\beta\beta$) decay and described by

$$(\mathrm{Z}, \mathrm{A}) \longrightarrow (\mathrm{Z}+2, \mathrm{A}) + 2e^{-}, \tag{1.4}$$

no neutrinos are emitted. In Figure 1.2 the Feynman diagrams for $2\nu\beta\beta$ decay (a) and $0\nu\beta\beta$ decay (b) are shown. In the neutrinoless case a light Majorana neutrino (ν_{M}) is exchanged. In principle other lepton number violating processes can lead to $0\nu\beta\beta$ decay. However, the exchange of a light Majorana neutrino is amongst the discussed mechanism the most popular one [8]. The neutrinoless case violates lepton number conservation by two units. It can only occur if neutrinos have a mass and if they are their own antiparticles (i.e. they have Majorana nature). This process is not allowed by the SM and has not been observed until today.

The total decay rate of $0\nu\beta\beta$ decay, $\Gamma^{0\nu}$, in the case of a light Majorana neutrino mediator can be expressed in the following way [9]:

$$\Gamma^{0\nu} = \frac{1}{T^{0\nu}_{\frac{1}{2}}} = |m_{\beta\beta}|^2 \; |M^{0\nu}|^2 \; G^{0\nu}(Q_{\beta\beta}, \mathrm{Z}). \tag{1.5}$$

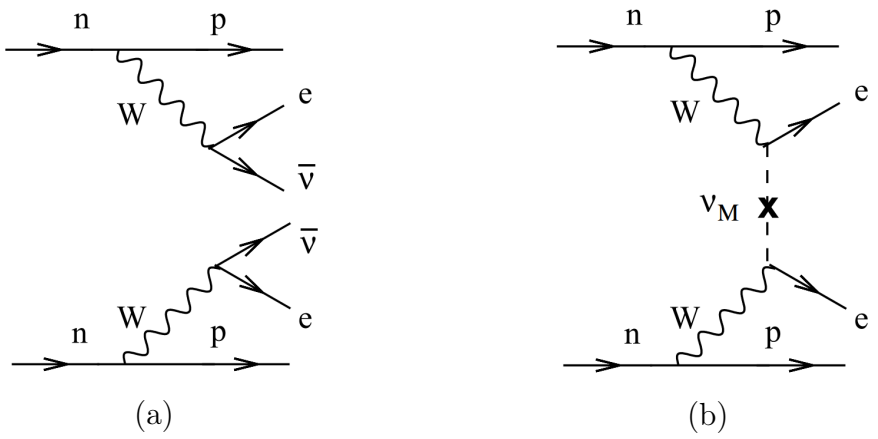

Figure 1.2: Feynman diagrams of neutrino accompanied double beta decay (a) and neutrinoless double beta decay (b). Taken from [8].

Here $T^{0\nu}_{\frac{1}{2}}$ represents the half-life of the $0\nu\beta\beta$ decay, $m_{\beta\beta}$ the effective Majorana neutrino mass, $M^{0\nu}$ the nuclear matrix element and $G^{0\nu}(Q_{\beta\beta}, \mathrm{Z})$ the phase space factor. $G^{0\nu}(Q_{\beta\beta}, \mathrm{Z})$ can be precisely calculated and is proportional to ${Q_{\beta\beta}}^5$ [8]. In contrast to this, $M^{0\nu}$ has to be approximated through nuclear models. Typically, different models are used for this purpose. As the individual models yield different results, this introduces uncertainties up to a factor of 3 [10]. The term $m_{\beta\beta}$ is the sum of the neutrino mass eigenstates (m_i) and the corresponding elements of the Pontecorvo-Maki-Nakagawa-Sakata matrix corresponding (U_{ei}) [11, 12]. It can be written as

$$m_{\beta\beta} = \left| m_1 |U^2_{e1}| + m_2 |U^2_{e2}| e^{i(\alpha_2 - \alpha_1)} + m_3 |U^2_{e3}| e^{i(-\alpha_1 - \delta_{CP})} \right|. \tag{1.6}$$

The α_i stand for the two Majorana phases whereas δ_{CP} for the Dirac CP-violating phase. The $0\nu\beta\beta$ decay rate is therefore related to the absolute neutrino mass scale and the neutrino mass hierarchy. Further, it can be seen that non-zero Majorana phases influence the $0\nu\beta\beta$ decay rate. The resulting dependencies of $m_{\beta\beta}$ on the smallest neutrino mass (m_{min}) for the two possible hierarchies are shown in Fig. 1.3. Further, an experimental upper limit on $m_{\beta\beta}$ as well as a cosmological constraints on m_{min} are indicated [13].

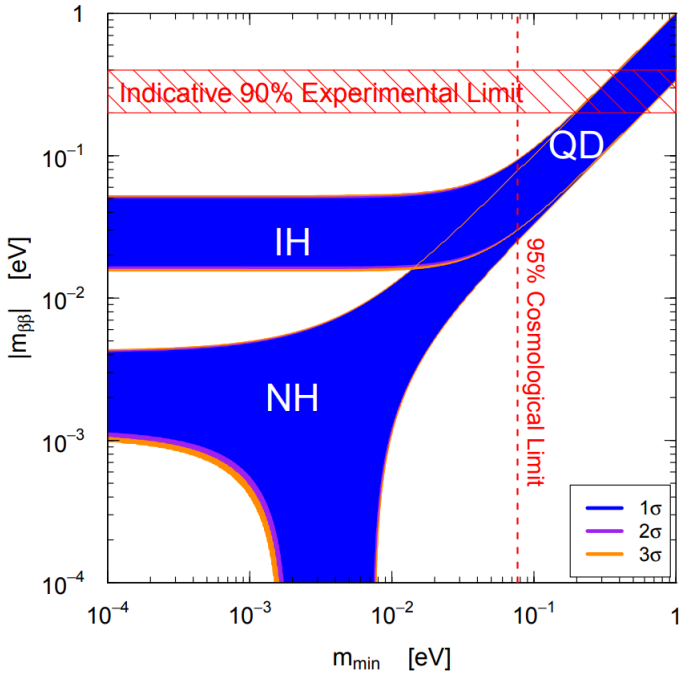

Figure 1.3: Allowed parameter space for the effective Majorana neutrino mass ($m_{\beta\beta}$) as a function of the smallest neutrino mass (m_{min}). The allowed regions for the two different cases are shown: the inverted (IH) and normal (NH) neutrino mass hierarchy. In the quasi-degenerate case (QD) the neutrino mass differences are much smaller than the neutrino masses themselves. The width of the depicted bands is dominated by the unknown Majorana phases. The experimental upper bound on $m_{\beta\beta}$ and the cosmological constraints on m_{min} are depicted as well. The experimental limit of $m_{\beta\beta}$ is depicted as a band, which arises due to the uncertainty on $M^{0\nu}$. Taken from [14].

1.1.2 Experimental Search for Neutrinoless Double Decay

As was described in Section 1.1.1, various open questions concerning neutrinos can be investigated by searching for $0\nu\beta\beta$ decay. The goal of experiments searching for $0\nu\beta\beta$ decay is to measure its half-life. In the following, the requirements and strategies on the searches for this decay are discussed.

For an experiment that searches for $0\nu\beta\beta$ decay a suitable isotope has to be chosen. A total of 35 different nuclei have been identified for which $2\nu\beta\beta$ decay can be potentially observed [15]. Up to now this process has been identified for 11 of them [16]. The selected isotope should either have a high natural isotopic abundance or its enrichment should be applicable. A high $Q_{\beta\beta}$ is preferable as the phase space factor $G^{0\nu}(Q_{\beta\beta}, \text{Z})$ scales with $Q^5_{\beta\beta}$. Also in terms of potentially background sources, a Q-value above the Compton edge of the 2.6 MeV gamma line of ^{208}Tl, which is $\approx$2.4 MeV, is of advantage. The availability of the isotope

is important, especially for future experiments for which large target masses are required.

The expected signal, in the case of a $0\nu\beta\beta$ decay, is the full energy deposition of $Q_{\beta\beta}$ in the detectors. In Fig. 1.4 the summed energy spectrum of the two released electrons (including the energy of the recoiling nucleus) is schematically depicted for $0\nu\beta\beta$ decay (red) and $2\nu\beta\beta$ decay (blue) of ^{76}Ge. The pursued way of experiments searching for the neutrinoless mode is to measure events in the region of interest (ROI) around $Q_{\beta\beta}$.

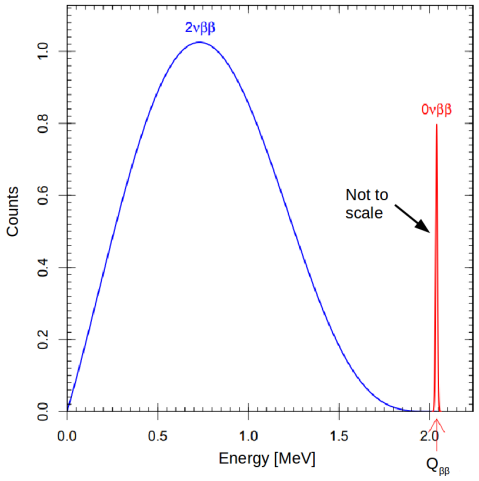

Figure 1.4: Energy spectra of the summed kinetic energy of electrons emitted in $2\nu\beta\beta$ decay (blue) and $0\nu\beta\beta$ decay (red) of ^{76}Ge. The spectrum of $2\nu\beta\beta$ decay is continuous, as in addition to the electrons also two neutrinos are emitted (escaping the detector). In the case of $0\nu\beta\beta$ decay of ^{76}Ge a narrow peak at $Q_{\beta\beta}$ is expected (peak not to scale). Taken from [14].

From the number of observed events in the ROI, in the case of non-zero background level in the ROI, the detector sensitivity $S^{0\nu}$ is given by [14]:

$$S^{0\nu} = \ln 2 \, \frac{N_A}{M_A} \, \kappa \, \epsilon \sqrt{\frac{Mt}{B\Delta E}} \text{ (at 68 \% confidence level).} \tag{1.7}$$

Here $S^{0\nu}$ is the half-life of the $0\nu\beta\beta$ decay process that would produce the same number of events as expected from an upward background fluctuation at the $1\,\sigma$ level. Further, N_A represents Avogadro's number, M_A the atomic mass of the isotope, κ the mass fraction of the double beta decaying isotope and ϵ the signal detection efficiency (includes the active volume fraction of the detector). Also included in the formula are the total mass of the source material (M), the measurement time (t), the background index (B, typically expressed in counts per

(keV kg yr)) and the ROI (ΔE, depends on the energy resolution of the detector). This formula shows that the sensitivity of an experiment can be improved by increasing the detector mass, a longer measurement time, by reducing the background rate in the ROI as well as by optimising the energy resolution.

In the case of an experiment with significantly less than one expected background event in the whole measurement time (often called "zero background" case), $S^{0\nu}$ can be determined by [14]:

$$S^{0\nu} = \ln 2 \, \frac{N_A}{M_A} \, \kappa \, \epsilon \, M \, t \text{ (at 68 \% confidence level).} \tag{1.8}$$

It can be seen that in the "zero background" case, $S^{0\nu}$ scales linearly with M and t.

Currently there are various experiments searching for $0\nu\beta\beta$ decay. For many of them, the decaying isotope is source and part of the detector at the same time. This is feasible if a detector can be build out of the double beta decaying isotope. In general, the advantage of this is a high detection efficiency. Different detector concepts and detection techniques are utilised, including semiconductors, bolometers and time projection chambers. Semiconductor detectors made out of germanium (enriched in ^{76}Ge) are used by the GERDA [17] and MAJORANA [18] experiments. CUORE [19] searches for $0\nu\beta\beta$ decay of ^{130}Te using TeO_2 bolometers. An example for an experiment utilising liquid ^{136}Xe as a time projection chamber is EXO-200 [20]. A further concept (for experiments in which the source is part of the detector) is to load liquid scintillators with a double beta decaying isotope. This technology is used by KamLAND-Zen [21] and SNO+ [22] experiments, which are searching for $0\nu\beta\beta$ decay of ^{136}Xe and ^{130}Te, respectively.

Another approach is to separate the double beta decaying isotope from a tracking detector. This allows to search for $0\nu\beta\beta$ decay in multiple isotopes at the same time. This approach is adopted by the NEMO-3 experiment [23], searching for $0\nu\beta\beta$ decay of isotopes like ^{100}Mo [24] and ^{150}Nd [25]. In NEMO-3 the deposited energy and the full event topology can be reconstructed, allowing to discriminate all background events without two electrons. However, compared to the approach in which the double beta decaying isotope is part of the detector, a lower detection efficiency has to be accepted.

The current best lower limits of $T^{0\nu}_{\frac{1}{2}}$ for the mentioned isotopes are (all at 90 % confidence level): $0.9 \cdot 10^{26}$ yr for ^{76}Ge [26], $1.5 \cdot 10^{25}$ yr for ^{130}Te [19], $1.07 \cdot 10^{26}$ yr for ^{136}Xe [27], $1.1 \cdot 10^{24}$ yr for ^{100}Mo [28] and $2.0 \cdot 10^{22}$ yr for ^{150}Nd [25]. These lower limits of $T^{0\nu}_{\frac{1}{2}}$ can be converted to upper limits of $m_{\beta\beta}$ using Eq. (1.5). The current best upper limits for $m_{\beta\beta}$ are in the range of

$\approx (50\text{ - }300)$ meV depending on the isotope and the chosen model for $M^{0\nu}$.

In order to further improve the lower limits on $T^{0\nu}_{\frac{1}{2}}$ and thus reduce the upper limits on $m_{\beta\beta}$ future experiments are planned. The near future goal of the upcoming experiments is to either measure $0\nu\beta\beta$ decay or to exclude at least the inverted neutrino mass hierarchy for the Majorana neutrino case. For such an exclusion the full mass range of $m_{\beta\beta}$ in the case of the inverted hierarchy (≈ 15 meV to ≈ 50 meV) has be fully covered (to account even for the most pessimistic nuclear matrix element models).

Examples of future experiments are LEGEND [29], nEXO [30], SNO+ [22] and SuperNEMO [31]. To improve the parameters of $S^{0\nu}$ (see Eq. (1.7)), significant research and development efforts are currently ongoing for each of these experiments. Special focus lies on an increase of the source mass in combination with a mitigation of the background in the ROI. As an example, LEGEND is planned to exploit up to 1 t of germanium, enriched in ^{76}Ge [29]. This is more than an order of magnitude more mass than currently used in the GERDA (≈ 35 kg) and MAJORANA (≈ 30 kg) experiments together. Furthermore, for LEGEND the goal is to reduce the background index in the ROI by a factor of ≈ 20. In general, to succeed such a significant background reduction, a plentitude of measures have to be undertaken. Among others, a careful material selection (e.g. only radiopure materials in the vicinity of the detectors), a special experimental design (e.g. instrumented active shielding materials) and the reduction of cosmogenic backgrounds (e.g. going deep into the underground and shielding materials during processing) are essential.

1.2 Dark Matter

The first evidence for the existence of dark matter in our universe was discovered in the early 1930s by Fritz Zwicky [32]. He determined the gravitational mass of galaxies in the Coma cluster and compared it to their luminous matter content. What he found was that the mass of the luminous matter is at least by a factor of ≈ 400 too small to explain the gravitational mass of the galaxies. From this observation he drew the conclusion that a huge part of the mass in the investigated galaxies must be dark. Since his discovery, compelling evidence for the existence of dark matter has been found on all cosmological scales of the universe. However, up to the present day its nature is still unknown.

In the following, some of the observations that lead to the convincing evi-

dence of dark matter are presented. Furthermore, WIMP (Weakly Interacting Massive Particle) dark matter as well as the direct search for this type of dark matter is introduced.

1.2.1 Evidence for Dark Matter

One evidence for the existence of dark matter comes from the observation of rotation curves of spiral galaxies. The orbital velocity, $v(r)$, of these galaxies is expected to follow Newtonian mechanics and can thus be described by the relation:

$$v(r) = \sqrt{\frac{GM(r)}{r}}. \tag{1.9}$$

Here G represents the gravitational constant, r the distance from the galactic centre and $M(r)$ the total mass of the galaxy within r. For the outer regions of most spiral galaxies, instead of the expected $r^{-0.5}$ behaviour (if only luminous matter would be present), a nearly constant orbital velocity is observed. This could be explained by a spherical halo of dark matter particles with a density function proportional to r^{-2} [33]. In Fig. 1.5 the rotation curve of the spiral dwarf galaxy NGC 6503 is depicted as an example, together with its individual components.

It should be noted that the observed behaviour of the orbital velocities of spiral galaxies could also be explained by the so-called Modified Newtonian Dynamics (MOND theories). These theories suggest that Newton's law of gravity does not hold on such large scales and thus needs to be modified [34].

Observations of galaxy cluster collisions strongly suggest the existence of dark matter and disfavour MOND theories. The most famous one is the so-called Bullet Cluster which is shown in Fig. 1.6. Its structures were formed by the collision of two smaller galaxy clusters [36]. After the collision two peaks of the gravitational potential are present (determined by gravitational lensing) which are shaded in blue. In contrast to this, it was observed that the position of hot X-ray emitting gas (shaded in red), which makes up most of the baryonic matter in the cluster, deviates from the observed gravitational centers. This can be explained by the slowing down of the intergalactic gas due to the friction during the collision of the clusters. The dark matter particles on the other hand moved without or with only few collisions through the other galaxy cluster. This leads to the conclusion that bulk of the dark matter particles only interacted gravitationally during the collision in contrast to the bulk of the intergalactic gas.

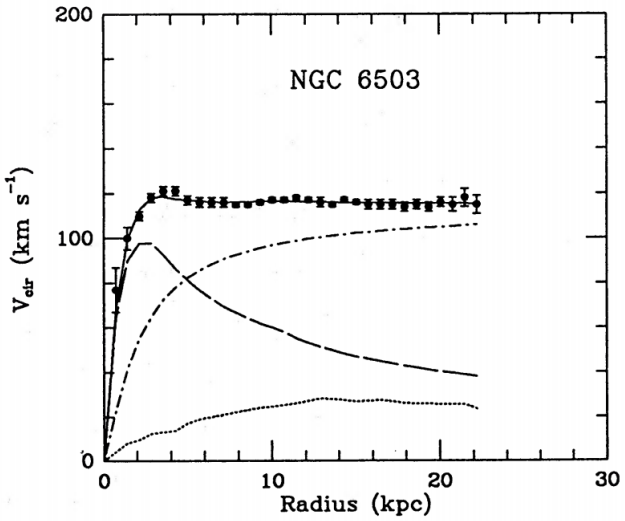

Figure 1.5: Measured rotation curve (points) of the spiral dwarf galaxy NGC 6503 together with a dark halo model fit (solid line). The contribution to the fit from the visible component (dashed line), the gas (dotted line) and the dark matter halo (dash-dotted line) are shown. Taken from [33].

Figure 1.6: Picture of the bullet cluster recorded in the optical spectrum. In addition the distribution of hot X-ray emitting gas is indicated in red whereas the gravitational potential is shaded in blue. A deviation between the bulk of baryonic matter and the gravitational centres can be observed. Taken from [35].

On cosmic scales further evidence for the existence of dark matter can be found by investigating the cosmic microwave background (CMB). The CMB is the radiation left over from the decoupling of photons and has an almost prefect black body spectrum with a temperature of 2.725 K [37]. The photons of the CMB arrive nearly isotropically from all directions of the sky. Nevertheless, small anisotropies of the temperature on the order of 10^{-5} were found. These anisotropies of the CMB are imprints of small matter inhomogeneities in the early universe. Various measurements of the CMB with satellites have been carried out over the last decades [38, 39]. The most precise one was achieved by the Planck satellite [40]. By analysing the power spectrum of anisotropies, information on the cosmological parameters can be derived. The best fit is obtained for the Λ-CDM model, which is the standard model of cosmology. According to this model, cold dark matter and dark energy[1] dominate the universe. The best fit results for the case in which 68.3 % of the total energy content in the universe originates from dark energy, 26.8 % from dark matter and 4.9 % from baryonic matter [40].

1.2.2 Weakly Interacting Massive Particle Dark Matter

According to the Λ-CDM model, the majority of the mass in galaxies and galaxy clusters consists of dark matter. From various observations multiple requirements on the possible particle candidates for dark matter can be derived. Through the analysis of the CMB anisotropies and big bang nucleosynthesis it can be concluded that dark matter particles have to be non-baryonic. In addition, they have to be non-relativistic in order to catalyse the structure formation in the early universe. In the case of thermally produced dark matter particles this means, that they have to be heavy (at least $\mathrm{GeV\,c^{-2}}$ masses [41]) as otherwise they would have been still relativistic at times of their decoupling in the early universe. Furthermore, they have to be stable or at least have a lifetime that is larger or similar to the age of the universe. Thermally produced dark matter particles can neither interact via the strong force nor via the electromagnetic force, as otherwise they would have been already observed by experiments [42]. The predicted abundance of the dark matter particles should be consistent with the observed mismatch.

One of the currently most favoured class of thermally produced dark matter particles are WIMPs. These type of dark matter particles only interact via gravitation and a further force, which is expected to be on the order of the weak force

[1] The nature of dark energy is totally unknown.

or lower. Different kinds of WIMP dark matter particles have been proposed with masses ranging from a few GeV c^{-2} to TeV c^{-2}.

1.2.3 Direct Detection of Weakly Interacting Massive Particles

In the direct detection approach for WIMPs, experiments search for the interaction of these particles with ordinary matter. The searched for signals are energy depositions in the detectors from the recoils of WIMPs scattering elasticly off the target nuclei. If WIMPs are detected an annual modulation of the signal rate on the order of a few percent is expected. This arises from the relative speed of the Earth through the non-rotating galactic dark matter halo, which has a density of $\approx 0.3\,\mathrm{GeV\,cm^{-3}}$ at the position of the Earth. Over the year the velocity of the Earth through the thermal dark matter halo varies due to a superposition of the orbital velocity of the solar system ($\approx 220\,\mathrm{km\,s^{-1}}$) around the galactic centre and the Earth orbiting the sun ($\approx 30\,\mathrm{km\,s^{-1}}$) [43].

Many experiments searching for WIMPs are based on one of two different detector types. The first are solid state cryogenic crystals which are operated at temperatures below 100 mK at the edge of superconductivity. Examples of used detector materials are germanium (e.g. EDELWEISS [44]) and calcium tungstate (e.g. CRESST-II [45]). The second type are liquid noble gas detectors that use xenon (e.g. XENON100 [46]) or argon (e.g. DarkSide [47]).

In the interaction of WIMPs with nuclei energy can be deposited in three different channels: Scintillation light, heat and ionisation. Most of the current and future experiments read out two of these channels in order to discriminate backgrounds. This is possible as electrons and gammas (background events) distribute their deposited energy differently in these channels compared to nuclear recoils of WIMPs. However, especially neutrons lead to a crucial background for direct WIMP dark matter experiments, as they deposit similar amounts of energy as expected from WIMPs and are difficult to identify.

Over the last decades various experiments participated in the search for WIMPs. In Fig. 1.7 the experimental results of different direct dark matter searches for elastic spin-independent WIMP-nucleon scattering are shown. The parameter space above each line was excluded by the corresponding experiment while islands represent signal claims. As can be seen, some experiments like DAMA claim to have observed a signal consistent with the WIMP hypothesis. DAMA results show the expected annual modulation of the interactions with dark matter particles [48]. However, other experiments like LUX excluded these

and further discovery claims[2] [50]. A possible explanation for these claims could be events from unexpected backgrounds. In general, the tension between claims and exclusion limits make the direct WIMP dark matter search a controversial and debatable subject.

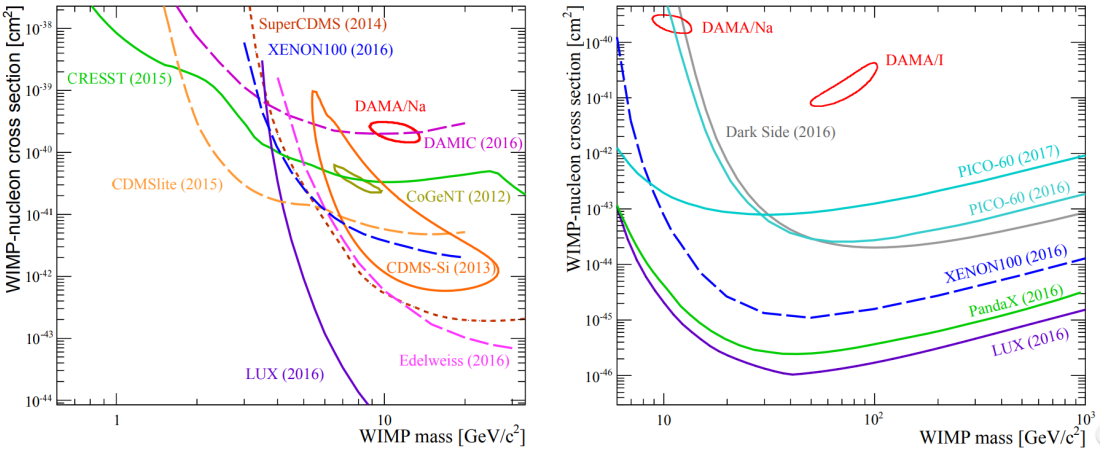

Figure 1.7: Summary of exclusion limits and discovery claims of the spin-independent WIMP-nucleon scattering cross section as of early 2017. The cross section is plotted against the WIMP mass. The parameter space above each line was excluded by the corresponding experiment. The depicted islands on the other hand represent observed signal claims. On the left the situation for low WIMP masses is depicted whereas on the right for high WIMP masses. Taken from [51].

[2]This only holds under specific assumptions. Examples are an elastically scattering of WIMPS off nuclei and a spin-independent scattering cross section which is similar for protons and neutrons [49].

Chapter 2

Backgrounds in Underground Physics Experiments

The sensitivity of an experiment to detect a signal depends significantly on the background level in the ROI. Figure 2.1 shows the sensitivity for a $0\nu\beta\beta$ decay discovery with germanium detectors (enriched in ^{76}Ge) as a function of the exposure for different background levels. Discovery means here that the signal from

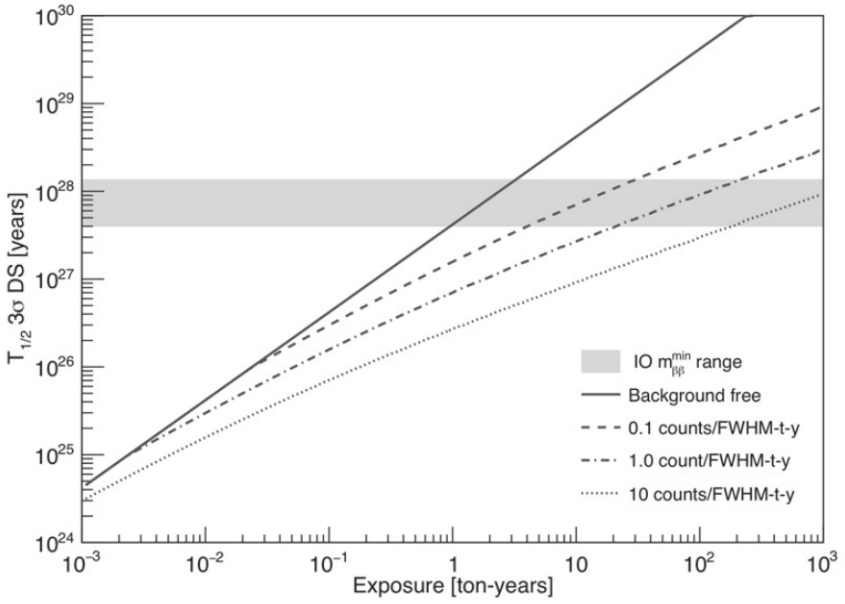

Figure 2.1: Sensitivity to observe a signal from $0\nu\beta\beta$ decay as a function of the exposure for an experiment using germanium detectors (enriched to 88 % in ^{76}Ge). A signal detection efficiency of 0.6 for the detectors is considered. The lines indicate the sensitivities for different background levels and the grey shaded area shows the mass range of $m_{\beta\beta}$ in the case of the inverted neutrino mass hierarchy and light Majorana neutrino exchange. Taken from [52].

$0\nu\beta\beta$ decay can be observed with a 50 % chance at a $3\,\sigma$ significance. The drawn lines represent the sensitivity dependence on four different background levels in the ROI. A strong dependence of the discovery potential on the background level is apparent. In the ideal case of no background the sensitivity scales linearly with the exposure while in the case of an existing background it increases with the square root of the exposure. The mass range of $m_{\beta\beta}$ in the case of the inverted neutrino hierarchy ($\approx (15\text{ - }50)$ meV) is indicated as a grey shaded area (different assumptions like a light Majorana neutrino exchange were assumed). It can be seen that for a background free search an exposure of a few ton years is enough to exclude the whole inverted hierarchy region. However, for a background level above 0.1 counts/(FWHM t yr) an exposure of > 10 ton years is necessary[1].

In general, the dominant backgrounds for rare event searches can be categorised into two groups: the backgrounds from natural radioactivity and the backgrounds induced by cosmogenic particles. Experiments that search for rare processes have to undertake several measures to reach the necessary low background levels. This is typically achieved by first identifying the dominant background sources of an experiment. Secondly, these sources have to be understood and finally as far as possible reduced. The identification of the individual contributions is not simple as each low-background experiment is unique, owing to the usage of different materials, different concepts (e.g. different detector types) and different data analysis techniques (e.g. pulse shape discrimination). This means that at the start of an experiment not all background contributions can be precisely predicted. The understanding of the different background contributions often requires work-intensive studies in the laboratories as well as extensive MC simulation studies.

2.1 Cosmic Rays and Cosmogenic Particles

In the following, the origin and the composition of cosmic rays and cosmogenic particles is introduced. Then, the backgrounds induced by cosmogenic particles in low-background experiments are discussed, with a special focus on muon-induced neutrons.

[1] FWHM stands for full width at half maximum.

2.1.1 Origin and Composition of Cosmic Rays and Cosmogenic Particles

Cosmic rays are high-energy particles that hit the atmosphere of the Earth from all directions of the sky. The energies of these particles range from a few MeV to $> 10^8$ TeV [53]. The maximal energies of cosmic rays are many orders of magnitude higher than current men made accelerators on Earth can reach [54]. Cosmic rays are mainly charged particles, composed of $\approx 87\,\%$ protons, $\approx 12\,\%$ alpha particles and $\approx 1\,\%$ heavier atomic nuclei and electrons [53]. Also neutral cosmic rays like photons hit the atmosphere of the Earth. In Fig. 2.2 the kinetic energy spectrum of various nuclei, contributing to the total cosmic ray flux, are depicted. The flux of all nuclei decreases with an increasing kinetic energy.

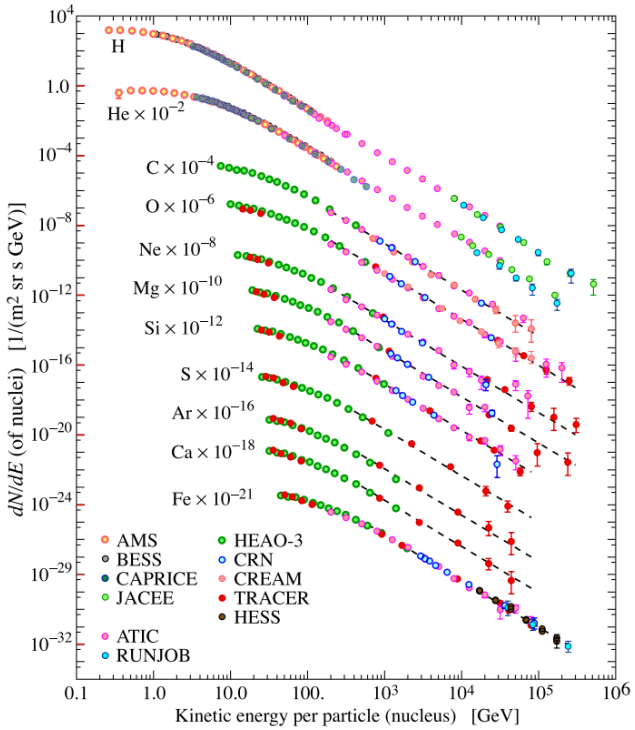

Figure 2.2: Flux of cosmic rays, resulting from different nuclei, as a function of their kinetic energy. The colours indicate the different experiments that contributed to the study of cosmic rays. Taken from [55].

Cosmic rays with energies $> 1\,\text{GeV}$ originate from the outside the solar system. They are mainly produced within our galaxy by the Fermi acceleration of charged particles [56]. Possible production sites are supernova remnant shocks [57] and active galactic nuclei [58]. Cosmic rays are nearly isotropically

distributed over the sky, owing to their diffusive propagation within the galactic magnetic field [59].

When cosmic rays penetrate Earth's atmosphere and interact with the nuclei therein, air showers can be produced. In these air showers plenty of cosmogenic particles are generated. The number and type of particles generated depend on quantities such as the energy, the rest mass and the charge of the incident cosmic rays. Obviously, also the composition of Earth's atmosphere and its density play an important role in the production of cosmogenic particles. Cosmic rays themselves do not travel far in the atmosphere until they interact and induce further particles. In Fig. 2.3 an air shower, initiated by a cosmic ray proton, is schematically depicted. Many of the cosmogenic particles produced in such an

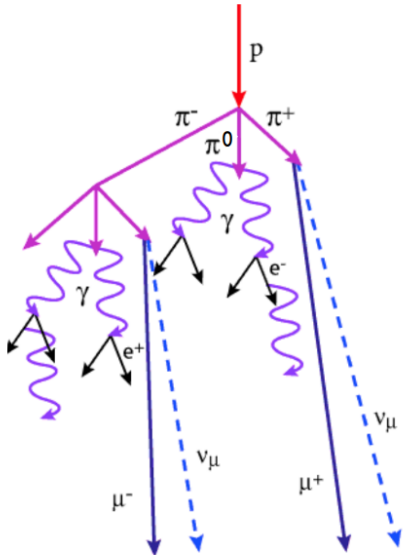

Figure 2.3: Schematic view of an air shower, initiated by a cosmic ray proton in the atmosphere of the Earth. Various cosmogenic particles are produced by the decay of pions, including photons, muons and neutrinos. Taken from [60].

air shower easily reach Earth's surface and even penetrate it.

Due to the importance of muons for low-background experiments (see later), a brief introduction to the production and the propagation of muons in Earth's atmosphere is given. Muons and anti-muons are typically produced at an altitude of $\approx 15\,\mathrm{km}$ in Earth's atmosphere [55]. The majority of muons results from charged pion decays while a minor part originates from charged kaon decays[2].

[2]Also heavier flavours contribute to the muon production but can be neglected except for very high muon energies [61].

Muons lose on average $\approx 2\,\mathrm{GeV}$ on their way towards Earth's surface and reach it with a mean energy of $\approx 4\,\mathrm{GeV}$. The muon charge ratio, defined as the quotient between the number of anti-muons and muons, depends on the muon energy and ranges from ≈ 1.15 for 1 GeV muons up to ≈ 1.45 for 8 TeV muons. The ratio > 1 results from the charge of cosmic rays. The majority of cosmic rays hitting Earth's atmosphere is positively charged, leading to an enhanced production of positively charged pions and kaons and therefore positively charged muons in the air showers.

On the surface of the Earth there is a high flux of cosmogenic particles of all kinds. Already the flux of muons (integral intensity of vertical muons above 1 GeV: $\approx 70\,\mathrm{m^{-2}\,s^{-1}\,sr^{-1}}$ [55]) would make it impossible to perform a low-background experiment on the surface. In order to reduce the number of cosmogenic particles and thus its correlated background, these experiments are located typically in deep underground laboratories. Except for muons and neutrinos, all other cosmogenic particles can not penetrate deep into the Earth, as they lose their energy already in the first few meters of soil. Also the muon flux decreases with an increasing overburden depth of an underground laboratory. The experimentally determined relation between the vertical muon intensity and the depth of an overburden, expressed in mwe, is depicted in Fig. 2.4. The experiments that contributed to this relation studied muons coming from different angles. A single experiment can therefore yield information for various shielding depths. The shaded region in the plot represents the flux of muons above 2 GeV that propagate upwards. These muons are produced by muon neutrinos via charged current interactions. These muons, compared to the ones produced in the atmosphere, can not be reduced by moving to deeper underground laboratories.

2.1.2 Interactions of Muons with Matter and Subsequent Production of Muon-Induced Neutrons

During the passage through matter muons interact and lose energy. There are four main processes by which muons deposit energy in matter: ionisation (i.e. muon-electron scattering), bremsstrahlung, electron-positron pair production and muon-nuclear inelastic scattering. The contribution of the different processes to the total energy loss is depicted in Fig. 2.5 as an example for muons in iron with energies between 10 GeV and 10 TeV. It is apparent that for muon energies up to a few hundred GeV the total energy loss is dominated by ionisation, while

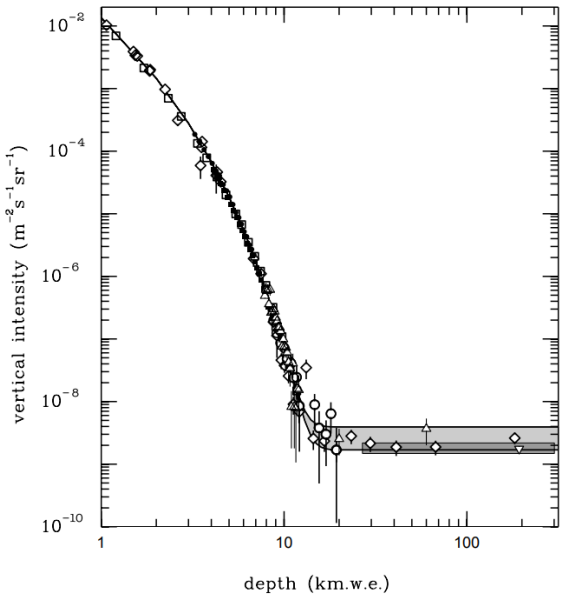

Figure 2.4: Measured vertical muon intensity as a function of the overburden depth. The shaded area for depths > 10 kilometres of water equivalent results from neutrino-induced muons (only muons with energies $> 2\,\mathrm{GeV}$ are taken into account). Various experiments like MACRO [62] and LVD [63] participated in the measurement of muons deep underground. Adapted from [64].

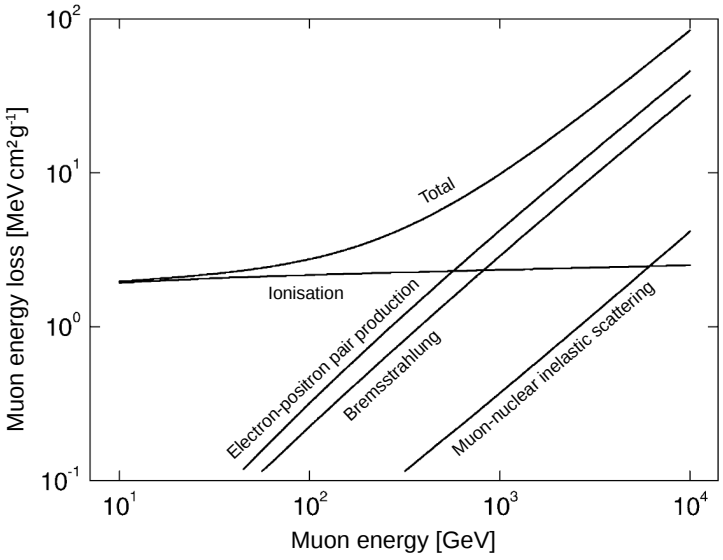

Figure 2.5: Dominating muon interaction processes to the total energy loss of muons in iron. Up to a muon energy of few hundred GeV the energy loss is dominated by ionisation. Adapted from [65].

for higher energies electron-positron pair production and bremsstrahlung become dominant.

The passage of muons through matter can lead to the production of various particles, like electrons, positrons, protons, neutrons and gammas. Of them, neutrons are one of the more critical particles for low-background experiments (see Section 2.1.3). Muon-induced neutrons can either get produced directly by a muon or indirectly in a muon-initiated shower. Direct production processes are muon-nuclear inelastic scattering reactions (in literature also-called muon spallation) and muon capture. In general, neutrons from muon capture dominate the neutron production in underground laboratories up to depths of $\approx 80\,\mathrm{mwe}$ [66]. Muon-initiated showers that lead to neutrons are similar to the ones induced by cosmic rays in the Earth's atmosphere. Muon-induced showers can be separated into hadronic and electromagnetic showers. Hadronic showers are composed of different hadrons, mainly pions, neutrons and protons whereas electromagnetic showers are composed of electrons, positrons and photons. Depending on the energy and the type of particles in a shower, further particles (including neutrons) are produced. In general, if the energy of a muon is high and the shower is fully developed (i.e. the number and composition of particles produced in the shower per track length is constant), the neutrons from the shower outnumber the directly produced neutrons [67]. According to [67] the minimal path length of muons in matter, defined here as the product of the track length and the density of the matter, to reach a fully developed shower is $800\,\mathrm{g\,cm^{-2}}$. With the development of the shower, also the number of neutrons per track length increases. Furthermore, the number of neutrons produced increases with the muon energy (see also Section 3.2.2) [68]. In the following, the dominating production processes for muon-induced neutrons are discussed.

Muon-Nuclear Inelastic Scattering Reactions

The process of muon-nuclear inelastic scattering reaction, muon-nuclear reaction in the following, refers to the inelastic scattering of a muon on a nucleus, via the exchange of a virtual photon. This process typically leads to the disintegration of the nucleus. A number of different particles like pions, gammas, protons and neutrons as well as various residual nuclei can get produced. Muon-nuclear reactions proceed on two time scales. In the first $(10^{-22}\text{-}10^{-21})\,\mathrm{s}$ of the interaction nucleons get knocked out from the nucleus [66]. At time scales of $10^{-16}\,\mathrm{s}$ the excited residual nucleus may evaporate neutrons. The respective neutrons from these two processes are called knock out neutrons and evaporation neutrons in

the following. The momenta of the knock out neutrons are focused along the momentum direction of the muon, while the evaporation neutrons are emitted nearly isotropically. In Fig. 2.6 a schematic illustration of the muon-nuclear process is shown. The muon coherently interacts with the nucleus in the case of an

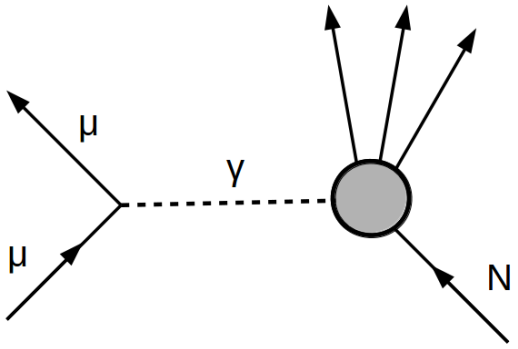

Figure 2.6: Schematic illustration of the muon-nuclear process. The muon interacts inelastically with the nucleus via the exchange of a virtual photon, leading to the fragmentation of the nucleus. Various particles like neutrons, protons and gammas can get produced in this process.

energy transfer $< 300\,\mathrm{MeV}$ [66]. For higher energy transfers the muon interacts with a single nucleon of the nucleus.

Muon-nuclear reactions are the largest source of uncertainty for the production of muon-induced neutrons, especially at low muon energies [69]. Models suggest to assess the cross section of the virtual photons in muon-nuclear reactions by relating it to the measured cross section of real photons with nuclei (called equivalent photon approximation) [69, 70].

Capture of Negatively Charged Muons on Nuclei

The second muon interaction process that leads to the direct production of neutrons is the capture of a negatively charged muon on a nucleus. The muon capture process proceeds in the following way: Slow negatively charged muons can get bound in the Coulomb field of a nucleus (similar to electrons). The muon cascades down to the 1s state within a time scale on the order of $10^{-13}\,\mathrm{s}$ [71]. During this process, Auger electrons as well as X-rays are emitted. In the 1s state the muon has two different reaction channels. The first is the decay of the muon, described by

$$\mu^- \longrightarrow e^- + \bar{\nu}_e + \nu_\mu, \tag{2.1}$$

where no neutrons are produced. The second channel is the capture of the muon by the nucleus (X) via the weak charged current process

$$\mu^- + \mathrm{X(A,Z)} \longrightarrow \nu_\mu + \mathrm{X(A,Z\text{-}1)}. \tag{2.2}$$

In this reaction the residual nucleus is highly excited and subsequently evaporates neutrons, gammas and other particles. The average multiplicity of the evaporated neutrons in this reaction depends on the capturing nucleus [70].

Photo-Nuclear Inelastic Scattering Reactions

The production of neutrons in photo-nuclear inelastic scattering reactions, called photo-nuclear reactions in the following, is induced by high-energy gamma rays. A gamma gets absorbed by a nucleus, resulting in an exited state. Depending on the excited state the nucleus can emit a number of different particles, including neutrons. The minimal energy of a gamma to lead to the production of neutrons via photo-nuclear reactions depends on the nucleus and is in the range of (5 - 10) MeV. This energy is similar to the average nucleon binding energy, for nuclei with mass numbers ≥ 4. The gammas that lead to photo-nuclear reactions originate for example from muon bremsstrahlung or are created within electromagnetic showers that are induced by muons. The dominating source of gammas depends on the material, the muon energy and how far the electromagnetic shower is developed [72].

Hadron-Nuclear Inelastic Scattering Reactions

The process of hadron-nuclear inelastic scattering reaction refers to the inelastic scattering of a hadron off a nucleus. In this process, called hadron-nuclear reaction in the following, nucleons can get knocked out from the nucleus (similar to a muon-nuclear reaction) [73]. This can be followed by the evaporation of further particles by the excited residual nucleus. The incident hadron of such a reaction originates for example from a previous muon-nuclear reaction or any other hadron producing process. Hadron-nuclear reactions typically occur within hadronic cascades. However, a single neutron can lead to the production of further neutrons via neutron inelastic scattering off a nucleus as well.

2.1.3 Backgrounds from Cosmogenic Particles

As discussed in Section 2.1.1, low-background experiments are typically located in deep underground laboratories to reduce cosmogenic backgrounds. Examples are GERDA and CRESST which are operated at the Laboratori Nazionali del Gran Sasso which provides a shielding depth of ≈ 3800 mwe [74, 75]. As discussed before, not all cosmogenic particles can be fully shielded by going deep into the underground. Muons can still reach these experiments and lead to backgrounds. Signals can be generated by the muon itself or by any muon-induced particle, produced inside or outside of the experimental setup.

A way to reduce these backgrounds is to operate active shielding. Often used are plastic muon veto systems, located on top and on the side of the experiments. In addition, systems in which the target detectors are directly deployed in liquid scintillators (e.g. argon) or surrounded by water tanks are often utilised [52, 76, 77]. In the case of an observed signal in any veto system, indicating a muon or any muon-induced particle, all events in the target detectors that are in time coincidence with this signal can be rejected.

Backgrounds resulting from energy depositions of neutrons in the target detectors are especially critical. This results from the fact that the induced signals are often hard to discriminate from the searched for signals (e.g. from WIMPs). Further, as neutrons are neutral particles and hence have particularly long mean free paths, their energy depositions are in general difficult to veto. In low-Z materials, compared to high-Z ones, less neutrons get induced by muons. Hence, muon-induced neutron backgrounds can be reduced by choosing low-Z materials for the components of the setup that are located in the vicinity of the target detectors. Muon-induced neutrons can have energies up to several GeV [70]. The majority of the neutrons (depending on the location of their production) can be absorbed by layers of neutron moderators like water or polyethylene, surrounding the target detectors. Potentially, these layers can be combined with materials that have a high neutron capture cross section (e.g. materials containing cadmium or gadolinium). Nevertheless, it is very difficult to shield high-energy neutrons completely. This makes muon-induced neutrons a challenging background. For future ton-scale experiments like EURECA [78] or LEGEND [29], muon-induced neutrons could yield a sizeable contribution to the background in the ROI. This holds even though such experiments are typically planned to have a setup design, explicitly addressing the neutron background mitigation.

A further background of muon-induced neutrons results from their capture on nuclei. Such captures can lead to the production of long-lived metastable

isotopes. If the time correlation to the original muon is lost, due to the long half-life of the produced isotopes, then theirs decays can lead to signals in the target detectors. An example for such a long-lived isotope for $0\nu\beta\beta$ decay experiments, using germanium detectors enriched in ^{76}Ge, is ^{77}Ge. It has a half-life of $\approx 11\,\mathrm{h}$ and a Q-value of 2702 keV which is above the Q-value of the $0\nu\beta\beta$ decay of ^{76}Ge (2039 keV) [79].

The exposure of materials, used in low-background experiments (especially the target detectors itself and the materials used in their vicinity), to cosmogenic particles on Earth's surface should be as short as possible. This measure reduces the cosmogenic activation of various materials with long-lived isotopes. An example for such an isotope is ^{60}Co, which is produced by cosmogenic particles from copper or germanium. This isotope has a Q-value of 2834 keV and a half-life of 5.3 yr [80].

2.2 Natural Radioactivity

In addition to the backgrounds induced by cosmogenic particles, also natural radioactivity contributes to the background of rare event searches. All used materials in an experimental setup as well as the surroundings (e.g. rock or concrete) contain radioactive isotopes. The present radioactivity is mainly primordial, meaning it was produced before Earth was formed. The dominating part of the backgrounds from natural radioactivity (in the context of low-background experiments) results from the isotopes of the long-lived ^{238}U, ^{235}U and ^{232}Th decay chains as well as from ^{40}K [70]. The decay chain for the mother isotope ^{238}U is schematically depicted in Fig. 2.7. It is apparent that within the chain many alpha and beta decays occur, leading to the release of various particles that can contribute to the backgrounds of rare event searches. Prominent examples of gamma rays from natural radioactivity have energies of 2.6 MeV and 2.2 MeV and result from the decays of ^{208}Tl and ^{214}Bi, respectively. These gamma lines are especially a critical background for experiments searching for $0\nu\beta\beta$ decay of ^{76}Ge ($Q_{\beta\beta}$ of 2039 keV) [82]. The gamma line of ^{40}K with an energy of 1460 keV does not affect the ROI of experiments searching for $0\nu\beta\beta$ with germanium detectors, but yields backgrounds for experiments looking for energy depositions $< 1460\,\mathrm{keV}$ [83, 84].

Neutrons from radioactivity result from spontaneous fission as well as alpha-neutron (α,n) reactions. Spontaneous fission refers to the spontaneous breakup of heavy nuclei into lighter nuclei, typically accompanied by the emission of a

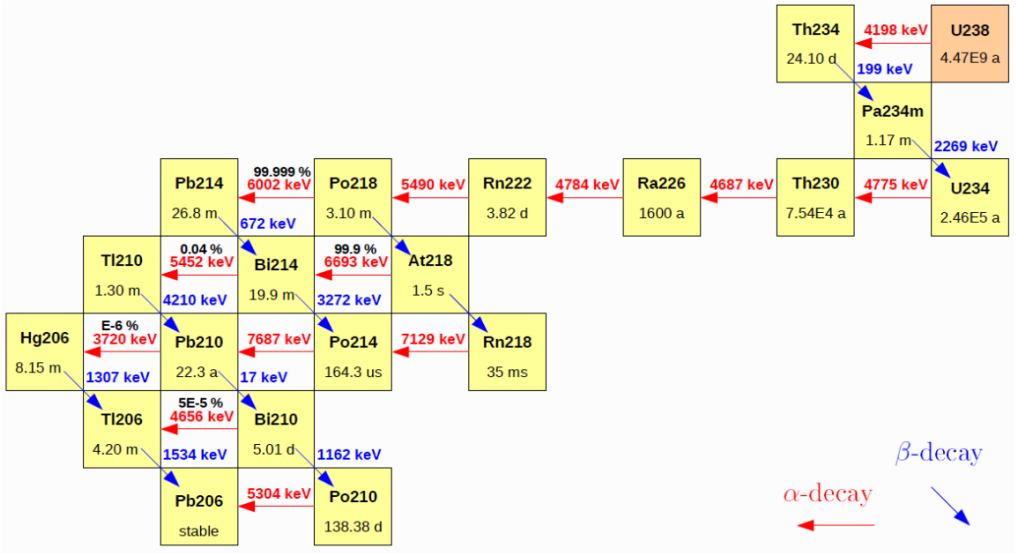

Figure 2.7: Schematic of uranium-radium decay series. The lifetime of the chain is dominated by the half-life of ^{238}U with $\approx 4.5 \cdot 10^9$ yr. Alpha decays are indicated by red arrows while blue arrows represent beta decays. Always the most probable decay channel is stated. Taken from [81].

few neutrons. Typical elements that undergo spontaneous fission are uranium and thorium [70]. For example, in the case of ^{238}U on average ≈ 2 neutrons are released in this process. In (α,n) reactions an alpha, originating from the primordial uranium or thorium decay chains, interacts with the nucleus of a light element (like ^{9}Be) and leads to the production of neutrons. The energy of neutrons from spontaneous fission and (α,n) reactions ranges up to a maximum of ≈ 10 MeV [70]. The neutrons from radioactivity can lead to similar backgrounds as discussed for the muon-induced neutrons (see Section 2.1.3).

To reduce backgrounds from natural radioactivity different measures can be undertaken. Compared to backgrounds from cosmogenic particles, going underground does not help. However, an extremely important measure to reduce backgrounds from natural radioactivity is the purification and careful selection of materials. This is especially crucial for the target detector material as well as for any experimental part in the close vicinity of the target detectors. Furthermore, the mass of all components introducing backgrounds (e.g. cables) should be reduced as much as possible [85]. In order to shield the particles (induced by radioactive decays outside the detector volume) from the target detectors, different layers of shielding materials are often installed. Typically used for the reduction of gamma rays and beta particles are high-Z materials like copper and

lead [86]. Also the deployment of active shielding (see Section 2.1.3), operated as a veto system, can be used to identify backgrounds from natural radioactivity. Compared to muon-induced neutrons (energies up to several GeV), neutrons from natural radioactivity (energies up to 10 MeV) can be more efficiently shielded by layers of low-Z materials. This holds, even though neutrons from radioactivity significantly outnumber muon-induced neutrons underground (for underground depths greater than a few tens of meters) [70].

Chapter 3

Measurements and Simulations of Muon-Induced Neutrons

In order to fully understand and correctly predict backgrounds, resulting from muon-induced neutrons, reliable simulation tools are crucial. However, current Monte Carlo tools do not reliably and consistently enough reproduce experimental findings of muon-induced neutrons. In the following, the simulation toolkit Geant4, used in the scope of this work, is shortly introduced. Afterwards, the neutron yield and its different definitions are discussed. At the end, the predictions of Monte Carlo tools for a few experiments are compared to the corresponding experimental findings.

3.1 Monte Carlo Simulation Toolkit Geant4

MaGe [87], a simulation toolkit based on Geant4 [88] and widely used within the low-background community, was used for the simulations in the context of this thesis. MaGe is jointly developed between the GERDA and the MAJORANA collaborations and is optimised for the framework of low-background experiments. Geant4, an established Monte Carlo toolkit in particle physics, provides the physics foundations for MaGe. Consequently, all MaGe predictions within this thesis are labelled as Geant4.

Geant4 simulates the propagation and interaction of particles in matter. As a user, a so-called physics list has to be selected. Such a list contains a collection of Geant4 models that describe the different physics processes. For each particle type, particle energy, interaction type and material the particle is propagating through, different models are assigned, depending on the chosen physics list. The selected physics list therefore has a direct influence on Geant4

predictions. Typically before simulating, the physics list that fits the application best is selected.

There is a constant development and improvement process of Geant4, leading to a continuous release of new versions. The MaGe version that was used in the scope of this work was released on 17th of February 2017. The underlying Geant4 version is 10.3, released on 9th December 2016. If not stated explicitly, all simulation within this thesis were carried out with the MaGe Default physics list [87], the list recommended by the MaGe developers for low-background physics applications. The MaGe Default physics list uses the QGSP_BERT_HP reference physics list for hadronic interactions (for more details on this list see [89]). This reference physics list includes a data driven high precision physics model for the propagation of neutrons from 20 MeV down to thermal energies. Another physics list, suited for the context of muon-induced neutrons, is the Shielding physics list. This list is recommended by the Geant4 collaboration for underground and low-background experiments as well as neutron penetration studies [90]. The hadronic interactions of this list are based on the FTFP_BERT_HP reference physics list, which also includes the data driven high precision model for the propagation of low-energy neutrons (for a more detailed description of this list see [89]). Differences of Geant4 predictions, obtained with different suited physics lists, are typically taken into account as a systematic uncertainty. Note that muon-nuclear and photo-nuclear reactions in Geant4 are described the same way, when Geant4 recommended or standard physics lists are selected [91, 92, 93]. The description of muon-nuclear and photo-nuclear reactions in MaGe is identical to their description in Geant4, when the Default or the Shielding physics list is chosen for MaGe [87].

In the context of the MINIDEX project [94], in addition to Geant4 also the Monte Carlo simulation package FLUKA [95, 96] (version: 2011.2c) was utilised. FLUKA is an established MC tool that is used in various fields, including high-energy particle physics and medical physics. In comparison to Geant4, in FLUKA no physics list can be selected by the user. As a consequence, differences in FLUKA simulations can not result from different assumptions on the underlying interaction processes. This makes comparisons between two FLUKA simulations much easier than between two Geant4 simulations.

3.2 Neutron Yield in Theory and Experiment

Muon-induced neutrons have been studied for many decades. Most of the investigated data sets result from experiments that are located underground. Only a few of these underground experiments like [72] or [97] were dedicated to the study of muon-induced neutrons. Most measurements of muon-induced neutrons result from underground experiments that have a different main purpose. Examples are the searches for dark matter with ZEPLIN-III [98] or for neutrino oscillations with KamLAND [99]. In addition to the underground experiments, also experiments that use muon beams contributed to the study of muon-induced neutrons [100, 101].

3.2.1 Definitions and Scaling of Neutron Yield

The typically stated quantity, resulting from an experimental study of muon-induced neutrons, is the neutron yield Y. This quantity relies on comparisons to simulations, as the neutron yield itself can in general not be directly measured. An imprecise description of the muon-induced neutrons by the simulation (i.e. of their production or their propagation) therefore leads to an imprecise neutron yield. Furthermore, different definitions of the neutron yield exist, making a comparison between them even more difficult. In the following, the different neutron yield definitions and their deficiencies are discussed.

The general definition of the neutron yield is

$$\mathrm{Y} = \frac{\mathrm{N_n}}{\mathrm{N}_\mu \cdot X_\mu \cdot \rho_{\mathrm{target}}}, \tag{3.1}$$

where N_μ is the number of muons that pass through the investigated target, X_μ the average track length of the muons in the target and ρ_{target} the density of the target material. The variable $\mathrm{N_n}$ stands for the number of neutrons considered, depending on the chosen definition of the neutron yield.

Three different definitions of the neutron yield are typically used in literature. The first one is the external neutron yield, $\mathrm{Y_{Ext}}$, for which $\mathrm{N_n}$ represents the number of neutrons emerging from a selected surface of the target [72, 102]. The second one is the neutron production yield, $\mathrm{Y_{Pro}}$, for which $\mathrm{N_n}$ states the total number of neutrons produced within the target [72, 103]. Both neutron yields depend significantly on the target geometry. For example, an increased target thickness (along the momentum direction of the muons) leads to a higher neutron production, as the muon-induced shower in the target will be more developed [67]. An increased width of the target leads to a higher neutron production as well,

due to the same reason. Furthermore, Y_{Ext} and Y_{Pro} depend on the muon-induced showers from the rock overburden and the support structures of the experimental setup. These showers, if not fully understood and rejected in the analysis, modify the resulting neutron yield. The third definition of the neutron yield is the equilibrium production yield Y_{Equi} [72, 98]. In this case, N_n states the total number of neutrons produced in an idealised target, meaning that the target is thick and wide enough to allow fully developed showers. Note, only those parts of the idealised target, for which the showers are fully developed, are considered in its determination. This makes Y_{Equi} a geometry independent quantity, reporting the maximum neutron production for the given material. Note that only muons are used as an input to the idealised simulation. Consequently, there is no contribution of particles produced outside of the target.

In general, only a small part of the produced or emitted neutrons are actually measured. Consequently, the determination of the neutron yields heavily depends on simulations. In order to get a realistic neutron yield, discrepancies between the measured and the predicted observable have to be taken into account. For example, if the rate of measured neutrons is underpredicted by the simulation, then an underpredicted neutron production by the simulation is expected. The procedure typically applied and described by

$$Y = Y^{Sim} \cdot MF_S \tag{3.2}$$

scales the neutron yield (any of them) predicted by simulation, Y^{Sim}, with the determined mismatch factor, MF_S, between the measured and the predicted observable [72, 98, 104]. Note that this procedure scales the number of all neutrons, independent of the correct description of the individual neutron production processes in the simulation. Together with an energy dependent neutron detection efficiency, this can lead to the introduction of uncertainties, which are very difficult to assess[1]. This might be especially the case when a high discrepancy is found between the measured and the predicted observable.

3.2.2 Relation Between Neutron Yield and Muon Energy

All three discussed neutron yields increase with an increasing muon energy [105]. The deeper underground an experiment is located, the higher the mean muon

[1] Also other quantities, if not precisely described by the simulation, can lead to the introduction of further non-assessable uncertainties. Examples are the momentum direction and the generation location of the neutrons.

energy $\overline{E}_\mu$ and consequently the neutron yield Y is. The relation between $\overline{E}_\mu$ and Y can be parametrised for each material by a power law function [106]:

$$Y(\overline{E}_\mu) = b \cdot \overline{E}_\mu{}^{\alpha}. \tag{3.3}$$

Despite the various definitions and the discussed deficiencies of the neutron yield, the parameters of the power law function (b and α) can be determined using experimental results. It should be noted that especially for old experiments (i.e. older than (10 - 20) yr) the stated neutron yields have to be treated with additional care [107]. During these times the predictions of MC tools were poor, resulting in a limited understanding of the influence of the used experimental components.

In Fig. 3.1 a set of published neutron yields Y_{Ext} and Y_{Equi} for lead, determined at various underground depths ($\overline{E}_\mu$ between a few GeV and several hundreds of GeV), is shown. Results from experiments that were performed over the

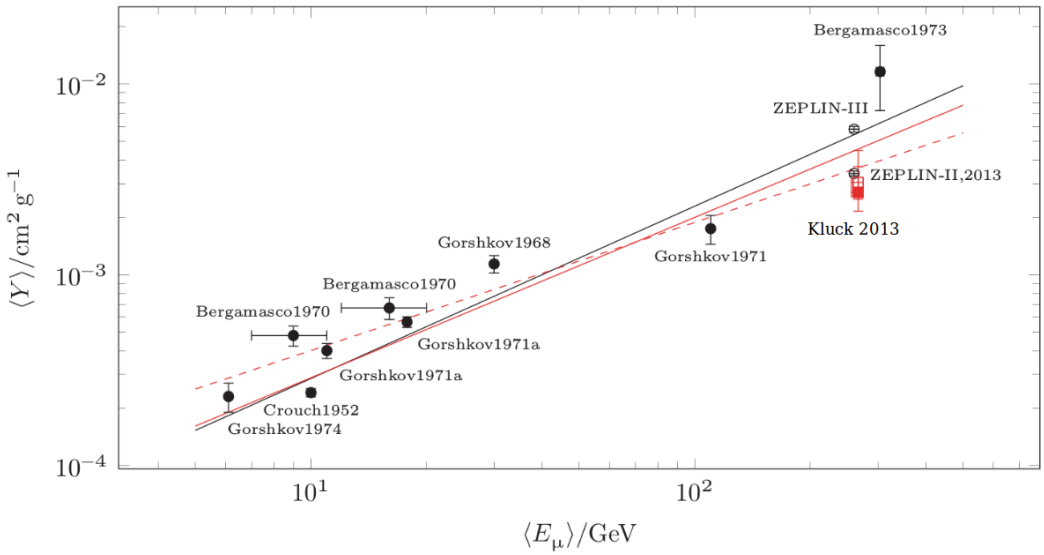

Figure 3.1: Dependence of the neutron yield for lead on the mean muon energy in the corresponding underground laboratory. The filled markers represent results published as Y_{Ext} whereas the open markers stand for results published as Y_{Equi}. Different subsets of the depicted data set were fit in [72] to determine the parameters of Eq. (3.3) for lead, indicated by the different lines. While the red solid line represents a fit to all Y_{Ext}, the solid black and dashed red lines stand for fits that exclude the results of Kluck2013 and Crouch1952, respectively. Adapted from [72].

last decades are included. For example, the results denoted as Bergamasco1970 are already $\approx$50 years old [108]. However, also more recent measurements of

muon-induced neutrons, like the 2013 published results of the lead shielding of the ZEPLIN-III dark matter detector [98], are included. An applied power law fit, depicted as a solid red line, was performed in [72] to determine the parameters of Eq. (3.3) for lead. Note, only external neutron yields Y_{Ext} were included in this fit. For b and α, values of $(4.2 \pm 1.5) \cdot 10^{-5}\,\mathrm{cm}^2\,\mathrm{g}^{-1}$ and 0.84 ± 0.13 were obtained, respectively.

In [109] the parameters of Eq. (3.3) were determined for liquid scintillator. Different neutron yields for mean muon energies between a few tens and a few hundreds of GeV were considered. For example, the neutron yields from experiments like the Cosmic-ray Underground Background Experiment ($\overline{E}_\mu$ of $\approx 13\,\mathrm{GeV}$, 1995, [110]) or Borexino ($\overline{E}_\mu$ of $\approx 280\,\mathrm{GeV}$, 2013, [111]) were taken into account. The determined values of b and α (i.e. the parameters of Eq. (3.3)) for liquid scintillator are $(4.0 \pm 0.6) \cdot 10^{-6}\,\mathrm{cm}^2\,\mathrm{g}^{-1}$ and 0.77 ± 0.03, respectively [109].

3.3 Reliability of Monte Carlo Tools

Various experiments have measured muon-induced neutrons in different materials and at different muon energies. The simulations of muon-induced neutrons were often compared to the experimental findings, partially yielding discrepancies and partially agreements. In general, the neutron transport is assumed to be reasonably well described by simulations [112]. For MC predictions in the context of muon-induced neutrons often a factor 2 is recommended to be taken as a systematic uncertainty [67, 113]. As MC tools constantly get developed and therefore improved (in general), a definite answer on their predictive power is difficult. Found discrepancies between experimental observations and the corresponding MC predictions could have been already solved within the release of a new version. Note that every new version of Geant4 typically yields different simulation results for muon-induced neutrons [72, 98]. Also the selection of a different physics list in Geant4 might lead to significantly different simulation predictions.

In order to improve the predictive power of MC tools, experimental data sets of muon-induced neutrons are crucial. These data sets are used to evaluate and afterwards improve the simulation tools. In the following, the predictions of Geant4 and FLUKA for a few more recent measurements of muon-induced neutrons, with a focus on lead and other high-Z materials, are compared to the corresponding experimental findings. Additionally, studies that investigated the neutron production in photo-nuclear reactions are discussed. Although no

muons are involved in these studies, they provide an important feedback on the predictive power of simulation tools with regards to the muon-induced neutron production in photo-nuclear reactions.

The veto system of the ZEPLIN-III dark matter detector was used to measure muon-induced neutrons produced in lead [98]. The mean energy of the muons at the position of the experiment in the Boulby Underground Laboratory is $\approx 260\,\mathrm{GeV}$. The analysis of the experimental and the Geant4 generated MC data set yielded an $\approx 25\,\%$ higher number of neutron signals per tagged muon in the measurement. Furthermore, discrepancies between measured and simulated neutron multiplicities have been observed. An investigation of the influence of the used Geant4 version and the selected physics list yielded up to a factor of ≈ 2 different neutron yields. Also a trend of the neutron yield towards higher values with every released Geant4 version was found. Note, as the geometry of the ZEPLIN-III detector is complicated, the measurement of muon-induced neutrons and the understanding of their detection efficiencies is difficult. As a consequence, the results should be treated carefully.

In Borexino the neutron production yield was (to some extent) directly measured at a mean muon energy of 280 GeV [111]. This was feasible as the experiment contains a large amount of liquid scintillator (278 t) within a spherical construction. The geometry of Borexino is much simpler than the geometries of earlier liquid scintillator experiments like LVD [114]. This led to a better understanding of the neutron production within the liquid scintillator of Borexino and therefore to a more reliable determination of the neutron production yield. Geant4 and FLUKA predictions were compared to the experimental observations. It was found that FLUKA consistently describes the experimental observables [107, 115]. This includes the neutron production yield, the lateral distance of the muon-induced neutrons from the muon track, as well as the multiplicity of neutron captures. For Geant4 the situation is different. Various hadronic models were composed and their predictive power tested on the experimental data [111]. A single simulation, using only one of these hadronic models, could not reproduce all experimental observables. However, each individual observable can be described reasonably well by a simulation that uses one of the composed hadronic models. Consequently, a final conclusion on the reliability of Geant4 in the context of muon-induced neutrons in liquid scintillator at high muon energies is difficult.

In the Laboratoire Souterrain de Modane in the context of the EDELWEISS experiment a neutron counter, based on gadolinium doped liquid scintillator,

measured muon-induced neutrons produced in lead at a mean muon energy of $\approx 267\,\mathrm{GeV}$ [72]. The Geant4 predicted number of detected neutron signals per tagged muon was found to be $\approx 20\,\%$ higher than the measured value. On the other hand, a good overall agreement between the measured and Geant4 predicted neutron signal multiplicity was determined. This work again showed a dependence of the neutron yield on the used Geant4 version as well as on the selected physics list.

A study [116] was carried out to compare the photo-nuclear cross sections for the neutron production in different materials (^{9}Be, ^{48}Ti, ^{133}Cs, ^{197}Au), implemented in Geant4, with the cross sections from the Exchange Format experimental nuclear reaction database [117]. Large discrepancies between the cross sections provided by the experimental data base and the implemented cross sections in Geant4 were found, yielding strong evidence for an imprecise description of the neutron production in photo-nuclear reactions in Geant4.

In the n@BTF experiment, which used the Beam Test Facility at the National Laboratory of Frascati, pulsed electrons with an energy of 510 MeV were shot on a fixed high-Z target [118]. In the target, which consisted of tungsten, electron-induced neutrons were produced. The majority of these neutrons originate from photo-nuclear reactions. The flux of neutrons that leave the target was measured with a Bonner Sphere Spectrometer. It was found that the measured flux of emitted neutrons is in good agreement with the FLUKA predicted flux. Furthermore, FLUKA reproduced the measured energy spectrum of the emitted neutrons well. In contrast to this, Geant4 did neither reproduce the measured energy spectrum of the emitted neutrons nor their flux (underpredicted by $\approx 40\,\%$) correctly. Different Geant4 recommended and standard physics lists were used and the obtained results were found to be in good agreement. Further, the neutron production cross sections for photo-nuclear reactions (in natural tungsten, lead and zinc), implemented in Geant4 and FLUKA, were compared to the experimental and evaluated cross sections recommended by the International Atomic Energy Agency (IAEA) [119]. While the cross sections implemented in FLUKA agree well with the IAEA recommended ones, large deviations were found for Geant4. In conclusion, the results of [118] convincingly point towards an imprecise description of the neutron production in photo-nuclear reactions in Geant4. In contrast to this, the FLUKA predicted neutron production in photo-nuclear reactions seems to be much more reliable.

For some time of MINIDEX Run 2 an additional neutron detector was installed next to the MINIDEX setup [120]. This additional detector used gadolinium doped liquid scintillator to measure muon-induced neutrons from lead (at a

mean muon energy of $\approx 9\,\mathrm{GeV}$). Geant4 results for different quantities were compared to the experimental observations. It was found that Geant4 underpredicts the number of detected neutron signals for tagged muons by a factor of ≈ 1.5 to ≈ 3 (depending on the used Geant4 version and the applied cuts). Furthermore, it was found that the multiplicity of detected neutron signals is underestimated by the simulation. The energy spectrum of neutrons induced by muons in lead was unfolded in a range from $5\,\mathrm{MeV}$ to $40\,\mathrm{MeV}$. The results suggest that the unfolded spectrum is harder than the corresponding Geant4 predicted spectrum. It should be noted that more recent investigations of the neutron detector MC data analysis revealed some systematic inaccuracy in the muon tag determination procedure. As a consequence, the simulation predictions of this study should be treated with special care.

From the reviewed studies it can be concluded that a factor of 2 as a systematic uncertainty on Geant4 predictions in the context of muon-induced neutrons seems to be reasonable. On the other hand, FLUKA simulations seem to have a lower systematic uncertainty.

Chapter 4

Experimental Setup, Working Principle and Detectors

MINIDEX is a compact, flexible and simple experimental setup which was designed to measure muon-induced neutrons in different high-Z materials, potentially at different underground locations [121]. MINIDEX is presently located in the Tübingen Shallow Underground Laboratory (see Section 6.1.1). A shallow underground site was chosen to shield the cosmogenic atmospheric neutron flux while at the same time preserve a high muon flux ($\approx 65\,\text{muons}\,\text{m}^{-2}\,\text{s}^{-1}$, see Section 6.1.1).

The first measurement of muon-induced neutrons was accomplished in 2015 with the MINIDEX commissioning run (Run 1). In this run, which is not part of this thesis, the first measurement of muon-induced neutrons in lead was carried out [1, 121]. The experimental setup of the commissioning run had two shortcomings. The first one was an unexpected low detection efficiency, observed for both employed scintillators. The second deficiency was the missing possibility to identify muons that pass through target material only. In the improved MINIDEX setup of Run 2 and Run 3 these shortcomings were fixed.

In the following, the experimental setup, the working principle and the individual detectors of MINIDEX Run 2 and Run 3 are presented.

4.1 Experimental Setup

The MINIDEX setup is $\approx 1.5\,\text{m}$ high, $\approx 1.5\,\text{m}$ long and $\approx 1\,\text{m}$ wide. A cross section of the MINIDEX Run 2 and Run 3 setups is presented in Fig. 4.1. In the centre of the setup two high-purity germanium detectors are deployed. The germanium detectors are surrounded by a plastic tank filled with purified water. The water tank is enclosed by the target material. In any spatial direction there

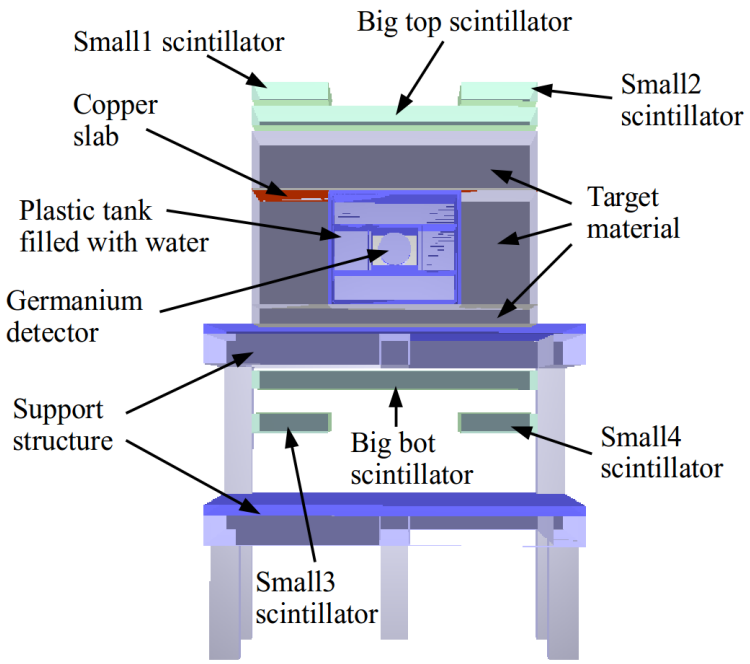

Figure 4.1: Cross section of the MINIDEX Run 2 and the Run 3 setup. A total of eight detectors, consisting of six scintillators (Big top, Big bot, Small1 - Small4) and two high-purity germanium detectors, are employed in the setup. The setup has a footprint of $\approx 1\,\mathrm{m}^2$ and a height of $\approx 1.5\,\mathrm{m}$.

is at least a layer of 8 cm of water between the germanium detectors and the target material. A 0.5 cm thin copper slab is installed directly above the water tank. This slab protects the fragile water tank from the weight of the target material above (several hundreds of kg). Two big scintillators (Big top and Big bot) and four small scintillators (Small1 - Small4), all 5 cm thick, were installed above and below the target. The two big scintillators have a size of 75 cm × 65 cm whereas the four small scintillators have a size of 20 cm × 65 cm. Nearly all experimental parts of the MINIDEX commissioning run [121] were reused in MINIDEX Run 2 and Run 3 (at the same position within the setup). However, the used big scintillators of the commissioning run were removed and new ones were installed. In comparison to the commissioning run, which was operated with two big scintillators only, the four additional small scintillators of MINIDEX Run 2 and Run 3 allow for an identification of muons passing through target material only (see also Section 4.2). The parts of the target material which are covered by the small scintillators (and parts of the big scintillators) on each side of the setup are called target walls in the following. All six scintillators of MINIDEX Run 2 and Run 3 were newly purchased to replace and extend the scintillator

system of the MINIDEX commissioning run. The replacement of the old scintillators was necessary, as their muon detection efficiencies were measured to be only $\approx 90\,\%$ [121]. These deteriorated muon detection efficiencies resulted from a special detector design, where the photomultiplier tube, PMT, was directly incorporated into the scintillating material. Detailed information on the spatial positioning of all important MINIDEX Run 2 and Run 3 setup components can be found in Fig. 4.2 (all other values can be found in [121]).

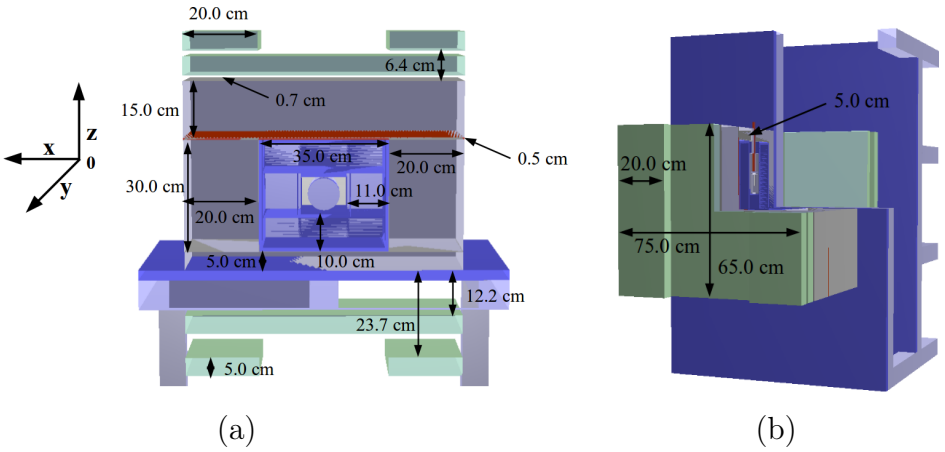

Figure 4.2: Cross section (front view) in (a) and top view in (b) of the MINIDEX Run 2 and the Run 3 setup. Relevant dimensions of the setups are given.

Pictures of the fully assembled MINIDEX Run 2 and Run 3 setups are shown in Fig. 4.3. In Fig. 4.3(a) the Run 2 setup, for which the target consisted of lead only (density: $11.34\,\mathrm{g\,cm^{-3}}$), is shown. Fig. 4.3(b) shows the Run 3 setup for which the lead in the left target wall was replaced by copper (density: $8.96\,\mathrm{g\,cm^{-3}}$). While in Run 2 only lead was studied, the Run 3 setup allows for the simultaneous investigation of lead and copper. The total weight of the setups, which are dominated by the mass of the target material, is ≈ 2 tonnes.

4.2 Working Principle and Muon-Induced Neutron Signature

MINIDEX is designed to measure muon-induced neutrons produced in high-Z materials. Neutrons from such materials are difficult to investigate. In the case of MINIDEX the neutrons have to leave the target, making the neutron detection nearly independent of the muon detection. As a consequence, the signals from the

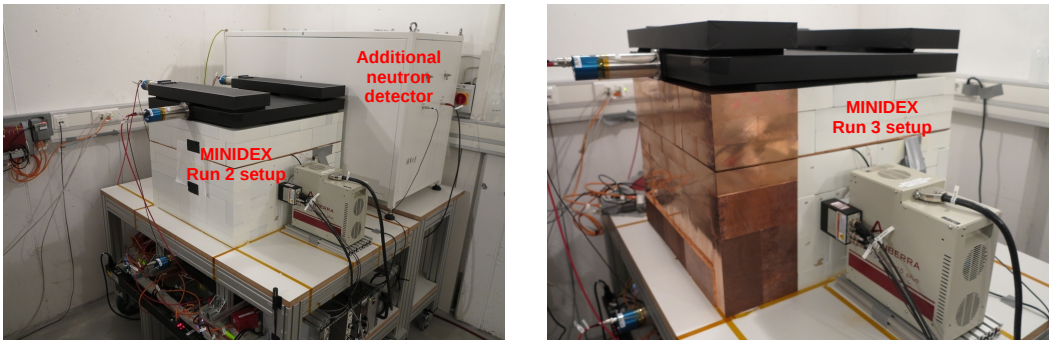

(a) (b)

Figure 4.3: Pictures of the fully assembled MINIDEX Run 2 (a) and Run 3 (b) setups. The three scintillators above the target, the target as well as part of the electronics are visible. The three scintillators below the target, except for the PMT of the Big bot scintillator, are hidden by the tabletop. In (a) an additional neutron detector, installed for a few months next to the MINIDEX Run 2 setup [120] and discussed in Section 3.3, can be seen.

neutrons do not have to be distinguished from large muons backgrounds. However, this leads to rather low detection efficiencies for the muon-induced neutrons. The working principle for measuring muon-induced neutrons with MINIDEX is depicted in Fig. 4.4. Muons (μ) that pass through the target material are identified with help of the installed scintillators. The muons can either directly produce neutrons (n) in muon-nuclear reactions (see Fig. 4.4(a)) or indirectly via muon-induced particles like gammas or protons (see Fig. 4.4(b)). After propagating through the target material, some of these neutrons enter the water tank and get thermalised. Thermalised neutrons can get captured on hydrogen atoms in the water, leading to an exited deuterium nucleus. The subsequent de-excitation of the nucleus is followed by the emission of a $(2223.259 \pm 0.001)\,\mathrm{keV}$ [122] gamma (γ), called 2.2 MeV gamma in the following. Such a neutron capture gamma can be detected by one of the two installed high-purity germanium detectors.

Muons that pass through target material only (i.e. through a target wall only) are identified with the help of the six scintillators. This is accomplished by requesting energy depositions (above a threshold) within a short time in four scintillators on one side of the setup (e.g. Big top + Big bot + Small1 + Small3). Such an event is called a muon tag (also tagged muon) in the following and can occur on both sides of the setup. A schematic example for a muon, generating a muon tag on the left side of the setup, is depicted in Fig. 4.4(a). Following

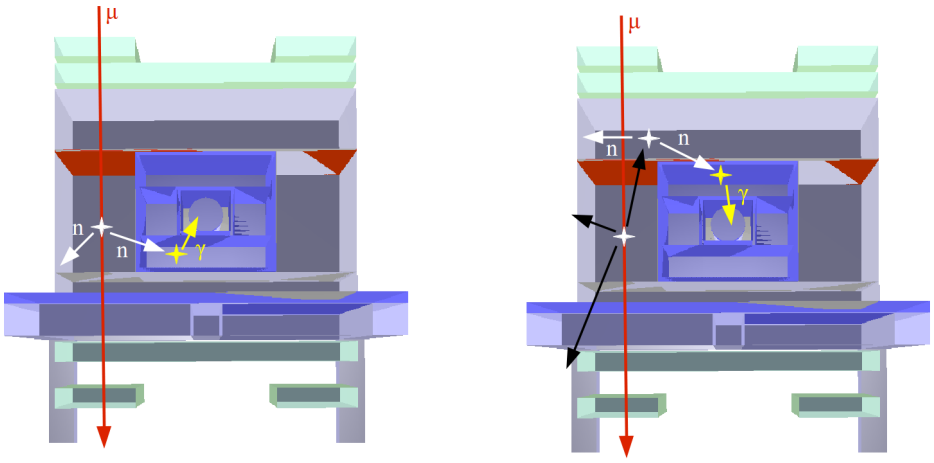

(a) (b)

Figure 4.4: Illustration of the MINIDEX working principle. Muons (μ) that pass through the target material of the setup are identified with the help of the scintillators. The muons can either directly (a) or indirectly (b) produce neutrons (n) during their passage. If any of these neutrons reaches the water tank, it can get thermalised and afterwards captured on hydrogen. Such a capture is followed by the release of a 2.2 MeV gamma (γ), which can get detected by one of the two installed high-purity germanium detectors.

an observed muon tag, delayed 2.2 MeV neutron capture gammas are searched for with the two installed high-purity germanium detectors. The signature of an identified muon-induced neutron that follows a muon tag, called neutron signal in the following, is a detected 2.2 MeV neutron capture gamma within a predefined time window. All search details for neutron signals are given in Section 6.2 for the simulation data and in Section 7.1 for the experimental data.

4.3 Detectors and Electronics

In MINIDEX Run 2 and Run 3 six scintillators and two germanium detectors were operated. In the following, the used detectors as well as the employed electronics of the MINIDEX setup are described.

4.3.1 Scintillators

The six scintillators that are used in MINIDEX Run 2 and Run 3 are commercially available scintillation detectors, purchased from Saint-Gobain [123]. The scintillating material is BC-408 (polyvinyl toluene: $C_{10}H_{11}$), which has a density

of $1.032\,\mathrm{g\,cm^{-3}}$ [124]. Each of the scintillators is equipped with a 51 mm type 9266KFLB PMT from ET Enterprises [125]. A picture of the three scintillators, which are positioned above the target, can be seen in Fig. 4.5. The operational

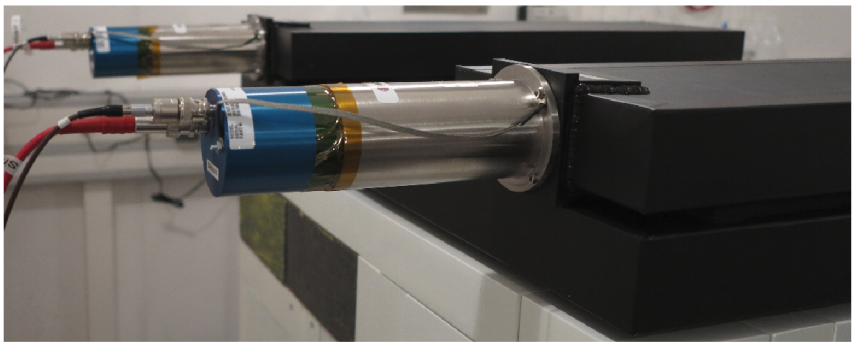

Figure 4.5: Picture of the three scintillators that are located above the target. The PMTs of the two small scintillators as well as the scintillating material, completely wrapped in black foil, are visible. The PMT of the Big top scintillator can not be seen, as it points towards a different direction than the PMTs of the small scintillators.

voltage of each individual scintillator was optimised to maximise its muon detection efficiency. This was carried out by varying the operational voltages and requesting coincident signals in two scintillators, which are stacked on top of each other. A detailed description of this procedure can be found in [126]. The operational voltages of the six MINIDEX Run 2 and Run 3 scintillators are given in Table 4.1.

Table 4.1: Operational voltages of the six MINIDEX Run 2 and Run 3 scintillators. In order to maximise the muon detection efficiency, the voltage of each individual scintillator was optimised.

	Small1	Small2	Small3	Small4	Big top	Big bot
Voltage [V]	− 840	− 875	− 890	− 840	− 1030	− 1070

4.3.2 Germanium Detectors

The two installed germanium detectors of the MINIDEX setup are commercially available extended range coaxial high-purity p-type germanium detectors produced by Mirion [127, 128]. This type of detector is used for gamma

spectroscopy in the energy range of 3 keV up to about 10 MeV. A cross section of such a detector, made out of a cylindrically shaped germanium crystal, together with the housing of the cryostat is schematically depicted in Fig. 4.6. The two germanium crystals employed in MINIDEX have a diameter of

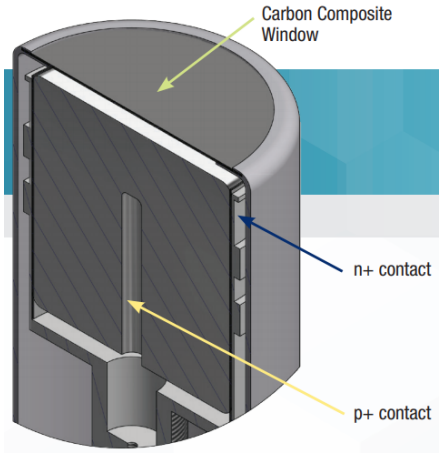

Figure 4.6: Cross section of an extended range high-purity germanium detector. Two detectors of this type are employed in the MINIDEX setup. Taken from [128].

(69.0 ± 0.5) mm/(70.5 ± 0.5) mm, a length of (72.0 ± 0.5) mm/(63.5 ± 0.5) mm, a (45.0 ± 0.5) mm/(37.5 ± 0.5) mm deep borehole with a diameter of (9.5 ± 0.5) mm in the centre and a mass of (1.416 ± 0.031) kg/(1.305 ± 0.029) kg, respectively. Both detectors have a (1.0 ± 0.5) mm thick dead layer on the n+ contact [128] and are operated at temperatures around -185°C. The detectors are electrically cooled via a copper cold finger, which connects the germanium crystals with two dedicated cooling units (Cryo-Pulse 5 Plus [129]). These cooling units are located outside the target material and can be seen in Fig. 4.3. Due to the electrical cooling work-intensive refilling of liquid nitrogen dewars (often related to the usage of germanium detectors) is unnecessary. The two high-purity germanium detectors of MINIDEX are operated at 3000 V and 3500 V, the operating voltages specified by the producer.

4.3.3 Electronics and Data Acquisition

The operating voltages of the six scintillators and the two germanium detectors are provided by different voltage devices (e.g. iseg NHQ 206L module [130]). To withstand short blackouts, the setup is equipped with an uninterruptible power supply (model: Online XSR3000).

The readout of the scintillators and the high-purity germanium detectors is handled by a flash analog-to-digital converter (FADC) from Struck (model: Struck SIS3316-DT [131]). This FADC runs with a 16 channel VME digitiser card that records traces with a 250 MHz sampling rate and a 14 bit resolution. Each of the 16 channels can be triggered independently and the determined information of the events are recorded. For each energy deposition in the germanium detectors, the amplitude of the charge signal and the corresponding time stamp are stored. A minimal time difference between two recorded consecutive energy depositions in the same germanium detector (i.e. the dead time of the germanium detectors) of $(20.3 \pm 0.1)\,\mu$s was found. For each energy deposition in the scintillators, which is associated to the measured light output, the amplitude of the current signal and the corresponding time stamp are stored. The minimal possible time difference for energy depositions within the same scintillator (i.e. the dead time of the scintillators) was determined to be $(1.2 \pm 0.1)\,\mu$s. As no external trigger is utilised in MINIDEX, all energy depositions above predefined thresholds are recorded. These thresholds are set to $\approx 3\,$MeV for any of the scintillators and $\approx 20\,$keV for the two germanium detectors. All recorded energy depositions are stored on a server from sysGen (model: SuperServer 5018D-MTF [132]) and are analysed offline.

Besides the discussed six scintillators and the two germanium detectors, used to identify muon-induced neutrons, also the fill level of the water in the tank was monitored. A Vegetronix [133] sensor was used for this purpose. Monitoring of the water fill level is necessary, as a significantly decreased fill level in the tank would lead to a significantly lower efficiency for neutron thermalisation and neutron capture. However, no significant reduction of the water content in the tank (meaning $\ll 1\,\%$) was found for any of the runs.

Chapter 5

Characterisation of Detectors, Data Selection and Experimental Data Sets

In order to acquire reliable experimental data sets, the employed detectors of the MINIDEX Run 2 and Run 3 setup were characterised. In the following, the characterisation studies, including the energy calibration of the individual detectors, are introduced. Additionally, the muon tag determination procedure and the generated experimental data sets are discussed.

5.1 Characterisation of Detectors

5.1.1 Stability of Data Taking

In order to guarantee stable data taking for each MINIDEX run, all individual detectors were constantly monitored for their stability. For this purpose, the online monitoring system [121] that was implemented in the context of the MINIDEX commissioning run was used. It provides the possibility to notice discontinuities in the signal amplification or changes of the energy resolution of the detectors quickly. The monitoring data show that smooth data taking periods of the discussed runs within this thesis were accomplished.

5.1.2 Scintillators

5.1.2.1 Energy Calibration

The energy calibration of the individual scintillators was carried out with the help of simulation predictions for the measured energy spectrum. For the calibration

procedure the scintillator spectra without the request for any coincidence, which are therefore the most independent ones, were used. For each scintillator the position of the most probable value of the Landau distribution of the experimental light output spectra was set to the corresponding energy value provided by simulation. The simulated most probable energy was found to be around 10 MeV for each big and small scintillator as well as for each run. Note, the light collection efficiency and the resolution of each individual scintillator is assumed to be independent from the location of the energy deposition within the panel.

5.1.2.2 Muon Detection Efficiencies

The efficiencies of the six scintillators to identify muons passing through the scintillating material were determined. This was carried out above the Earth's surface by stacking all six scintillators on top of each other. The PMTs of the small scintillators were pointing to the same direction. Furthermore, the PMTs of the two big scintillators were also aligned. The setup that was used to determine the muon detection efficiencies of the Small1, Small4, Big top and Big bot scintillators is depicted schematically in Fig. 5.1. Through-going muons were identified

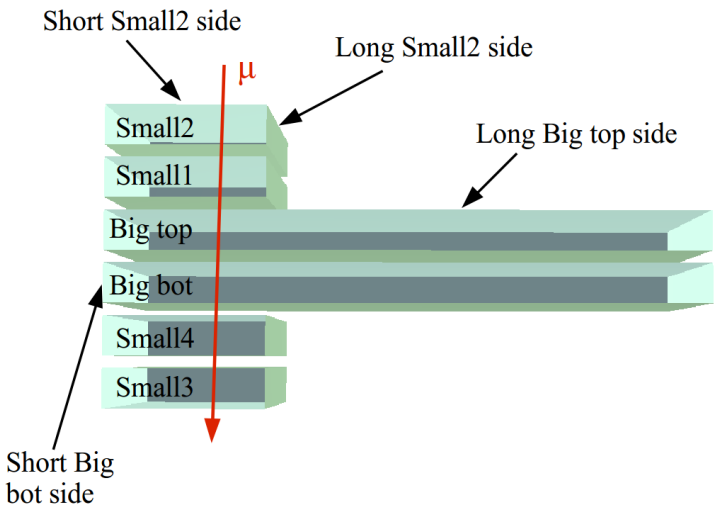

Figure 5.1: Cross section of the setup that was used to determine the muon detection efficiencies of the Small1, Small4, Big top and Big bot scintillators. The efficiencies were determined by requesting coincident and high-enough energy depositions within different scintillators. The PMTs of all small and big scintillators are mounted on the short side of the corresponding panel. See text for details.

with the help of the two outermost scintillators, in the depicted case Small2 and

Small3. This is achieved by requesting coincident signals in both scintillators within ± 30 ns (for the choice of ± 30 ns see Section 5.2). In order to select single muons only (i.e. only one muon and no further particle) that pass through the scintillators, the signals are required to be located within the peaks of the Landau distributions. This measure leads to the suppression of particle showers as well as energy depositions from particles that are not minimum ionising. The peaks of the Landau distributions in the corresponding scintillator spectra, as shown in Fig. 5.2, were fit with Gaussian functions. The most probable energy of each

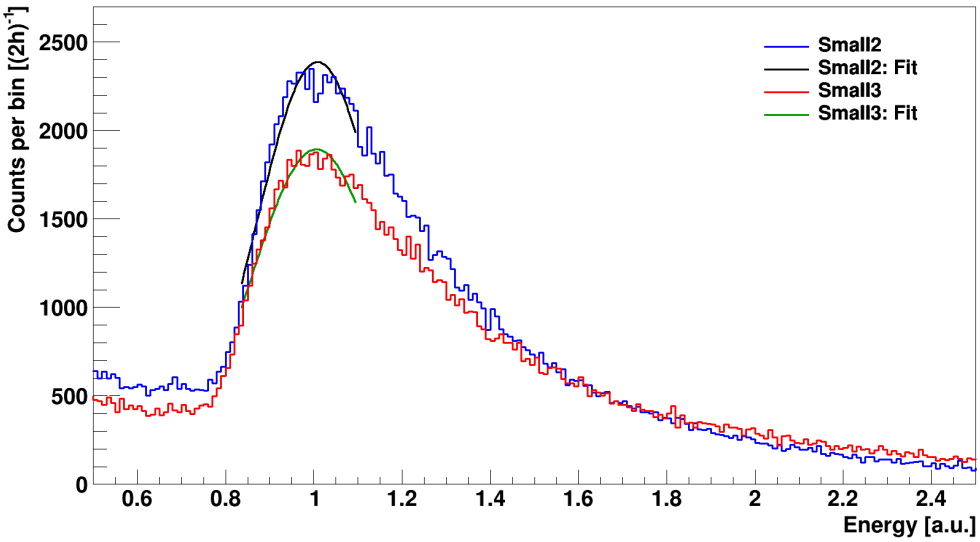

Figure 5.2: Zoom on the peaks of the Landau distributions of the measured Small2 and Small3 scintillator spectra before any cuts. The shown data were acquired in a 2 h measurement with the help of the setup schematically depicted in Fig. 5.1. Both Landau peaks were fit with a Gaussian function and the determined most probable energies were set to a value of 1.

Landau distribution was set to a value of 1. Only energy depositions within the FWHM (Small2: 0.84 to 1.16, Small3: 0.82 to 1.18) of the Gaussian fit functions are used. It can be seen that the rate of events in Small3 in the chosen energy range is smaller than the corresponding rate of events in Small2. This likely results from the shielding of muons by the scintillators above Small3. Furthermore, particles that are induced in the scintillators above Small3 by the through-going muons can lead to additional energy depositions. As a consequence, the Small3 energy spectrum becomes harder, and thus, only a smaller number of signals appear in the peak of the Landau distribution. This seems to be confirmed by the

observable higher number of signals with energies > 1.8 in Small3 compared to Small2.

Following an identified single through-going muon, all energy depositions in the other four scintillators above a value of ≈ 0.75 and within ± 30 ns were counted. As the energy spectra of the four investigated scintillators are similar to the ones in Fig. 5.2, the applied energy cut of ≈ 0.75 selects all events within the Landau distributions. With the discussed method and by using a further data set, acquired for a setup in which the Small1 and the Small4 scintillator enclose the other panels (same PMT positioning as before), the muon detection efficiencies of all six scintillators were determined and are given in Table 5.1. As all values are $> 99\,\%$, a reliable identification of muons with the MINIDEX

Table 5.1: Muon detection efficiencies of the six MINIDEX Run 2 and Run 3 scintillators. Two dedicated setups, one schematically depicted in Fig. 5.1, were used to determine these efficiencies. The given systematic uncertainties on the detection efficiencies of the big scintillators result from the obtained differences between the values determined with the two setups.

	Muon detection efficiency [%]
Small1	$99.37\,^{+0.13}_{-0.16}\,(\text{stat})$
Small2	$99.57\,^{+0.17}_{-0.27}\,(\text{stat})$
Small3	$99.40\,^{+0.20}_{-0.26}\,(\text{stat})$
Small4	$99.70\,^{+0.09}_{-0.11}\,(\text{stat})$
Big top	$99.77\,^{+0.08}_{-0.10}\,(\text{stat}) - 0.29\,(\text{syst})$
Big bot	$99.77\,^{+0.08}_{-0.10}\,(\text{stat}) - 0.37\,(\text{syst})$

Run 2 and Run 3 setup is feasible. The small percentage of undetected muons can be explained by a non-perfect alignment of the scintillators in the performed measurements. The stated systematic uncertainties on the efficiencies of the big scintillators result from the difference between the values obtained with the two setups. Note, the determined muon detection efficiencies of the MINIDEX Run 2 and Run 3 scintillators are significantly higher than the unexpected low muon detection efficiencies of the MINIDEX commissioning run scintillators (see Section 4.1).

5.1.2.3 Estimation of Energy Resolution

The data set of the measurement that was introduced in detail in the previous section (acquired with the setup depicted in Fig. 5.1) was also used to estimate the energy resolution of the scintillators. The applied method, which is slightly different for the small and the big scintillators, is demonstrated as an example for Small1 and Big bot.

For the small scintillators, first single through-going muons were identified with the help of coincident energy depositions in the two outermost scintillators of the setup (Small2 and Small3). A zoom on the energy spectra of the Small2 and Small3 scintillators (without any cuts) was shown in Fig. 5.2. For coincidences of the Small2 and the Small3 scintillator only events that occur within $\pm 30\,\text{ns}$ (for the choice of $\pm 30\,\text{ns}$ see Section 5.2) and within an energy range from 0.8 to 1.2 were considered. Note that these are not the final energy cuts for coincident signals in Small2 and Small3, as discussed in the following. The chosen energy range roughly corresponds to the FWHM of the peaks of the Landau distributions (obtained from fits with Gaussian functions, see Section 5.1.2.2). This energy range was chosen as the majority of energy depositions occurring in this range originates from single muons passing through a scintillator. The selected energy range of 0.4 is split up into energy slices with 0.1 width each. In order to select the same type of events in both scintillators (i.e. the same amount of energy is deposited at the same position within the scintillator[1]), it is requested that both events occur within the same energy slice. Following a selected muon in the Small2 and the Small3 scintillator, all events in the Small1 scintillator within $\pm 30\,\text{ns}$ are recorded. As Small1 was located in the measurement directly beneath the Small2 scintillator (see Fig. 5.1), it is expected that Small1 observes the same type of events as Small2. In Fig. 5.3 the difference between measured energies in Small2 and Small1 is depicted for the four chosen energy slices. Distributions with different shapes can be observed, owing to the selection of different event types by the four individual energy slices. In Fig. 5.3 also the distribution, which results from the summation of the spectra of the individual energy slices, is shown in magenta. The width of this distribution depends on the energy resolution of the Small1 scintillator but also on other quantities, like the energy resolution of the Small2 scintillator and the precision of the event type selection[2]. Thus, only

[1] The reconstructed energy depends on the location of an energy deposition within a scintillator. This effect is discussed in Section 5.2.

[2] For example, if the position of an identified through-going muon in the Small1 scintillator deviates from the position in Small2, then a similar energy deposition can lead to a different reconstructed energy.

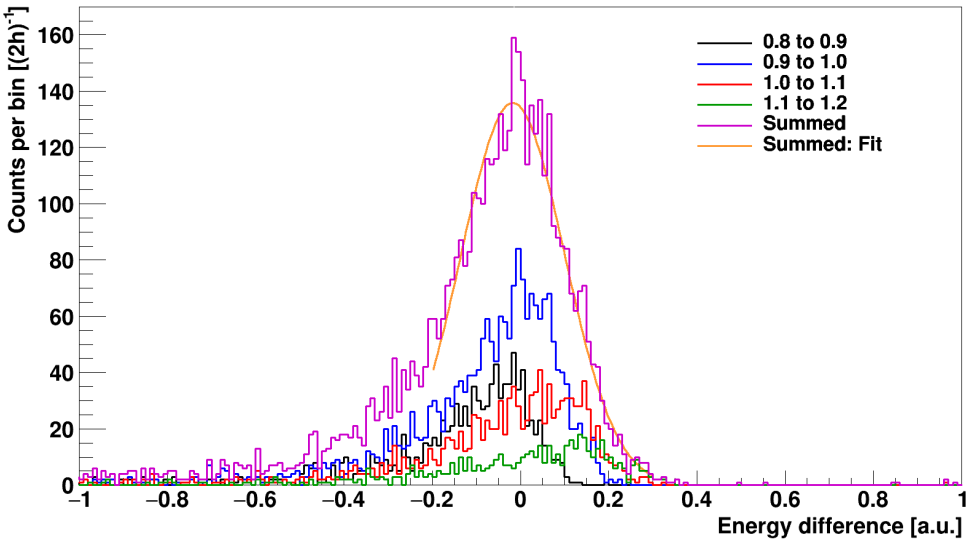

Figure 5.3: Measured differences between energy depositions in the Small2 and the Small1 scintillator for different selected energy slices. Only events that were acquired in a 2 h measurement with the setup schematically depicted in Fig. 5.1 are considered. The shown energy differences result predominantly from through-going muons, identified with the help of the two outermost scintillators (Small2 and Small3) of the setup. A Gaussian fit (orange) on the distribution, which sums up the events of the individual energy slices, yields an upper limit on the energy resolution of the Small1 scintillator. See text for details.

an upper limit on the energy resolution of the Small1 scintillator can be assessed with the described method. This limit is determined by fitting the peak of the summed up distribution with a Gaussian function, as shown in orange in Fig. 5.3. A σ of 0.117 ± 0.002 was obtained for the Gaussian function. Together with an energy of ≈ 10 MeV at the most probable value of the Landau distribution (see Section 5.1.2.1) this yields an upper limit on the energy resolution of the Small1 scintillator of 1.2 MeV (σ). This upper limit on the energy resolution is taken for all four small scintillators.

For the estimation of the energy resolution of the big scintillators, the muons identified by the Small2 and Small3 scintillators can not be used. The event types of these muons differ significantly from the event types that would be obtained for example for Big top (for these muons), owing to a different scintillator size as well as a different PMT location (see Fig. 5.1). As a consequence, only the Big top scintillator was used to identify single through-going muons. In order to select predominantly single muons, the peak of the Landau distribution in the

spectrum of the Big top scintillator, as shown in Fig. 5.4, was fit with a Gaussian function. Only energy depositions that occur within an energy range from 0.8

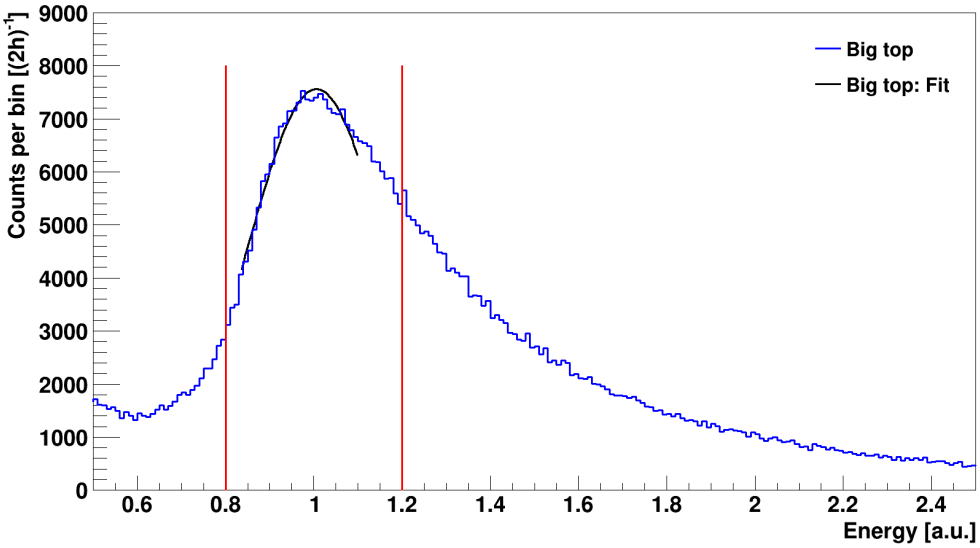

Figure 5.4: Zoom on the peak of the Landau distribution of the measured Big top scintillator energy spectrum before any cuts (blue). The energy of the most probable value of the Landau distribution was set to a value of 1. In black a Gaussian fit applied to the peak of the Landau distribution, used to identify single through-going muons, is displayed.

to 1.2 (indicated by red lines), roughly corresponding to the FWHM (0.37) of the Gaussian fit (black), are selected. As only one scintillator was used for the identification of single muons, no slicing of the energy range was performed. All energy depositions in the Big bot scintillator that occurred within ± 30 ns of an identified muon in the Big top scintillator are collected. As Big bot was positioned directly beneath Big top (see Fig. 5.1), the same type of events are expected to be observed in both scintillators. The obtained spectrum, representing the differences between measured energy depositions in the Big top and the Big bot scintillator, is depicted in Fig. 5.5. A peak around an energy difference of 0 can be observed. The width of the peak results from the energy resolution of the Big bot scintillator but also from other quantities (as discussed for the small scintillators). The peak was fit with a Gaussian function and a σ of 0.149 ± 0.001 was obtained. Together with an energy of ≈ 10 MeV at the most probable value of the Landau distribution (see Section 5.1.2.1) an upper limit on the energy resolution of Big

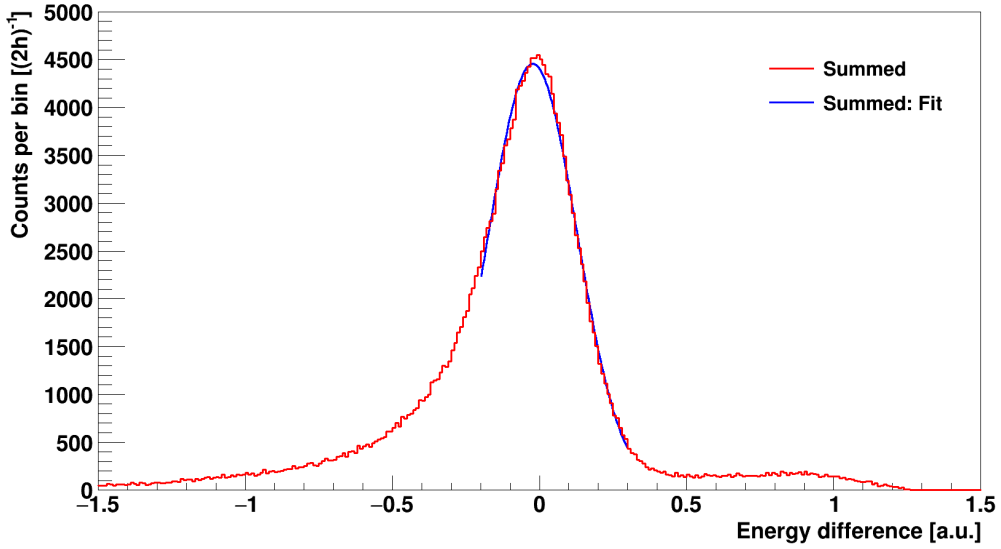

Figure 5.5: Measured energy differences between coincident energy depositions in the Big top and the Big bot scintillator. For the Big top scintillator only energy depositions within an energy range of 0.8 to 1.2 are considered. With the help of an applied Gaussian fit function (blue) upper limits on the energy resolution of the big scintillators were determined. See text for details.

bot of 1.5 MeV was determined. The determined value of 1.5 MeV (σ) is taken as an upper limit on the energy resolution for both big scintillators.

The determined upper limit on the energy resolution of the big scintillators is worse than the upper limit on the energy resolution of the small scintillators. This could result from a less position dependent light collection for energy depositions in the small scintillators compared to energy depositions in the big scintillators. However, it could also arise from the more precisely selected event types in the case of the small scintillators.

5.1.2.4 Stability of Muon Detection

It is assumed that the muon detection efficiencies of the MINIDEX scintillators are stable over the runtimes of the MINIDEX runs. To test this assumption, two studies were carried out.

In the first study, the stability of the signal amplification in the scintillators was investigated. A possible source of instability could originate for example from an unstable high voltage supply. For this purpose, the spectra of each scintillator (without any cuts), recorded at different times within a MINIDEX run, were investigated. As an example, in Fig. 5.6 the spectrum of the Big top scintillator is

depicted for five different times within the MINIDEX Run 2 data taking period. Each individual spectrum represents the energy depositions that were collected

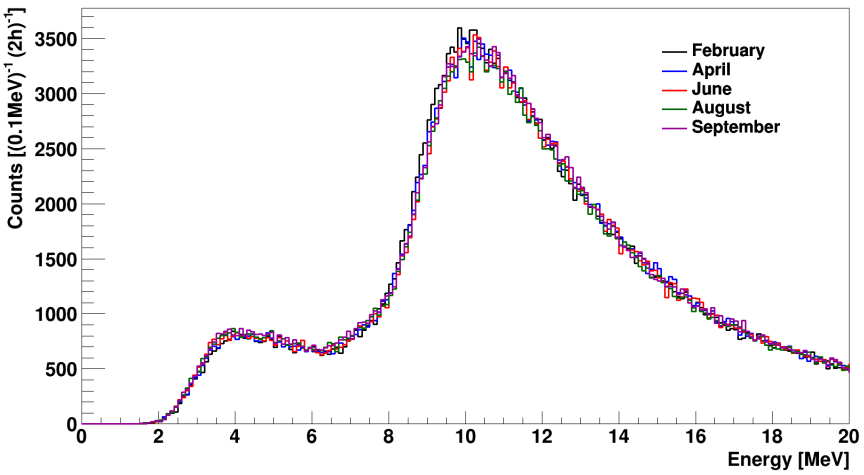

Figure 5.6: Measured energy spectrum of the Big top scintillator, recorded at different times within the MINIDEX Run 2 data taking period. Each spectrum represents the energy depositions collected within 2 h of measurement.

within a continuous 2 h measurement. In Table 5.2 the corresponding most probable values for the depicted Big top spectra, determined with the help of Landau fits, are given. A significant shift of the position of the Landau distribution was

Table 5.2: Most probable values of the measured Big top energy spectra that are depicted in Fig. 5.6. The values were determined with the help of Landau fit functions. All given uncertainties are statistical only.

	Most probable value [MeV]
February	10.53 ± 0.04
April	10.68 ± 0.03
June	10.65 ± 0.05
August	10.67 ± 0.02
September	10.65 ± 0.03

observed for one of the measured Big top spectra only. For any scintillator and run the maximal observed shifts were found to be < 200 keV. As these are only

small shifts, only a single energy calibration for each scintillator and run was performed. However, the observed changes of the scintillator signal amplification are taken into account in the investigation of systematic uncertainties (see Section 8.3.1).

In the second study the evolution of the muon rate was investigated and thus further information on the stability of the muon detection efficiency can be obtained. For this purpose, the rate of detected muons in the MINIDEX Run 2 and Run 3 data taking period (total runtime of ≈ 470 days) was analysed. The corresponding data were acquired from January 2016 until July 2017, with Run 3 starting in November 2016. Only the rate of big tag coincidences (i.e. the rate of coincidences between the Big top and the Big bot scintillator, for a detailed description of big tags see Section 5.3), $R_{\text{Big tag}}$, was taken for this investigation, as the rate of muon tags was found to be statistically insufficient for this study. Note that simulation predicts that $R_{\text{Big tag}}$ is dominated by actual muons passing through the setup. As the experimental MINIDEX Run 2 and Run 3 data sets were combined for this analysis, a normalisation of $R_{\text{Big tag}}$ of Run 3 had to be performed. This normalisation is necessary as in Run 3 (compared to Run 2) the left target wall was made up of copper. Copper has a $\approx 20\,\%$ lower density than lead, leading to a reduced shielding of muons by the copper target wall in Run 3 and thus to a higher $R_{\text{Big tag}}$. To take this effect into account, $R_{\text{Big tag}}$ of Run 3 was reduced by $\approx 1\,\%$. This value was determined with the help of simulation. After normalising $R_{\text{Big tag}}$ of Run 3, the spectrum shown in Fig. 5.7(a) in blue is obtained. The transition from Run 2 to Run 3 is indicated by the black vertical line. In Fig. 5.7(b) a zoom on the time axis, representing the acquired data from the end of November 2016 until the start of March 2017, is depicted. A change of $R_{\text{Big tag}}$ by a few percent over the whole measurement period of Run 2 and Run 3 can be observed. In addition to $R_{\text{Big tag}}$, also the modified atmospheric air pressure, $P_{\text{Mod. air}}$, is displayed in red. $P_{\text{Mod. air}}$ is defined by

$$P_{\text{Mod. air}} = P_{\text{Air}} - 2 \cdot (P_{\text{Air}} - \overline{P}_{\text{Air}}). \tag{5.1}$$

Here P_{Air} represents the measured air pressure[3] (for the individual points in time) while $\overline{P}_{\text{Air}}$ represents the mean air pressure (averaged over the whole runtime of Run 2 and Run 3). A correlation between $R_{\text{Big tag}}$ and $P_{\text{Mod. air}}$ is apparent in Fig. 5.7, showing that $R_{\text{Big tag}}$ is inversely proportional to P_{Air}. This can be explained by the correlation between the energy loss of muons in the atmosphere

[3]The air pressure was measured and provided by the Deutscher Wetterdienst for Echterdingen, a small town only ≈ 15 km away of the MINIDEX setup location [134].

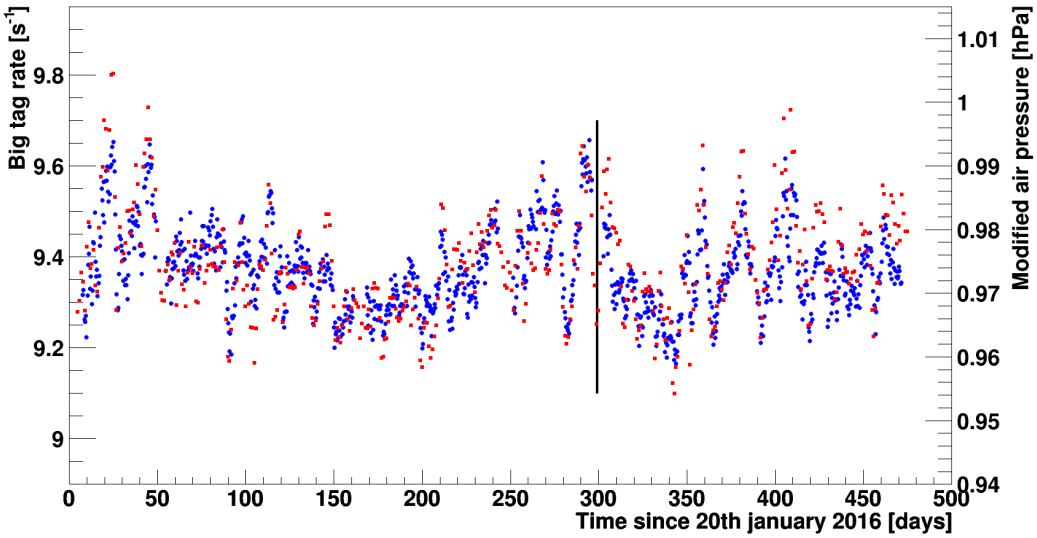

(a)

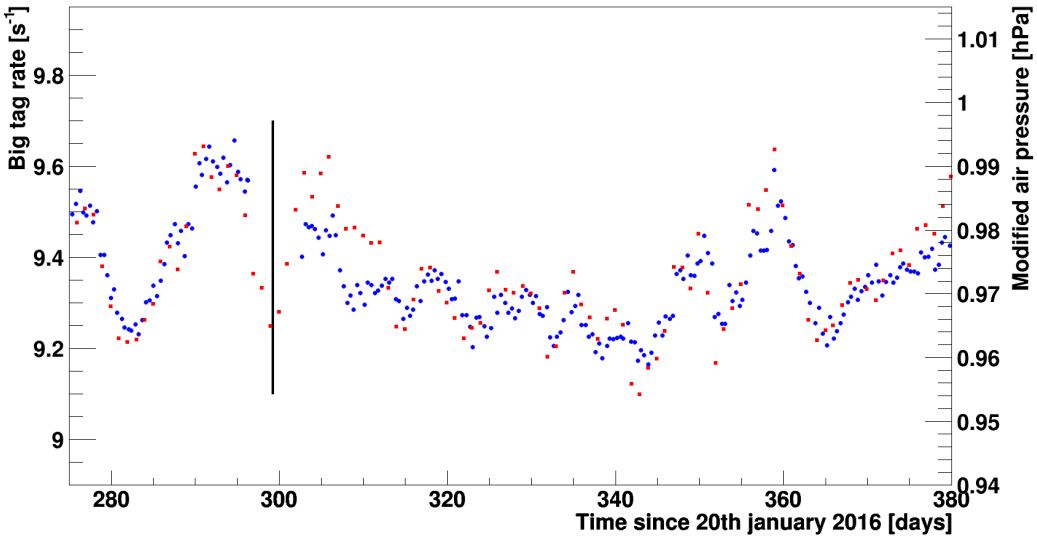

(b)

Figure 5.7: Measured time evolution of the MINIDEX big tag rate (blue) and the modified atmospheric air pressure (red) at the experimental site. In (a) the acquired experimental data from January 2016 until May 2017 are drawn. The black vertical line indicates the transition of MINIDEX Run 2 to Run 3. In (b) a zoom on the time axis from the end of November 2016 until the start of March 2017 is shown. See text for details.

and P_{Air}. For example, a high P_{Air} leads to an increased energy loss of muons in the atmosphere. Consequently, less muons can reach the MINIDEX setup and induce a big tag.

Summarising, the investigations performed confirm the assumption of stable muon detection efficiencies of the scintillators over the runtimes of MINIDEX Run 2 and Run 3.

5.1.3 Germanium Detectors

5.1.3.1 Energy Calibration

Each germanium detector was calibrated with the help of two gamma lines from natural radioactivity. One gamma line above and one below 2.2 MeV, the energy of the neutron capture gammas, were selected for the calibration. These lines arise due to the decays of ^{40}K and ^{208}Tl isotopes, leading to the emission of 1460.8 keV and 2614.5 keV gamma rays, respectively. Both gamma lines were fit with a Gaussian function plus a first order polynomial distribution. The energy resolution of both germanium detectors was determined to be ≈ 1 keV (σ) at the energies of the gamma calibration lines. From 1460.8 keV to 2614.5 keV a linear behaviour of the relation between the recorded ADC channel and the corresponding deposited energy is expected. A first order polynomial distribution was used to calibrate the germanium detectors. Note that each germanium detector was calibrated individually. In Fig. 5.8 the calibrated energy spectrum of one of the germanium detectors is depicted, representing all measured energy depositions of MINIDEX Run 2. The 2.2 MeV gamma line, resulting from the neutron captures on hydrogen, is expected to occur between the two highlighted calibration lines. Both germanium detectors were calibrated every 10 h during the MINIDEX runs (see next Section).

5.1.3.2 Detector Stability

A variation of the signal amplification within the runtime was observed for both MINIDEX germanium detectors and both runs. This could be accompanied by a slight deterioration of the energy resolution of the detectors. In order to operate the germanium detectors stably, these effects were studied for both germanium detectors and both runs. For the stability of the signal amplification, the position of the two calibration gamma lines were monitored over the whole runtime. This is shown in Fig. 5.9(a) for one of the germanium detectors of Run 2, for which the position of the 2614.5 keV calibration gamma line (determined in ADC

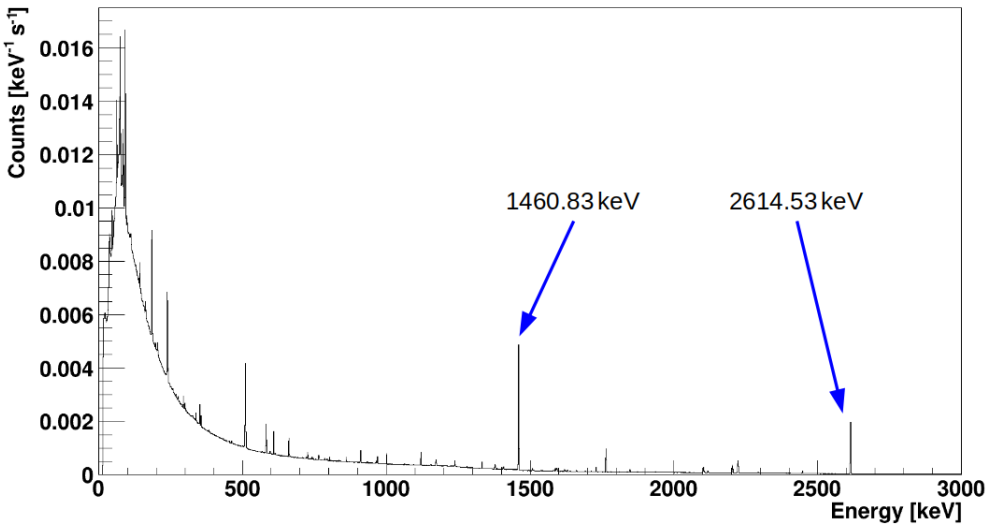

Figure 5.8: Measured energy spectrum of one of the germanium detectors that were operated in MINIDEX Run 2. The two highlighted lines result from gammas following the decays of ^{40}K (1460.8 keV) and ^{208}Tl (2614.5 keV). These gamma lines result from natural radioactivity and were used to calibrate the germanium detectors.

channels) is plotted relative to the first data point. Each data point represents a data set that was recorded for a continuous 10 h measurement. While a slight increase of the signal amplification within the measurement time is apparent, the regular calibrations (every 10 h) guarantee that this is accounted for in the energy reconstruction process. The difference of the reconstructed energies between two calibrated 10 h measurements is below statistical uncertainties. In Fig. 5.9(b) the evolution of the energy resolution (σ) at 2614.5 keV is depicted for the same germanium detector and the same MINIDEX run as in (a). No deterioration of the energy resolution above the statistical uncertainty is found. This holds for both germanium detectors and both runs. Note that for a short period of data taking this did not hold (resulting from an unforeseen warming up of the germanium detectors). However, the acquired data from this period were rejected from the further analysis.

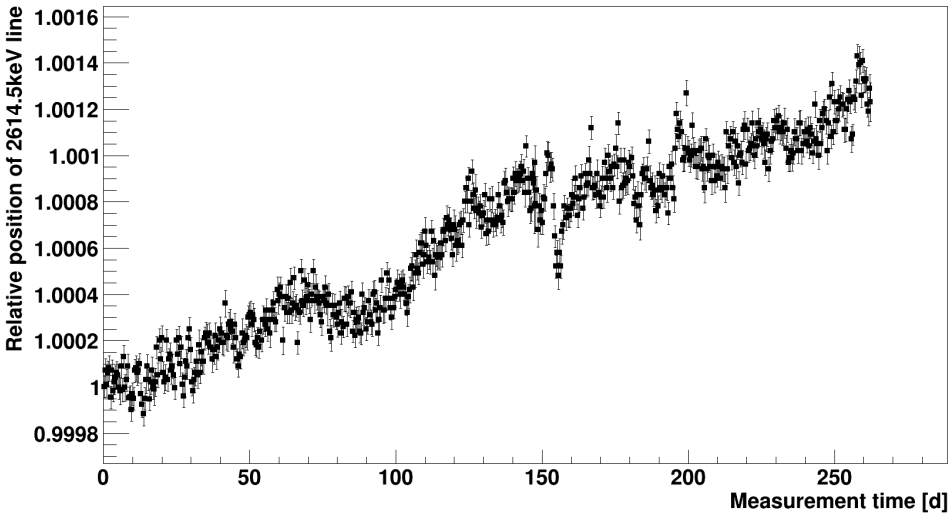

(a)

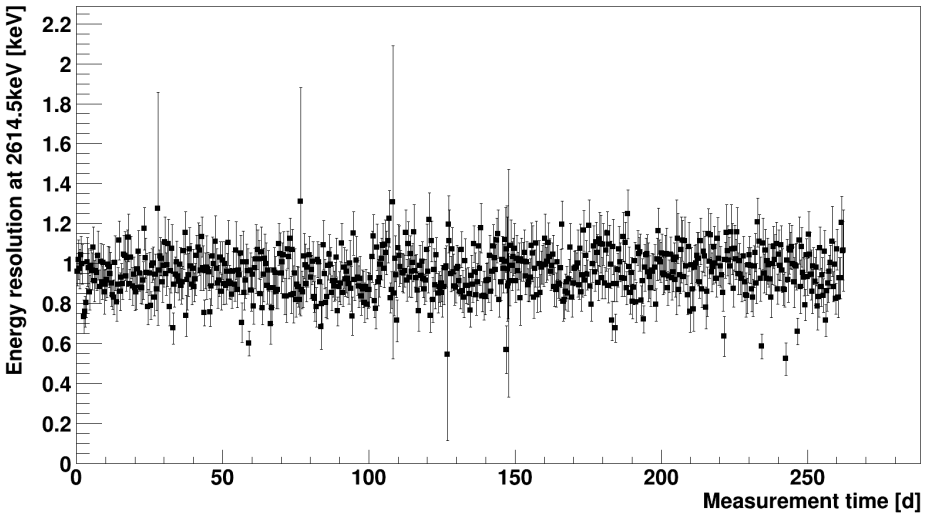

(b)

Figure 5.9: Measured position of the 2614.5 keV gamma line (used for the calibration of the germanium detectors) relative to the first data point in (a). The total increase of the signal amplification is $\approx 1.5\,‰$. In (b) the measured energy resolution (σ) at 2614.5 keV is drawn. Both plots are depicted for one of the two employed germanium detectors, but are similar for both. Each point represents 10 h of data taking in MINIDEX Run 2. The given uncertainties are statistical only and result from fits of the gamma line.

5.2 Muon Tag Determination Procedure and Muon Tag Characteristics

In order to search for 2.2 MeV gammas from the captures of muon-induced neutrons on hydrogen, the corresponding muons have to be identified first. This is achieved by requesting energy depositions > 5 MeV (called scintillator energy cut) in all four scintillators on one side of the setup (e.g. in Small2 + Big top + Big bot + Small4) within a time window of ± 30 ns. Simulation predicts that in $> 95\,\%$ of all muon tags a muon passes through a target wall only. A muon tag, resulting from the passage of a muon through the left target wall, is schematically depicted in Fig. 4.4(a). The requirement for energy depositions in the scintillators above > 5 MeV and within ± 30 ns reduces the contribution of accidental coincidences to the rate of muon tags to negligible contributions. Accidental coincidences can result for example from simultaneous energy depositions of radioactive decays. A detailed investigation of the influence of these backgrounds on the search for neutron signals in MINIDEX can be found in Section 8.3.1.

By selecting an energy cut of 5 MeV, all energy depositions from muons passing through at least 5 cm of scintillator are accepted. The spectrum recorded with the Big top scintillator can be seen in Fig. 5.6. It corresponds to a Landau distribution. The 5 MeV energy cut was determined by interpolating the falling edge of the Landau distribution of each individual scintillator to lower energies. The obtained energy values were found to be all slightly higher than 5 MeV.

The ± 30 ns time window was determined by studying the time differences between energy depositions > 5 MeV in different scintillators on the same side of the setup. In Fig. 5.10 the time differences between measured energy depositions > 5 MeV in the Small2 and the other three scintillators on the right side of the setup are depicted. A distinct peak around 0 ns, which extends up to time differences of ± 30 ns, can be observed in all three spectra. These peaks result from energy depositions that originate from the same muon or its induced particles (e.g. particles induced by the muon during its passage through the laboratory overburden). The width of the peaks is determined by different quantities, including the precision of the time stamp reconstruction algorithm of the ADC. The highest coincidence rate appears for the time differences between the Small2 and the Big top scintillator. As these two scintillators are stacked on top of each other, the probability to detect the same muon (due to the large geometrical acceptance) is high. Furthermore, both scintillators are located above the target and are thus exposed to a higher muon flux than the scintillators below the

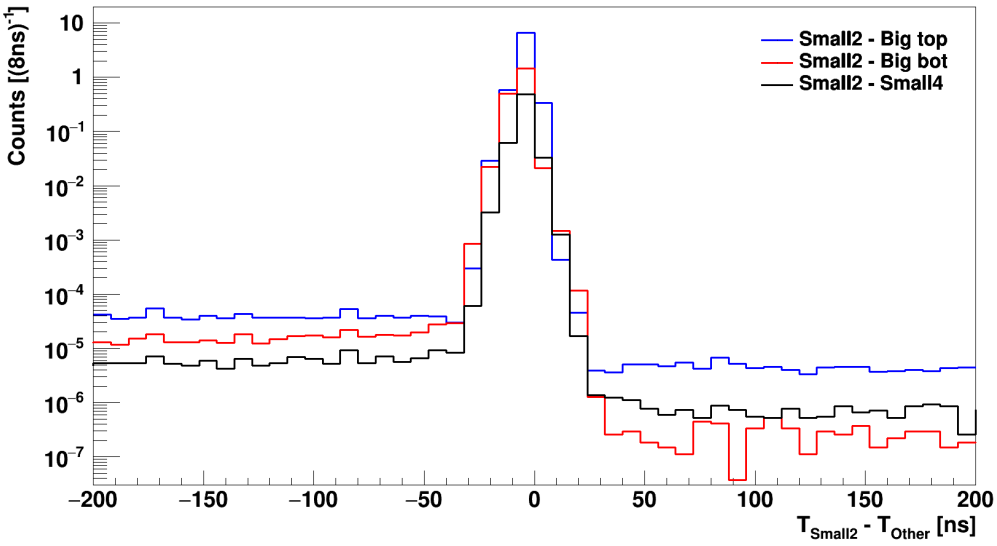

Figure 5.10: Distribution of measured time differences between energy depositions in the Small2 and the other three scintillators on the right side of the MINIDEX Run 2 setup. Only time differences for deposited energies $> 5\,\mathrm{MeV}$ are considered and all shown spectra are normalised to the lifetime of the run.

target[4]. The increased plateau on the left side of each distribution results from the detection of muons in the Small2 scintillator and a delayed energy deposition in the corresponding second scintillator. Such delayed energy depositions might be explained by the decays of muon-induced radioactive isotopes. These isotopes can be produced directly by the muons or by any of the induced particles.

In Fig. 5.11 the energy spectrum of the Big top scintillator is depicted. In blue all events with energy depositions $> 5\,\mathrm{MeV}$ (divided by a factor of 30) are shown. In red only the subset of events for which a muon tag on the right side of the setup was found is displayed. A narrowing of the Landau distribution is apparent for the spectrum that results from the tagged muons. Furthermore, for this spectrum a shift of the most probable value of the Landau distribution towards lower energies can be observed. Both effects result from the selection of muons by the geometrical acceptance of the scintillators, defining the muon tags. The maximum possible angle of a muon with the z-axis, in order to pass through all four scintillators on one side of the setup and therefore lead to a muon tag, is $\approx 55\,°$. Such a muon passes steeper through the scintillators than an average muon and consequently deposits on average less energy. In the spectrum for

[4]A large number of muons with energies $< 1\,\mathrm{GeV}$ can not reach the scintillators on the bottom of the setup, as they get shielded by the target.

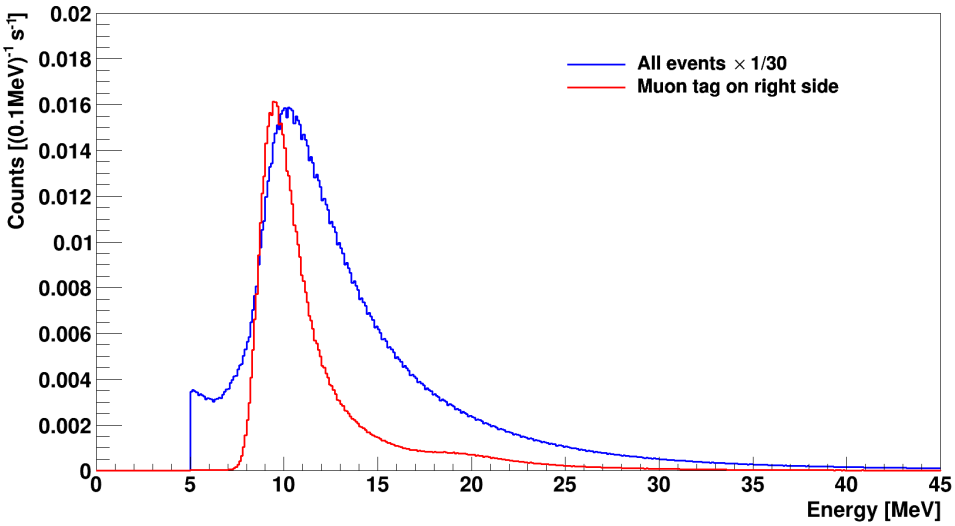

Figure 5.11: Measured energy depositions in the Big top scintillator. In blue all events (divided by a factor of 30) with deposited energies $>5\,\mathrm{MeV}$ are depicted. The subset of events, for which a muon tag on the right side of the setup was found, is shown in red. The small bump at an energy of $\approx 20\,\mathrm{MeV}$ results from the simultaneous passage of a muon and a second minimum ionising particle (mainly muon-induced electrons) through the scintillator. Only events of the experimental MINIDEX Run 2 data set are considered. Both spectra are normalised to the lifetime of the run.

muon tags a small bump can be observed at an energy of $\approx 20\,\mathrm{MeV}$, owing to the simultaneous passage of a muon and a second minimum ionising particle through the same scintillator. Simulation predicts that the majority of these additional particles are muon-induced electrons, created during the passage of the muons through the laboratory overburden.

It was found that the measured energy spectra of the big scintillators differ significantly for muon tags on the left and the right side of the setup. This is shown in Fig. 5.12 for the muon tags found in the MINIDEX Run 2 data set. It is apparent that the most probable values of the scintillator energy spectra for muon tags on the left side are at lower energies than the ones for muon tags on the right side. Furthermore, the spectra for muon tags on the left side are significantly broader. The origin of both observations is a location dependent light collection efficiency. As only one PMT is mounted on each scintillator panel (on the left side for the big scintillators, see Fig. 4.3), large differences in the number of detected photons results. For example, an energy deposition in the corners of the big scintillators leads to a different number of detected photons that an energy deposition in front of the PMT. Note that detailed FLUKA simulation

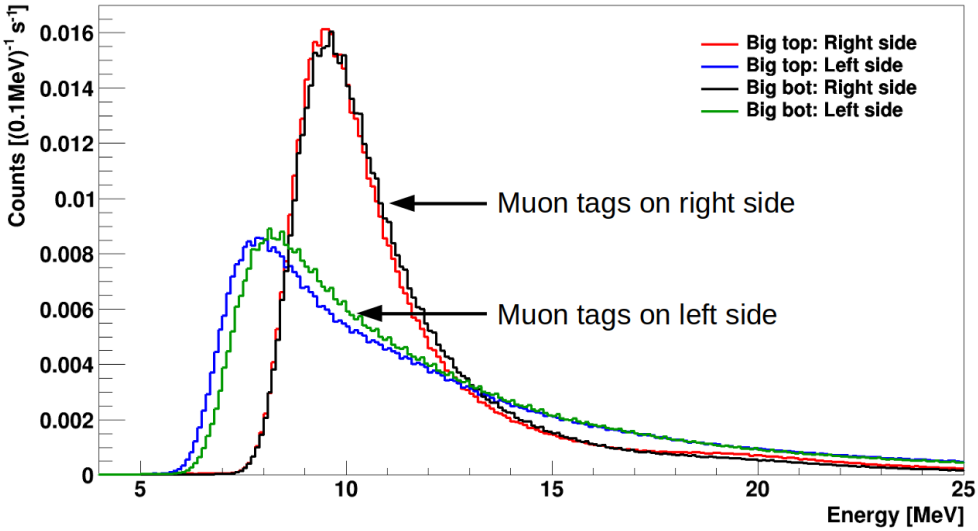

Figure 5.12: Measured energy spectra of the two big scintillators for events with a muon tag on the left and the right side of the setup. The observable deviation arises due to a location dependent scintillation light collection efficiency. Only events of the MINIDEX Run 2 data set are considered. All depicted spectra are normalised to the lifetime of the run.

studies confirmed the origin of the observed deviations between muon tags on the left and the right side of the setup [2]. The measured spectra can be well reproduced by FLUKA simulations in the case of an implemented generation, propagation and detection of the scintillation light within the scintillators.

5.3 Big and Cross Tags

For some investigations (e.g. in Section 5.1.2.4 or Section 6.1.3) two further tags, defined as big tags and cross tags, were used. For a big tag coincident signals in the Big top and Big bot scintillator are required. In the case of a cross tag, coincident signals in both big scintillators as well as two small scintillators on different sides of the setup are requested. As for the muon tags, the big and cross tags require energy depositions $> 5\,\mathrm{MeV}$ that occur within $\pm 30\,\mathrm{ns}$. In Fig. 5.13 the energy spectrum of the Big top scintillator for all events with energies $> 5\,\mathrm{MeV}$ and for those with a muon tag, a big tag or a cross tag are depicted. It is apparent that big, muon and cross tags select different types of events. While events with a big tag are a subset of all events, events with a muon or a cross tag are a subset of events with a big tag. It can be seen that for events with a cross tag more energy is deposited on average in the Big top scintillator than for events

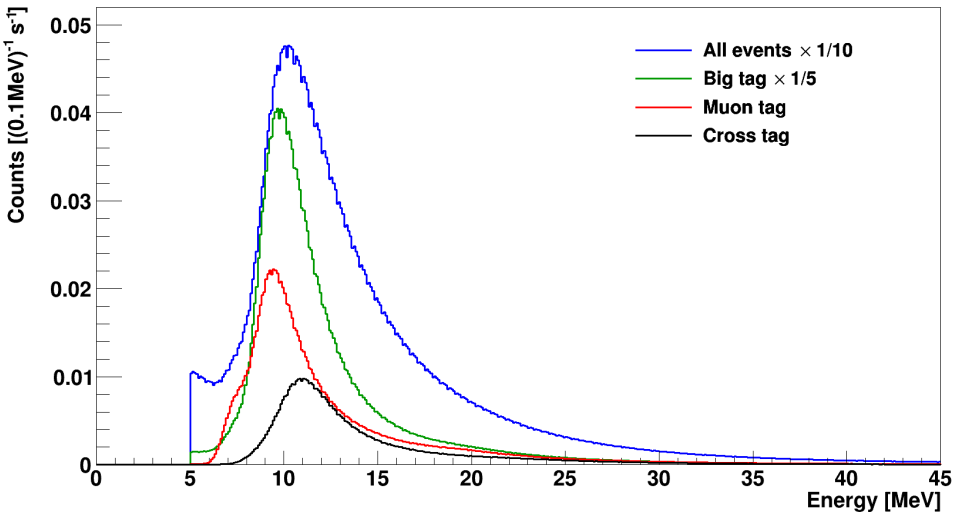

Figure 5.13: Measured energy spectrum of the Big top scintillator for different sets of events. In blue all events with energies $> 5\,\text{MeV}$ are depicted whereas the other colours represent subsets of events, for which a big tag (green), a muon tag (red) or a cross tag (black) was observed. The spectrum for all events is divided by a factor of 10 whereas the spectrum for big tags is divided by a factor of 5. The spectra of muon tags from both sides and the spectra from both cross tag possibilities are respectively added. Only events of the MINIDEX Run 2 data set are considered. All shown spectra are normalised to the lifetime of the run.

with a muon tag. This results from the geometrical selection of muons by the scintillators involved for the corresponding tags. Muons that pass through the setup and lead to a muon tag have in average a smaller angle with the z-axis (see Fig. 4.4) than muons leading to a cross tag. A smaller angle is directly related to a shorter track length (on average) of muons in a scintillator, and therefore to a lower deposited average energy.

Note, the big and cross tags of the MINIDEX setup are not ideal for the study of muon-induced neutrons. In comparison to muon tags, big and cross tags include muons that pass through other parts of the setup than the target walls (e.g. water, aluminium or germanium). As a consequence, the set of 2.2 MeV neutron capture gammas, correlated to big or cross tags, are not as clean as the set of 2.2 MeV gammas related to muon tags.

5.4 Experimental Data Sets

MINIDEX Run 2 started on the 27th January 2016 and lasted until the 11th November 2016, resulting in an experimental data set for lead with a lifetime of 260.35 days. A total number of $2.57 \cdot 10^7$ muon tags has been found in this data set (muon tags on left side: $1.28 \cdot 10^7$, muon tags on right side: $1.29 \cdot 10^7$), leading to a muon tag rate of $1.14\,\mathrm{s}^{-1}$ ($0.57\,\mathrm{s}^{-1}$ for each side individually). The statistical uncertainty on these muon tag rates as well as on the following ones within this section is on the order of $10^{-4}\,\mathrm{s}^{-1}$.

In the middle of November 2016 the lead in the left target wall of the MINIDEX Run 2 setup was exchanged with copper. The MINIDEX Run 3 data taking period started and data was acquired from the 17th November 2016 until the 5th May 2017. An experimental data set for lead and copper with a lifetime of 166.17 days was obtained. In this data set $8.23 \cdot 10^6$ and $8.36 \cdot 10^6$ muon tags have been identified for the lead and the copper side, respectively. These numbers correspond to a muon tag rate of $0.57\,\mathrm{s}^{-1}$ for the lead side and $0.58\,\mathrm{s}^{-1}$ for the copper side. The $\approx 0.01\,\mathrm{s}^{-1}$ higher muon tag rate in the case of copper is significant and results from the lower density of copper in comparison to lead.

Chapter 6

Monte Carlo Simulation Predictions

Simulations were carried out to provide information for the experimental data analysis, like the expected time distribution of the neutron signals and the expected backgrounds. Simulations were also used to determine the number of predicted neutron signals and the simulated value of the external neutron yield.

6.1 Generation, Evaluation and Characterisation of Monte Carlo Data Sets

In the following, the generation of the MINIDEX MC data sets is introduced. This was performed in several simulation steps, starting with primary cosmic rays and ending with the responses of the MINIDEX detectors. The output of each step was used as an input for the corresponding subsequent step. The predicted muon and muon-induced radiation field at the setup position was evaluated by comparing simulated and measured scintillator responses. Afterwards, the generated MC data sets were quantified for their effective lifetimes as well as characterised.

6.1.1 Simulation of Cosmogenic Muons Through the Laboratory Overburden

FLUKA simulations were carried out to provide a set of cosmogenic muons and muon-induced particles at the position of the MINIDEX setup in the Tübingen Shallow Underground Laboratory. Note that all FLUKA simulations discussed within this thesis were carried out separately [2] and that the information provided within this section is partially taken from [94]. The generation of the set of

cosmogenic muons and muon-induced particles proceeds in two steps: In the first step the production of muons by cosmic rays in the upper atmosphere of the Earth and their transport towards the surface was simulated with the FLUKA GCR tools [135]. In these simulations the influence of the Earth's magnetic field and the location of the underground laboratory (48.5 ° N, 9.1 ° E and ≈ 450 metres above sea level) were taken into account. The energy, the type and the momentum of all muons reaching Earth's surface were recorded and subsequently removed from the simulation. On the order of 10^{10} muons were recorded. In Fig. 6.1 the kinetic energy spectrum of the muons on the surface of the Earth with energies > 1 GeV is depicted. The zenith angle distribution of these muons

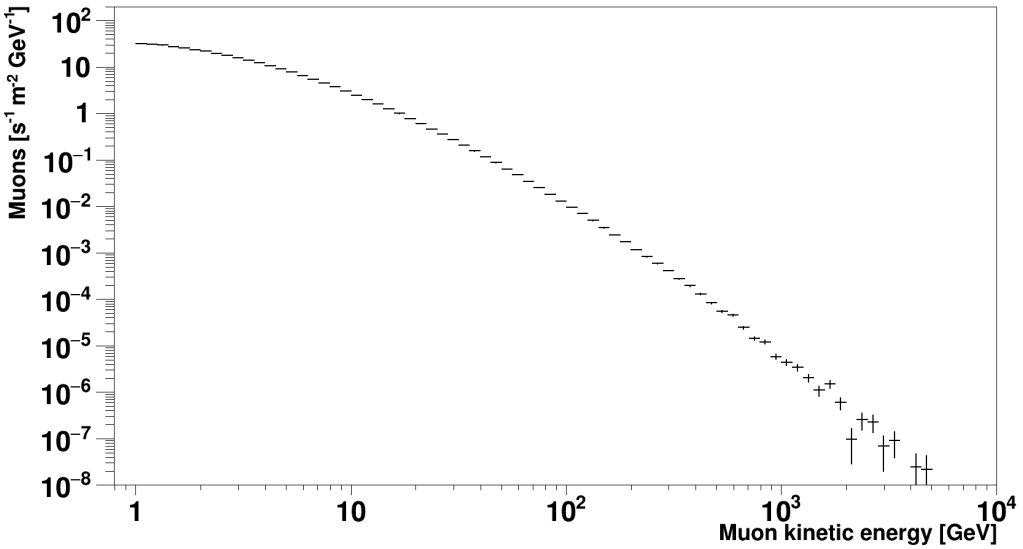

Figure 6.1: Simulated energy spectrum of muons with kinetic energies > 1 GeV reaching the surface of the Earth above the Tübingen Shallow Underground Laboratory. The muons are obtained by FLUKA simulations of the production and the propagation of cosmogenic muons by cosmic rays in the atmosphere of the Earth. The spectrum is normalised with the corresponding effective MC lifetime as determined in Section 6.1.5. The given uncertainties are partially smaller than the size of the marker and are statistical only.

is in good agreement with a $\cos^2$ distribution.

In a second step, on the order of 10^{10} muons with kinetic energies > 1 GeV were started at the surface of the Earth and propagated through the overburden of the underground laboratory. For this purpose, the recorded muons of the previous simulation step were used as an input. Note that in order to reach the experimental setup in the underground laboratory, muons need kinetic energies

$>2\,\mathrm{GeV}$ at the surface of the Earth. For the second simulation step, the Tübingen Shallow Underground Laboratory and its surroundings were implemented in FLUKA. A cross section of the implemented model of the underground laboratory is shown in Fig. 6.2. All particles (muons and muon-induced particles)

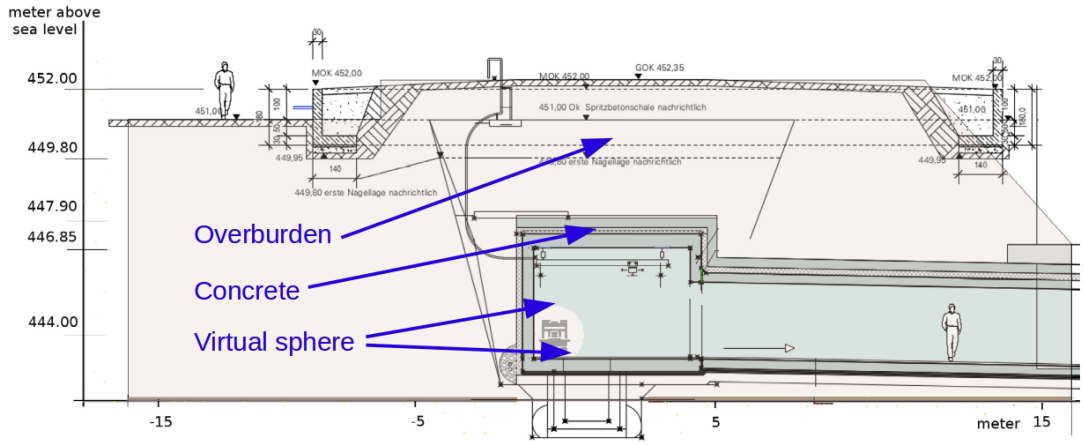

Figure 6.2: Cross section of the implemented model of the Tübingen Shallow Underground Laboratory and its surroundings (shaded areas), together with a superimposed technical design drawing. With the help of this model and the FLUKA MC tool, cosmogenic muons were propagated through the laboratory overburden towards the MINIDEX setup. All particles reaching a virtual sphere of 105 cm radius, indicated in white and enclosing all detectors of the MINIDEX setup, were recorded and subsequently removed from the simulation. Adapted from [94].

reaching a virtual sphere with radius 105 cm, enclosing the complete MINIDEX setup, were recorded and subsequently removed from the simulation. For each individually simulated muon that was started at the surface of the Earth, a set of relevant information for the recorded particles is stored (if at least one particle reaches the virtual sphere). Such a set of information, called pre-recorded muon event in the following, contains the number, the type, the time stamp, the energy, the position and the momentum of all stored individual particles.

On the order of $5 \cdot 10^9$ pre-recorded muon events were obtained, corresponding to an effective MC lifetime of ≈ 135 days (see Section 6.1.5 for details on the determination of the MC lifetimes). These events are provided as input to the MINIDEX Geant4 simulations that were carried out in the context of this thesis.

The density of the soil in the laboratory overburden is $(2.2 \pm 0.2)\,\mathrm{g\,cm^{-3}}$ [94]. The soil as well as further structural material (like concrete) lead to a vertical shielding depth of (13.2 ± 0.8) mwe at the position of the MINIDEX setup in

the underground laboratory. To account for uncertainties the soil density in the overburden of the laboratory was varied by $0.2\,\mathrm{g\,cm^{-3}}$. With the changed soil densities two further data sets with an effective MC lifetime of ≈ 80 days each were generated with FLUKA. These additional data sets were used to quantify the systematic uncertainty that is correlated to the uncertainty on the laboratory overburden density (see Section 8.3.2).

In Fig. 6.3 the kinetic energy spectrum of muons passing through a $0.5\,\mathrm{m^2}$ horizontal plane directly above the MINIDEX setup for a soil density of $2.2\,\mathrm{g\,cm^{-3}}$ is depicted. The muons have a mean muon energy of (9.01 ± 0.01) GeV and the

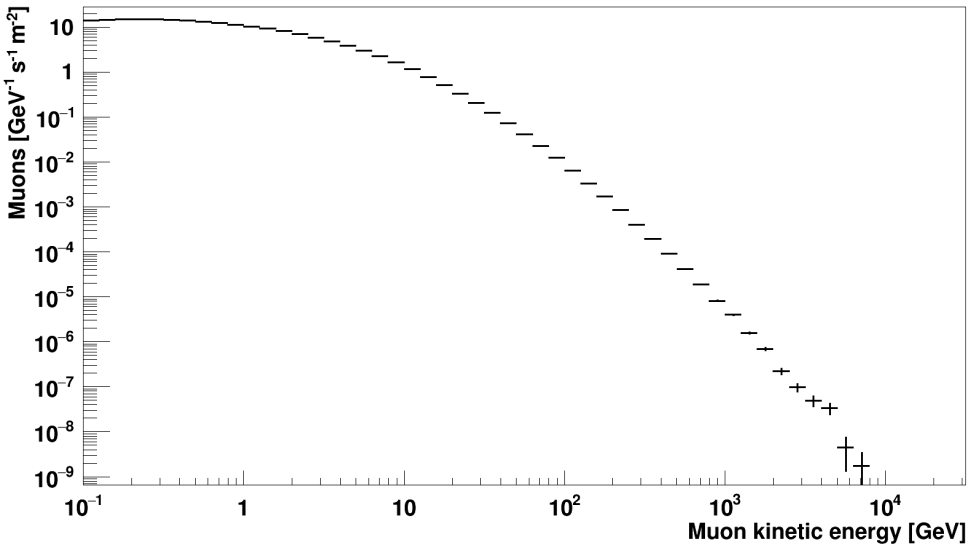

Figure 6.3: Simulated energy spectrum of muons passing through a $0.5\,\mathrm{m^2}$ horizontal plane directly above the MINIDEX setup. The spectrum is normalised with the corresponding effective MC lifetime as determined in Section 6.1.5. The mean energy of the displayed muons is (9.01 ± 0.01) GeV. The given uncertainties are partially smaller than the size of the marker and are statistical only.

predicted muon flux through this plane is $62.58\,\mathrm{m^{-2}\,s^{-1}}$. Taking into account the uncertainty on the density of the soil in the overburden ($\pm\,0.2\,\mathrm{g\,cm^{-3}}$) yields a mean muon energy of (9.0 ± 0.2) GeV.

6.1.2 Generation of MINIDEX Monte Carlo Data Sets

The pre-recorded muon events from the virtual sphere were simulated multiple times with Geant4 (for details on the used Geant4 version see Section 3.1) through both implemented geometry models of the MINIDEX Run 2 and Run 3 setups. On the order of 10^{10} pre-recorded muon events were simulated for both implemented MINIDEX setups. Note, even the same pre-recorded muon events were used as input, each time a different random seed number was given to the particle generator of Geant4. The generated MC data sets contain the individual energy depositions and their corresponding time stamps for the eight implemented MINIDEX detectors. Also the energy, the momentum and the creation location of neutrons, produced within the setup, were stored.

6.1.3 Quality Evaluation of Pre-Recorded Muon Events

The quality of the FLUKA generated pre-recorded muon events was evaluated. This was carried out with the help of coincidences between different predefined sets of scintillators. For this purpose, the measured and the Geant4 simulated rates as well as the corresponding spectra of these coincidences were compared. The simulated rates were normalised with the help of the effective MC lifetimes (see Section 6.1.5). Only coincidences of scintillators were used for the evaluation of quality of the pre-recorded muon events, because the rate of events in a single experimental scintillator contains lots of energy depositions from background sources (e.g. from natural radioactivity). Energy depositions $> 5\,\mathrm{MeV}$ within a narrow $\pm 30\,\mathrm{ns}$ time window are requested for the chosen coincidences. Note that these are the same conditions as the ones used for the determination of the different tags in the experimental data sets (see Section 5.2 and Section 5.3). The chosen scintillator coincidences for the evaluation of the FLUKA generated pre-recorded muon events are muon and cross tags as well as coincidences between the Small2 and the Big top scintillator. The chosen scintillator coincidences are sensitive to different muon angles and energies (see Section 5.3).

In Fig. 6.4 the measured and the simulated energy spectrum of the Big top scintillator for muon tags on the right side are shown. Muon tags on the right side of the setup were selected for the comparison, as the measured energy of the Big top scintillator is well reproduced by the simulation (see Section 5.2). The spectra are normalised to the (effective) lifetime of the MINIDEX Run 2 (MC) data set. A difference of $\approx 6\,\%$ between the measured and the simulated rate was observed, while the main features of the distributions are similar. In Fig. 6.5 the measured and the simulated energy spectrum of the Big top scintillator are de-

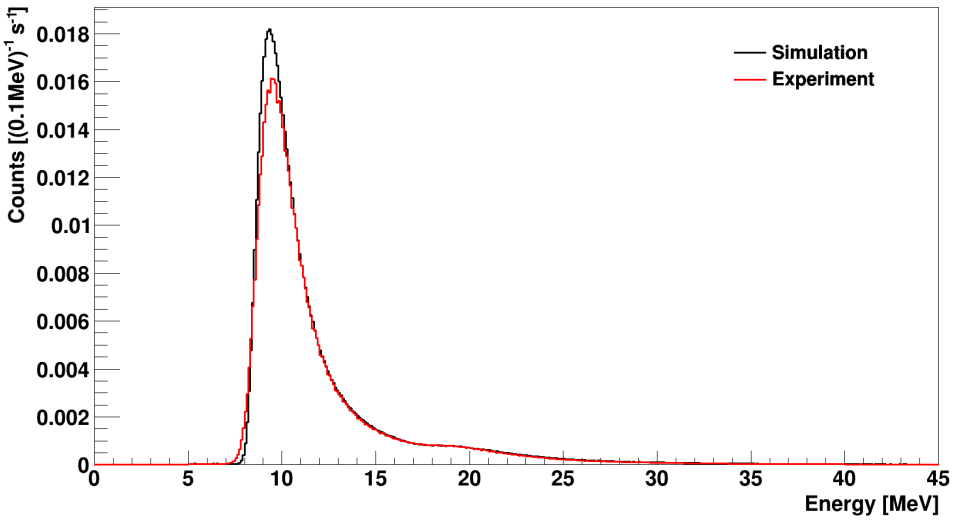

Figure 6.4: Simulated (black) and measured (red) energy spectrum of the Big top scintillator. Only events of the experimental and MC data sets of MINIDEX Run 2, for which a muon tag on the right side was found, are considered. Both spectra are normalised to the (effective) lifetime of the corresponding data set.

picted for cross tags. Only cross tags with the Small2 and the Small3 scintillator are taken into account, because for these coincidences the muon passes through the Big top scintillator on the right side. Good agreement between the measured and the simulated spectrum is apparent, with a difference in the rate of only 1 %. The third investigated coincidence (Big top and Small2, for details on this coincidence see Section 6.1.5) yields further good agreement between measured and simulated coincidences. Furthermore, comparisons between measured and simulated scintillator coincidences in the experimental and the MC data set of MINIDEX Run 3 are in good agreement with these observations.

As a consequence of the general good agreement between measured and simulated scintillator coincidences it can be concluded that the FLUKA generated pre-recorded muon events describe the muon and muon-induced radiation field at the setup position in the Tübingen underground laboratory well. The Geant4 generated MINIDEX Run 2 and Run 3 MC data sets, obtained by using the FLUKA provided pre-recorded muon events as an input, can therefore be reliably used to study muon-induced neutrons.

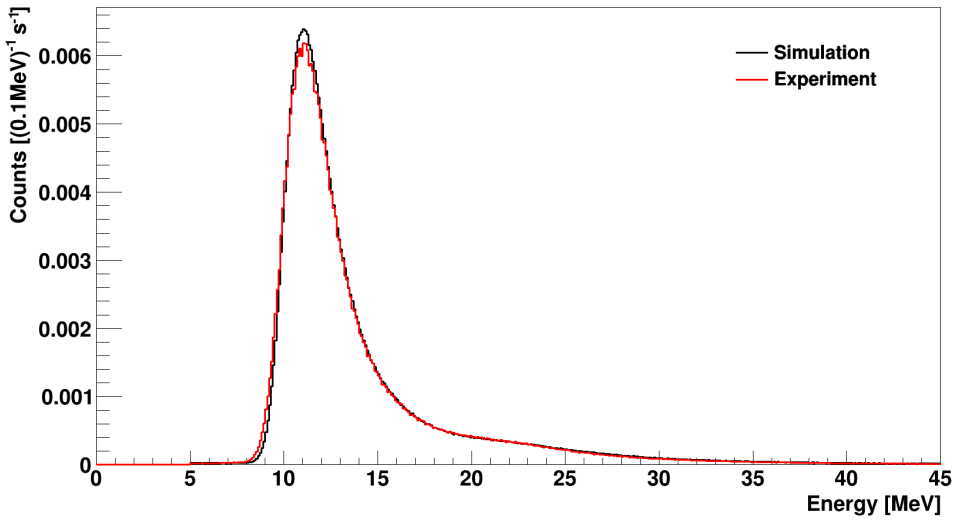

Figure 6.5: Simulated (black) and measured (red) energy spectrum of the Big top scintillator for cross tags. Only events of MINIDEX Run 2, for which a cross tag with the Small2 and the Small3 scintillator was found, are considered. Both spectra are normalised to the (effective) lifetime of the corresponding data set.

6.1.4 Energy Distribution of Tagged Muons

The energy distribution of muons leading to a muon tag in the MINIDEX Run 2 and Run 3 MC data sets was investigated. In Fig. 6.6 the simulated energy spectrum of tagged muons from the MINIDEX Run 2 MC data set, at the position before they enter the lead target walls, is shown. A mean muon energy of (8.73 ± 0.01) GeV was determined for these muons. In order to pass completely through one of the lead target walls and generate a muon tag, a muon needs a kinetic energy of at least ≈ 1 GeV. The events visible in the spectrum at a few hundred MeV result from events, for which muon-induced particles contributed to the energy depositions in at least two scintillators (see Fig. 4.1 for the location of the scintillators within the setup) of the corresponding muon tag. When taking into account the uncertainty on the soil density of the laboratory overburden (see Section 6.1.1), a mean muon energy of (8.7 ± 0.2) GeV and a most probable energy of (1.05 ± 0.05) GeV results for the tagged muons of Run 2. As expected, for the tagged muons on the lead side of MINIDEX Run 3 the same values were found. Owing to the lower density of copper compared to lead, a mean muon energy of (8.5 ± 0.2) GeV and a most probable energy of (0.87 ± 0.05) GeV were determined for the tagged muons of the MINIDEX Run 3 copper side.

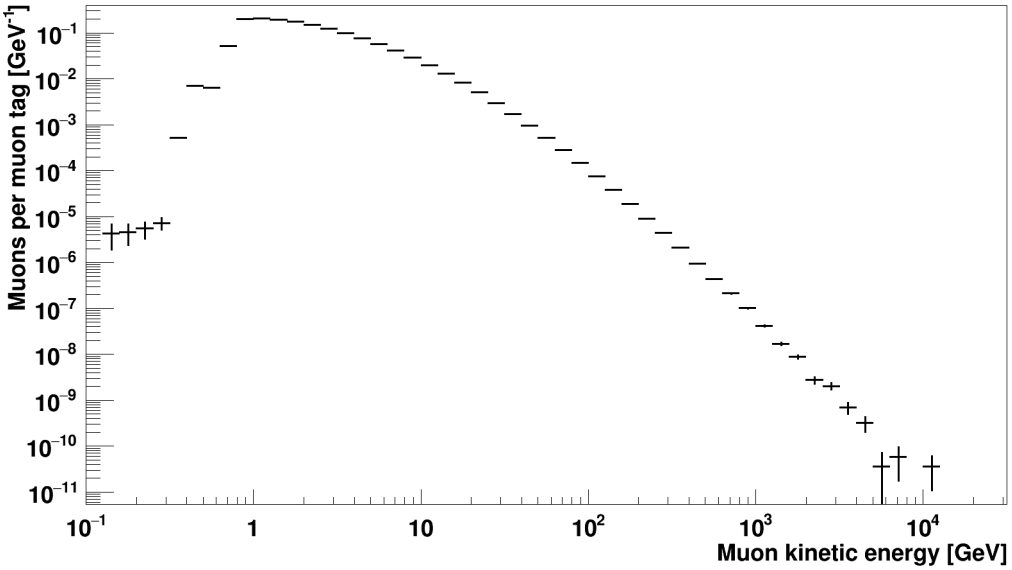

Figure 6.6: Simulated energy spectrum of tagged muons, recorded at the position before entering the MINIDEX Run 2 lead target walls. The spectrum is normalised to the corresponding number of muon tags. The muons have a mean muon energy of $(8.73 \pm 0.01)\,\mathrm{GeV}$. The given uncertainties are partially smaller than the size of the marker and are statistical only.

6.1.5 Monte Carlo Lifetimes and Monte Carlo Data Sets

The generated MC data sets for MINIDEX Run 2 and Run 3 were quantified for their effective lifetimes. For this purpose, coincidences between the Big top and the Small2 scintillator (called normalisation coincidences) were used. The measured and simulated scintillator spectra of the normalisation coincidences for MINIDEX Run 2 are depicted in Fig. 6.7. Energy depositions $> 5\,\mathrm{MeV}$ within $\pm\,30\,\mathrm{ns}$ are requested in both scintillators. The MC spectra were normalised with the help of $\mathrm{R}_{\mathrm{Norm}}^{\mathrm{Exp}}$, the measured rate of the normalisation coincidences. Good agreement between the simulated and the measured spectra can be observed. A value of $(8.39 \pm 0.02)\,\mathrm{s}^{-1}$ was determined for both experimental runs for the rate $\mathrm{R}_{\mathrm{Norm}}^{\mathrm{Exp}}$. The stated uncertainty is dominated by an observed systematic difference on $\mathrm{R}_{\mathrm{Norm}}^{\mathrm{Exp}}$, found for the two individual experimental runs. Both involved scintillators are located above the target, hence the same rate of normalisation coincidences would be expected for both experimental runs for a constant muon flux. The experimentally observed difference might therefore result from a slightly different positioning of the involved scintillators in the two experimental runs. In Section 5.1.2.4 it was shown that the air pressure leads to a variation of the Big

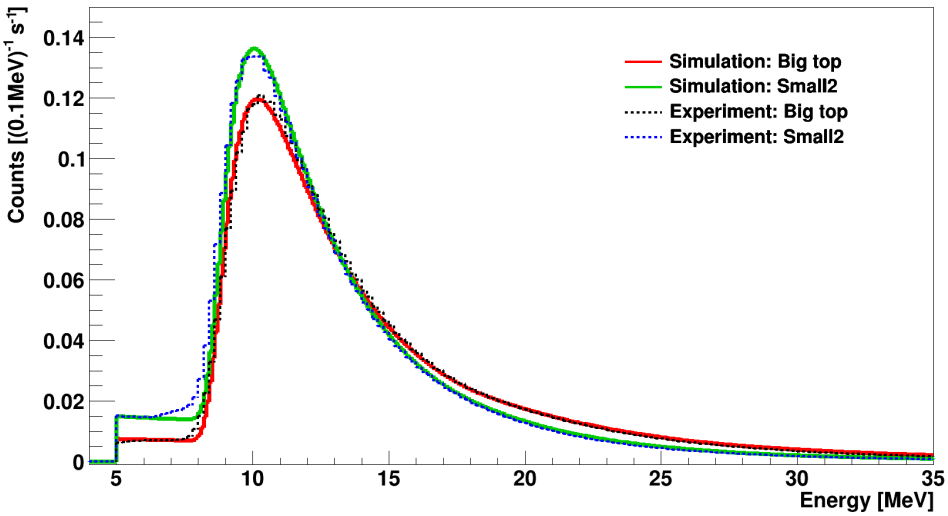

Figure 6.7: Measured and simulated energy spectrum of the Big top and the Small2 scintillator. Only events of the experimental and MC data set of MINIDEX Run 2, for which a coincidence between the two scintillators was found, are considered. The measured spectra are normalised to the lifetime of the experimental run whereas the simulated spectra are normalised to the measured rate of these coincidences.

tag rate on the percentage level. Consequently, also a different mean air pressure could yield the observed difference in the rate of normalisation coincidences. Coincidences between the Big top and the Small2 scintillator were used for the determination of the effective MC lifetimes, as the rate of events in a single scintillator panel (i.e. without the request for a coincidence) contains a large number of energy depositions from background sources (e.g. radioactivity). In order to be (mostly) independent from the interactions of muons and muon-induced particles in the target, a scintillator coincidence above the target was chosen. Furthermore, the measured energy of the Big top scintillator for coincidences on the right side of the setup is well reproduced by the simulation (see Section 5.2).

Using the measured rate $R_{\mathrm{Norm}}^{\mathrm{Exp}}$, an effective MC lifetime of (202.9 ± 0.5) days was determined for the MINIDEX Run 2 MC data set. This data set contains $2.12 \cdot 10^7$ lead muon tags. For the generated MINIDEX Run 3 MC data set an effective MC lifetime of (328.6 ± 0.8) days was obtained. In the Run 3 MC data set $1.69 \cdot 10^7$ lead muon tags and $1.74 \cdot 10^7$ copper muon tags were identified. The determined MC lifetimes show that the generated MC data sets have a similar statistic as the acquired experimental data sets (see Section 5.4). Note that the stated effective MC lifetimes do neither affect nor enter the following analysis.

6.2 Determination of Neutron Signals

The strategy to determine the simulated neutron signals, their time distribution and the expected backgrounds of the generated MINIDEX Run 2 and Run 3 MC data sets is presented. These information are used in the experimental data analysis to determine the neutron signals.

The predicted distribution of the time differences between neutron signals, observed as a 2.2 MeV neutron capture gammas in the germanium detectors, and the corresponding muon tags was determined. The obtained time distribution for the detected neutron signals of the Run 2 MC data set is shown in Fig. 6.8. It can be seen that the neutron signals are predicted within the first few ms after

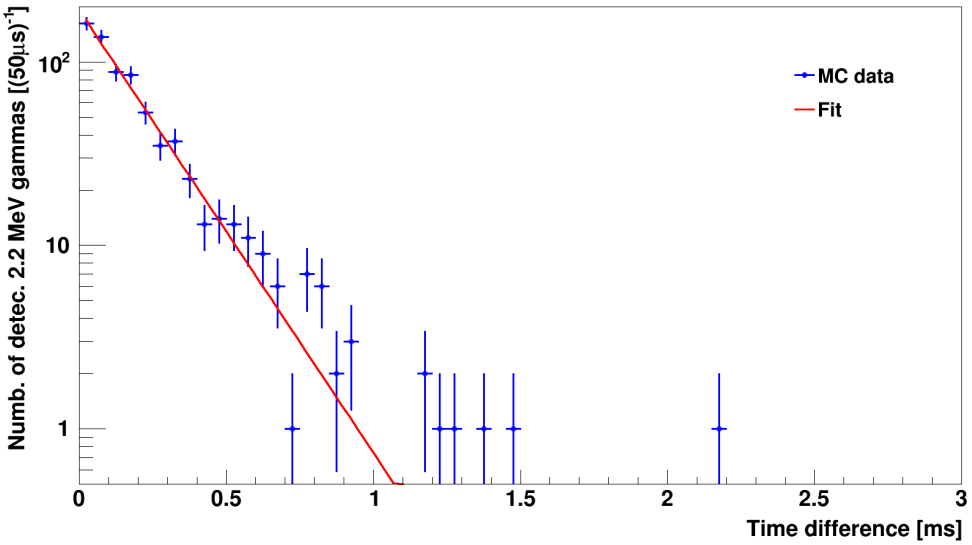

Figure 6.8: Distribution of simulated time differences between detected neutron signals and the corresponding muon tags. Here only neutron signals of the MINIDEX Run 2 MC data set are considered. A falling exponential fit function (red), applied on the distribution, yields a mean delay of the neutron signals of $(180 \pm 8)\,\mu$s. All displayed uncertainties are statistical only.

the muon tags. According to the simulation $(98.7 \pm 1.0)\,\%$ of the neutron signals occur within 1 ms after the muon tags[1]. With a falling exponential fit function,

[1]This percentage and the following two percentages within this section were determined by analysing a special MC data set. This special MC data set contains a significantly lager number of neutron signals, owing to the multiple simulation of the same neutrons. For detailed information on this data set see Section 9.3.

applied on the simulated distribution, a mean delay of $(180 \pm 8)\,\mu$s was found for the neutron signals.

Note, for any analysis of the MC data within this thesis, an artificial dead time of $20.3\,\mu$s (see Section 4.3.3) was implemented for the germanium detectors.

The neutron signals shown in Fig. 6.8 were identified in the MC data set by searching for events in the germanium detectors at an energy of 2224.37 keV[2]. In the simulation a simple identification of neutron signals based on the detected energy in the germanium detectors is possible, as no energy resolution was considered for the detectors. As the germanium detectors in the experiment have a finite energy resolution, the predicted energy depositions within a ± 3 keV energy window around 2224.37 keV were studied. This energy window roughly corresponds to the measured $\pm 3\,\sigma$ energy resolution of the used germanium detectors at 2.2 MeV (see Section 5.1.3.1). The spectrum of simulated energy depositions in the germanium detectors (both germanium detectors added up) in a small energy range around the position of the 2.2 MeV neutron capture gammas is shown in Fig. 6.9. A number of energy depositions from background sources within the energy region corresponding to the $\pm 3\,\sigma$ energy resolution (indicated by the two black vertical lines) can be observed. These predominantly result from muon-induced electrons and gammas. However, they occur mainly within the first few μs after the muon tags. By rejecting all energy depositions within the first $7\,\mu$s after each muon tag, the background in the relevant energy region is reduced by a factor of $30\,^{+21}_{-13}$. The rejection of all energy depositions within the first $7\,\mu$s after each muon tag reduces the maximum percentage of all detectable neutron signals to $(96.2 \pm 0.9)\,\%$.

The number of simulated neutron signals per muon tag is called neutron signal rate R_S^{Sim} in the following. Note, for R_S^{Sim} only neutron signals that are observed later than $7\,\mu$s after the corresponding muon tag are considered. If a time window from $7\,\mu$s to 1 ms after a muon tag would be selected, the simulation predicts that $(94.9 \pm 1.3)\,\%$ of all neutron signals could be observed.

In Fig. 6.10 the muon kinetic energy spectrum for all events with a muon tag and for those with an additional neutron signal is depicted. It can be seen that the muon energy spectrum for events with a neutron signal is significantly higher than the spectrum for all events with a muon tag (mean muon energy increased by a factor of 7.24 ± 0.04). This is consistent with the expected correlation between

[2]The Geant4 predicted energy of the 2.2 MeV neutron capture gammas (2224.37 keV) differs from the literature value of 2223.26 keV by ≈ 1 keV [122]. However, this bug has no influence on the simulation predictions and has been reported to the Geant4 collaboration [136].

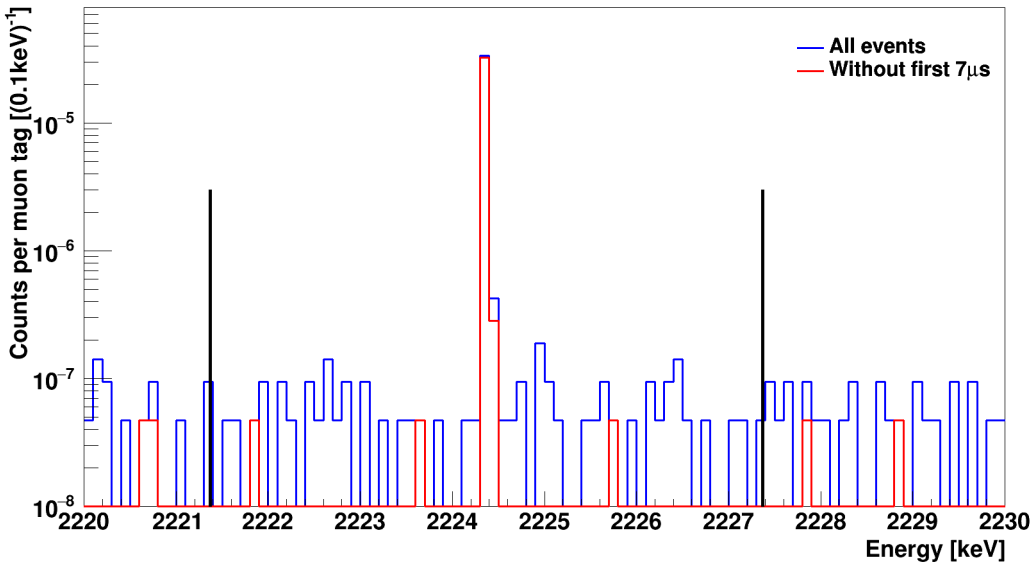

Figure 6.9: Spectrum of simulated energy depositions in the germanium detectors in a small energy range around the 2.2 MeV neutron capture gammas for events with a muon tag. The individual spectra of the two germanium detectors were added up. Only events of the MINIDEX Run 2 MC data set are considered. In blue all energy depositions in the germanium detectors are depicted, while in red only those energy depositions that are observed later than 7 μs after a muon tag are drawn. The black vertical lines indicate an energy region of ± 3 keV, the experimentally determined $\pm 3\,\sigma$ energy resolution of the employed germanium detectors at 2.2 MeV.

the neutron yield and the mean muon energy (see Section 3.2.2). An increased mean muon energy leads to a higher neutron production probability in the target and therefore to a higher 2.2 MeV neutron capture gamma detection probability.

6.3 Neutron Signal Multiplicity Events

Simulated events with a muon tag, for which more than one 2.2 MeV neutron capture gamma was found, were studied and the background of muon-induced showers from the laboratory overburden to these events was estimated. It is shown that these events can be used to investigate the precision of a specific simulation quantity, the number of neutrons directly produced by muons in muon-nuclear reactions in the lead target walls of MINIDEX.

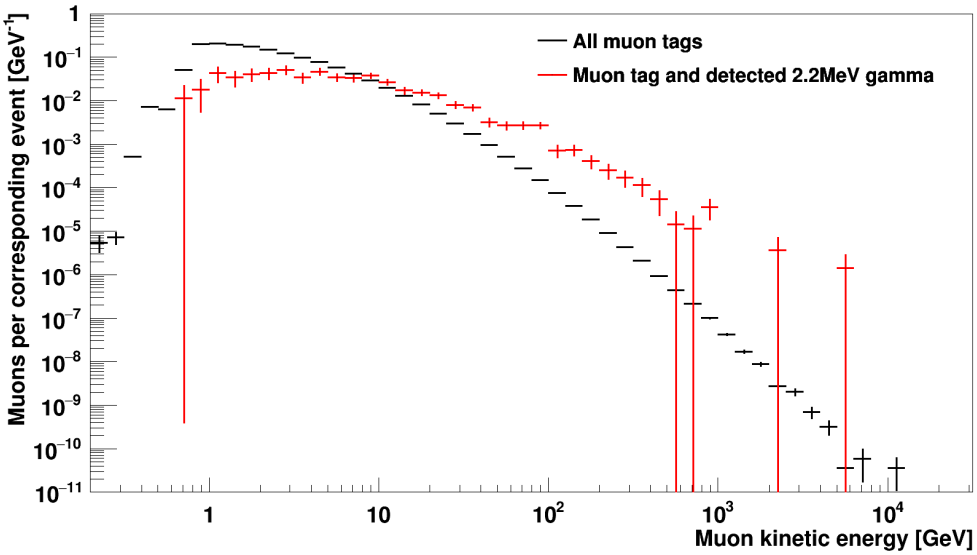

Figure 6.10: Simulated muon kinetic energy spectrum for all events with a muon tag (black) and for the subset of events with an additional neutron signal (red). Only events of the MINIDEX Run 2 MC data set are considered. The depicted spectra represent the energies of the muons at the position before they enter the lead target walls. The black spectrum is normalised to the number of muons tags whereas the red spectrum is normalised to the number of events with a muon tag and an additional neutron signal. The mean kinetic energy of the muons in the black and red spectrum is (8.73 ± 0.01) GeV and (63.18 ± 0.34) GeV, respectively. The given uncertainties are partially smaller than the size of the marker and are statistical only.

6.3.1 Determination of Neutron Signal Multiplicity Events

Events with a muon tag and more than one 2.2 MeV neutron capture gamma were determined in MINIDEX Run 2 MC data set. These events are called neutron signal multiplicity events in the following. The neutron signal multiplicity events are identified in the MC data set by searching for two individual 2224.37 keV energy depositions in the germanium detectors for the same muon tag. Only 2.2 MeV gammas, occurring later than 7 μs after the muon tags, are considered. The corresponding multiple 2.2 MeV gammas can be detected either both in the same germanium detector or each in a different one. The background, resulting from muon-induced showers that are produced in the laboratory overburden, is discussed in Section 6.3.3 and was found to be negligible.

For the study of neutron signal multiplicity events only the MINIDEX Run 2 MC data set was used, as it contains a cleaner set of events than the Run 3 MC data set (lead only was used as a target in Run 2). Furthermore, the experimental

Run 2 data set (see Section 5.4), which is the data set the simulation results will be compared to, has a significantly higher statistic than the experimental Run 3 data set. The simulated neutron signal multiplicity events are evaluated as the rate R_M^{Sim}, the number of neutron signal multiplicity events per muon tag. According to the simulation, the 2.2 MeV neutron capture gammas of all identified neutron signal multiplicity events contribute by $(5.8 \pm 0.8)\,\%$ to the total number of detected neutron signals.

6.3.2 Muon-Nuclear Neutron Multiplicity

The number of neutrons directly produced by muons in muon-nuclear reactions within the target walls of the MINIDEX Run 2 setup, $M_N^{Mu.\text{-}nuc.}$, is called muon-nuclear neutron multiplicity in the following. The correlation between the mean muon-nuclear neutron multiplicity, $\overline{M}_N^{Mu.\text{-}nuc.}$, and the neutron signal multiplicity events was investigated. Note that no event with more than one muon-nuclear reaction was observed for any event of the Run 2 MC data set. In Fig. 6.11 the $M_N^{Mu.\text{-}nuc.}$ distribution is displayed for different sets of events. In green $M_N^{Mu.\text{-}nuc.}$ for all muon-nuclear reactions is shown. The other colours display $M_N^{Mu.\text{-}nuc.}$ for different subsets of the green distribution, depending on the number of detected 2.2 MeV gammas. A correlation between the number of detected 2.2 MeV gammas and $\overline{M}_N^{Mu.\text{-}nuc.}$ can be seen. In Table 6.1 the corresponding values of $\overline{M}_N^{Mu.\text{-}nuc.}$ for the depicted distributions are given, which confirm this observation. It was

Table 6.1: Simulated mean muon-nuclear neutron multiplicity $\overline{M}_N^{Mu.\text{-}nuc.}$ for muon-nuclear reactions within the target walls of the MINIDEX Run 2 setup. Only events with a muon tag are considered. $\overline{M}_N^{Mu.\text{-}nuc.}$ for all muon-nuclear reactions as well as for different subsets, depending on the number of detected 2.2 MeV gammas, are given. Note that only one event with three detected 2.2 MeV gammas was found. The spectra corresponding to the stated $\overline{M}_N^{Mu.\text{-}nuc.}$ are shown in Fig. 6.11. All given uncertainties are statistical only.

Number of detected 2.2 MeV gammas	$\overline{M}_N^{Mu.\text{-}nuc.}$
≥ 0	12.73 ± 0.05
≥ 1	20.8 ± 0.7
≥ 2	31.1 ± 2.5
3	34

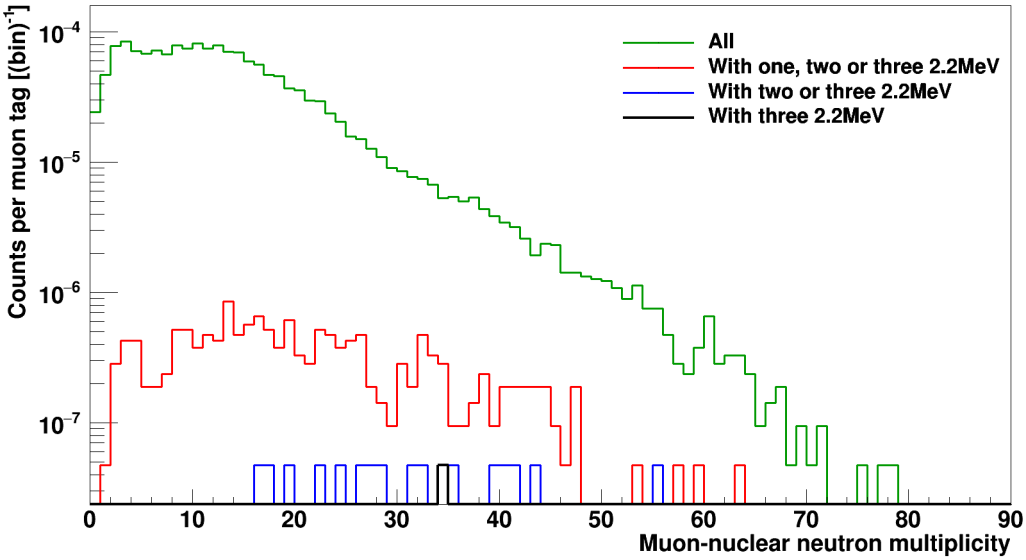

Figure 6.11: Simulated number of neutrons, produced directly by muons in muon-nuclear reactions $M_N^{\text{Mu.-nuc.}}$ (muon-nuclear neutron multiplicity). Only events with a muon tag for which a muon-nuclear reaction occurred within the target walls of the MINIDEX Run 2 setup are taken into account. In green $M_N^{\text{Mu.-nuc.}}$ for all muon-nuclear reactions is shown, while the other colours represent subsets with a different number of detected 2.2 MeV neutron capture gammas. All shown spectra are normalised to the total number of muon tags of the Run 2 MC data set. Note, the black spectrum contains only one event, which has a $M_N^{\text{Mu.-nuc.}}$ of 34.

determined that $(47.8 \pm 2.6)\,\%$ of all detected 2.2 MeV gammas of the Run 2 MC data set result from events with a muon tag for which a muon-nuclear reaction occurred within the target walls. For neutron signal multiplicity events the corresponding percentage was determined to be $(65 \pm 16)\,\%$. Note that this does not necessarily mean that the detected 2.2 MeV gammas solely result from particles produced in muon-nuclear reactions within the target walls. Any muon interaction outside the target walls as well as any muon interaction within the target walls, which is not a muon-nuclear reaction, can lead to a detected 2.2 MeV neutron capture gamma in the germanium detectors. However, it was found that $> 80\,\%$ of all observed 2.2 MeV gammas, detected for events with a muon tag and a muon-nuclear reaction within the target walls, result from the particles released in the muon-nuclear reactions. As a consequence, this shows that the number of neutron signal multiplicity events is directly correlated to $\overline{M}_N^{\text{Mu.-nuc.}}$.

6.3.3 Background of Muon-Induced Showers from Laboratory Overburden

The contribution of shower particles, induced by muons during their passage through the laboratory overburden, to the neutron signal multiplicity events of MINIDEX Run 2 was investigated. This is crucial in order to exclude the possibility that the correlation discussed beforehand is due to backgrounds. For this purpose, the average numbers of overburden shower particles, recorded on the virtual sphere (see Section 6.1.1) for events with a muon tag and at least one detected 2.2 MeV neutron capture gamma, were determined. In the following, only neutrons, pions and gammas are considered, as the simulation predicts that these dominate the overburden shower-induced neutron production within the MINIDEX setup. The average numbers of the considered particles on the virtual sphere per neutron signal or neutron signal multiplicity event are given in Table 6.2. While for neutrons and pions all kinetic energies are considered,

Table 6.2: Simulated average numbers of different shower particles on the virtual sphere for events of the MINIDEX Run 2 MC data set with a muon tag and an observed neutron signal or neutron signal multiplicity event. All given values are expressed in number of shower particles per neutron signal or neutron signal multiplicity event. Gammas with energies >8 MeV only are taken into account. All given uncertainties are statistical only.

	Particles per	
	neutron signal	neutron signal multiplicity event
Neutrons	1.29 ± 0.07	1.20 ± 0.32
Pions	1.22 ± 0.06	1.08 ± 0.30
Gammas	21.9 ± 0.9	7.5 ± 1.6

only gammas with energies >8 MeV (for the choice of this energy cut see Section 9.1) were taken into account. The determined average numbers of the shower particles for the neutron signal multiplicity events either agree within statistical uncertainties with the ones for the neutron signals or are lower. In Fig. 6.12 the energy spectra of the shower particles for the two investigated sets of events are depicted. The spectra for neutron signals and neutron signal multiplicity events are represented by the open and the filled markers, respectively. Only energies <4 GeV are depicted, owing to the extremely low statistic of particles with higher energies in the case of the neutron signal multiplicity events. It can be seen that

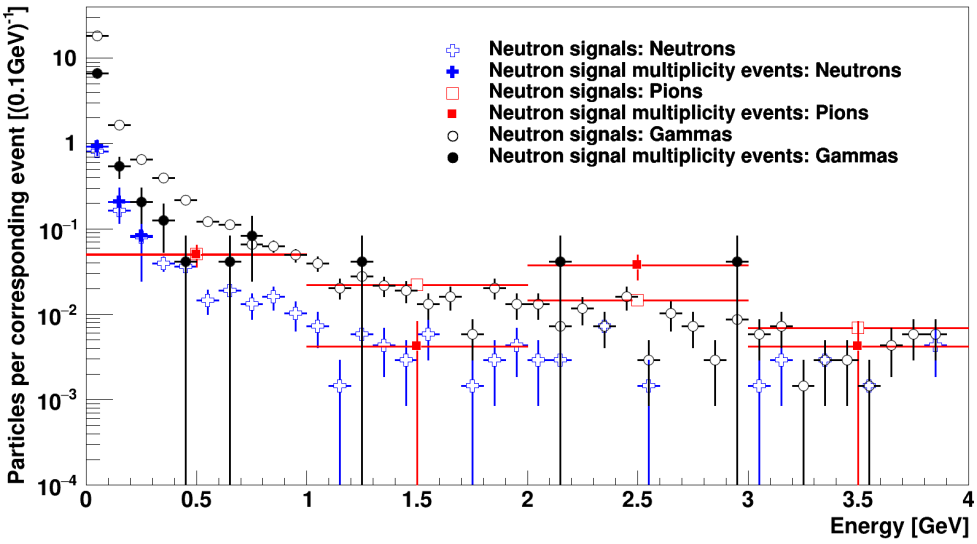

Figure 6.12: Simulated energy spectra of neutrons (blue), pions (red) and gammas (black), recorded on the virtual sphere, for events with a muon tag and an additional neutron signal (open markers) or neutron signal multiplicity event (filled markers). Gammas with energies $>8\,\mathrm{MeV}$ only are taken into account. The given uncertainties are partially smaller than the size of the marker and are statistical only.

the shape of the spectra, corresponding to the same particle type, are similar for all cases. Concluding, the studied average numbers and the discussed energy spectra hint towards a similar contribution of shower particles, produced in the laboratory overburden, to the neutron signals and the neutron signal multiplicity events. As only a minor part of the neutron signals results from overburden shower particles (see Section 9.3), also a minor contribution of the overburden shower particles to the neutron signal multiplicity events is expected.

6.3.4 Conclusion of Neutron Signal Multiplicity Event Study

A correlation between the number of neutron signal multiplicity events and $\overline{\mathrm{M}}_{\mathrm{N}}^{\mathrm{Mu.\text{-}nuc.}}$ was found. Consequently, by comparing the simulated rate of neutron signal multiplicity events $\mathrm{R}_{\mathrm{M}}^{\mathrm{Sim}}$ to the corresponding measured rate of these events, the reliability of the simulation for the prediction of the muon-nuclear neutron multiplicity can (to some extent) be evaluated.

6.4 External Neutron Yield

In order to determine the external neutron yield (Y_{Ext}) by using Eq. (3.2), the external neutron yield predicted by simulation (Y_{Ext}^{Sim}) has to be determined. For this purpose, the implemented MINIDEX Run 2 and Run 3 setups were first simulated with a small number of pre-recorded muon events, leading to $\approx 10^5$ muon tags. Only events with a muon tag are considered in the following. These first simulations showed that the number and the energy of neutrons emitted from both lead sides of the MINIDEX Run 2 setup agree within statistical uncertainties with the number and the energy of neutrons emitted from the lead side of the MINIDEX Run 3 setup. Hence, in order to determine Y_{Ext}^{Sim} (for lead and copper) only the Run 3 setup was simulated with a higher number of pre-recorded muon events.

Note that the determined values of Y_{Ext}^{Sim} are not "background free", as for example neutrons induced by particle showers from the laboratory overburden also contribute. This is important, as the scaling described by Eq. (3.2) can not be applied for a "background free" Y_{Ext}^{Sim}. This results from the fact that the measured neutron signal rate, which is used to determine the mismatch factor MF_S, is not free of backgrounds. Note that the applied scaling assumes that all processes involved lead to the same mismatch factor.

In Fig. 6.13 the implemented MINIDEX Run 3 setup, used to determine Y_{Ext}^{Sim} for lead and copper, is depicted. Two tag generating muons, inducing neutrons during their passage through the target walls, are schematically displayed. For all neutrons leaving the selected surfaces of the copper and lead target walls, which are indicated in Fig. 6.13, the energy and the momentum direction were recorded and the neutrons were subsequently removed from the simulation. With the applied procedure of removing the neutrons, the issue of correctly counting neutrons that pass through surfaces multiple times can be avoided[3]. At the position before the simulated muons enter the target walls, they have a mean muon energy of $(8.72 \pm 0.01)\,\mathrm{GeV}$ and $(8.52 \pm 0.01)\,\mathrm{GeV}$ for lead and copper, respectively. As the same pre-recorded muon events were used as input, these are the same mean energies as the tag generating muons in the standard simulation (see Section 6.1.4) have.

[3] In simulation studies like [137] it was shown that scattering leads to neutrons crossing the same surface multiple times. The influence of this effect depends on the material and the neutron energy.

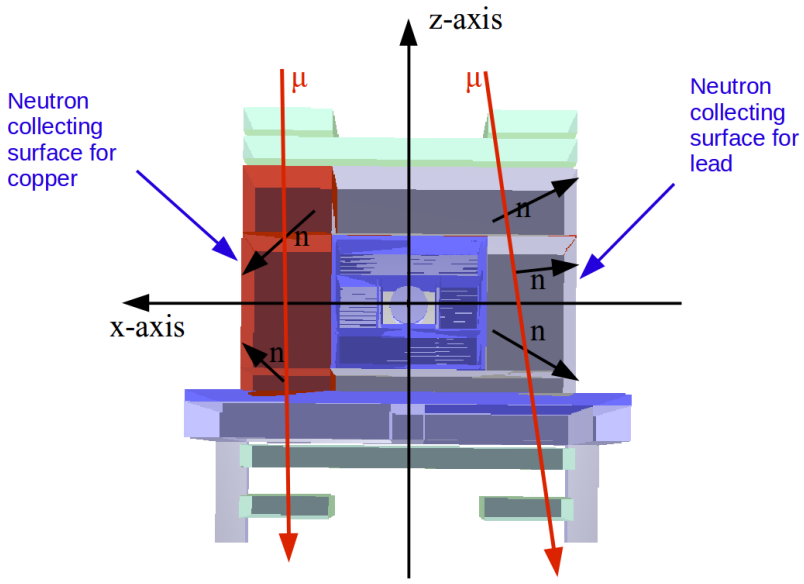

Figure 6.13: Cross section of the implemented MINIDEX Run 3 setup that is used to determine Y_{Ext}^{Sim}, the external neutron yield predicted by simulation, for lead and copper. The indicated outer surfaces of the setup, which are perpendicular to the x-axis, were selected for the determination of Y_{Ext}^{Sim}.

The simulated kinetic energy spectra of the neutrons emitted from the selected surfaces are depicted in Fig. 6.14(a). It can be seen that the simulation predicts the same rate of emitted neutrons (i.e. emitted neutrons per muon tag) from the lead and copper surface for neutron energies above $\approx 60\,\mathrm{MeV}$. For lower neutron energies the rate of emitted neutrons from the lead surface is clearly enhanced. A mean energy of $(4.9 \pm 0.2)\,\mathrm{MeV}$ and $(8.9 \pm 0.3)\,\mathrm{MeV}$ was determined for the neutrons emitted from the lead and copper surface, respectively. In Fig. 6.14(b) the distribution of the angle between the momentum direction of the emitted neutrons and the z-axis is depicted. It is apparent that for both investigated target materials the same angular distribution is predicted by the simulation.

In Table 6.3 the determined individual parameters for Eq. (3.1) as well as the resulting values of Y_{Ext}^{Sim} are given. A small difference in the average track length of the muons through the lead and the copper target walls was found. This difference results from the different target densities in combination with a dependence of the muon energy on the angle between the momentum direction of the muons and the z-axis. The more inclined muons are (on average), the higher their energy is (on average). The obtained rate of emitted neutrons from

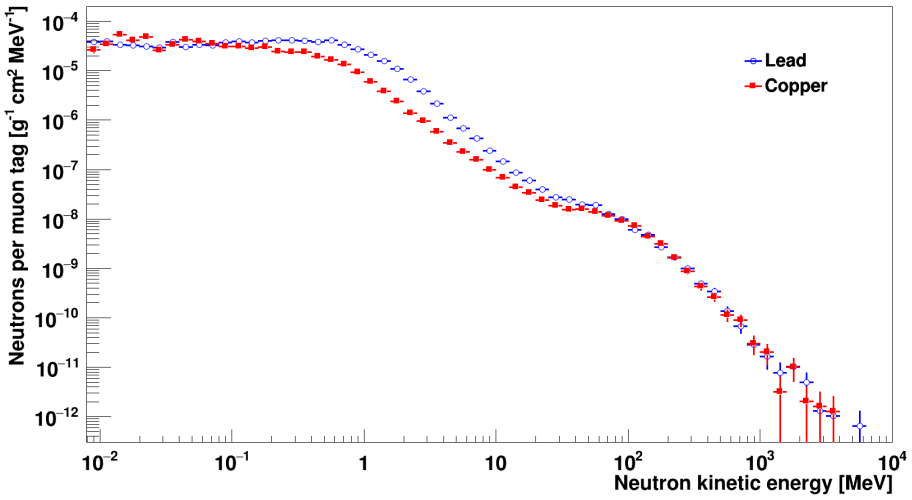

(a)

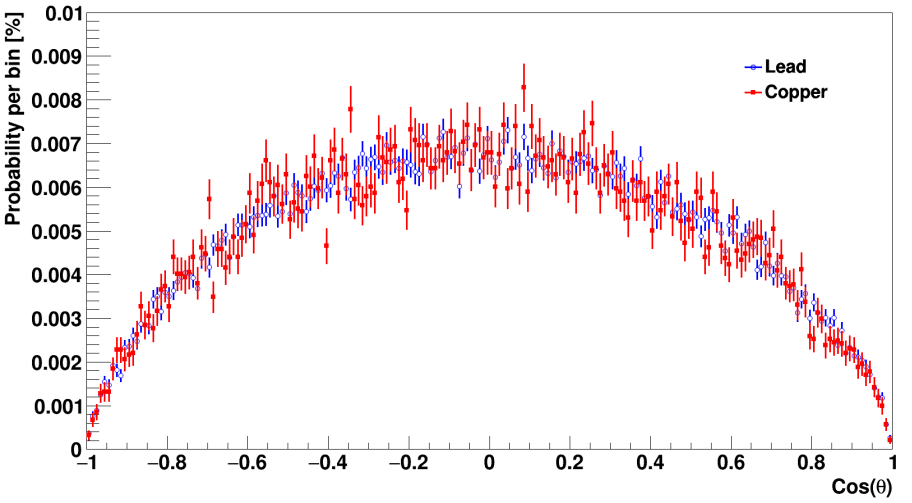

(b)

Figure 6.14: Simulated kinetic energy spectrum (a) and angular distribution (b) of neutrons emitted from the selected lead (blue) and copper (red) surface of the implemented MINIDEX Run 3 setup (see Fig. 6.13). The angle θ is defined as the angle between the neutron momentum direction and the z-axis. All given uncertainties are statistical only and are partially smaller than the size of the marker.

Table 6.3: External neutron yield predicted by simulation, Y_{Ext}^{Sim}, for lead and copper in MINIDEX. The simulated muons have a mean muon energy of (8.72 ± 0.01) GeV and (8.52 ± 0.01) GeV at the position before they enter the lead and copper target walls, respectively. Both neutron yields were calculated with the help of Eq. (3.1), using the number of muon tags (N_{μ}^{Sim}), the number of emitted neutrons from the selected surfaces (N_{n}^{Sim}) and the average track length of the muons in the target walls ($\overline{X}_{\mu}^{Sim}$). All given uncertainties are statistical only.

	Lead	Copper
Y_{Ext}^{Sim} $[10^{-5}\,g^{-1}\,cm^2]$ neutrons per muon tag	6.96 ± 0.02	2.93 ± 0.02
N_{μ}^{Sim} $[10^6]$	≈ 1.97	≈ 2.05
N_{n}^{Sim}	82275	28135
$\overline{X}_{\mu}^{Sim}$ [cm]	52.493 ± 0.001	52.460 ± 0.001

the lead surface is by a factor of 2.38 ± 0.02 higher than for copper, owing to a higher neutron production in lead.

6.5 Simulation Study of the Neutron Detection Probability

In order to evaluate the reliability of the neutron yield scaling procedure (see Section 3.2.1 and Section 8.5) and its systematic effects, a detailed Geant4 simulation study of neutrons in the MINIDEX Run 2 setup was performed. In this study the neutron detection probability and its dependence on the kinetic energy, the starting position and the momentum direction of neutrons within the MINIDEX Run 2 setup are investigated. Furthermore, the multiplicity of neutrons, induced by a single neutron within the setup, is studied.

6.5.1 Simulation Input

Neutrons with various monoenergetic energies were started in the left lead target wall of the MINIDEX Run 2 setup and are called simulated neutrons in the following. The neutrons investigated in this study have energies between 0.01 MeV and 10 GeV. This energy range corresponds to the neutron energies obtained by the neutron yield simulation (see Fig. 6.14). For each chosen individual energy, between 10^5 to $4 \cdot 10^6$ neutrons were simulated. For some neutron energies that

were studied in more detail (e.g. 0.01 MeV and 1 MeV), the number of simulated neutrons was higher than for the others, to obtain better statistics. In Fig. 6.15(a) the chosen energies and the corresponding number of simulated neutrons are depicted. All neutrons were distributed homogeneously within the left target wall

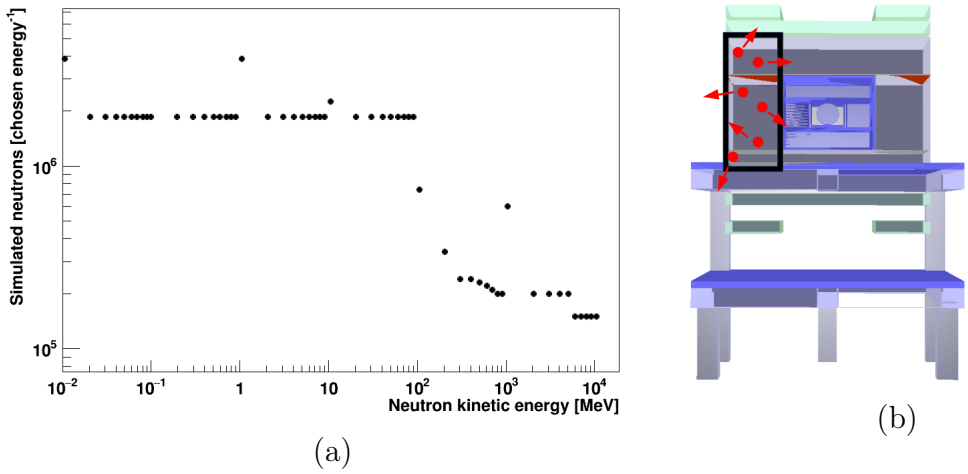

(a) (b)

Figure 6.15: (a) Number of simulated neutrons for the chosen neutron energies. In (b) a cross section of the implemented MINIDEX Run 2 setup is shown. Homogeneously distributed neutrons (red points) within the left lead target wall (black rectangle) of the setup were simulated with isotropic momentum distribution (red arrows).

and were simulated with an isotropic distribution of the neutron momenta. Note that each neutron was simulated individually. A cross section of the implemented MINIDEX Run 2 setup together with a few schematically displayed simulated neutrons are shown in Fig. 6.15(b). The red points indicate the homogeneous distribution of the simulated neutrons within the left target wall (black rectangle) whereas the red arrows represent their isotropic momentum distribution.

6.5.2 Neutron Detection Probability

In the following, the influence of the kinetic energy, the position and the momentum direction of the simulated neutrons on the neutron detection probability are investigated. For a neutron detection it is requested that for an individually simulated neutron at least one 2.2 MeV neutron capture gamma is detected with the germanium detectors. Note that this does not mean that the simulated neutron itself has been captured on hydrogen in the water and the subsequently released 2.2 MeV neutron capture gamma is detected. Depending on the energy

of the simulated neutron, further neutrons can be produced in the setup. These further neutrons also can get captured on hydrogen and lead to the detection of a 2.2 MeV gamma.

6.5.2.1 Kinetic energy of neutrons

The dependence of the probability to detect a 2.2 MeV gamma in the germanium detectors on the neutron kinetic energy is plotted in Fig. 6.16. For 0.01 MeV, the

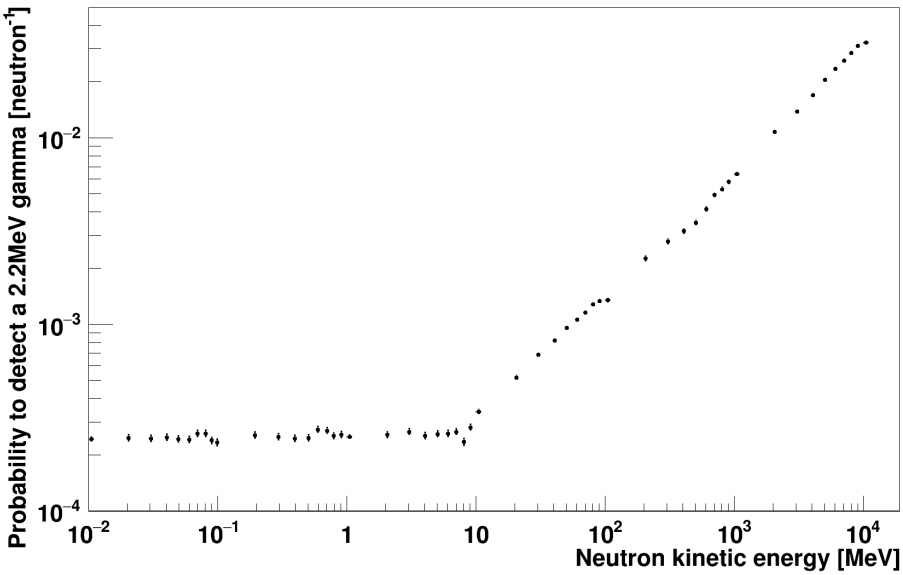

Figure 6.16: Dependence of the probability to detect a 2.2 MeV neutron capture gamma in the germanium detectors on the kinetic energy of the simulated neutrons. The neutrons were started in the left target wall of the MINIDEX Run 2 setup. See text for details. The given uncertainties are partially smaller than the size of the marker and are statistical only.

lowest simulated neutron energy, a detection probability of $(2.42 \pm 0.08) \cdot 10^{-4}$ was found. For 10 GeV neutrons, the highest simulated neutron energy, a detection probability of $(3.28 \pm 0.05) \cdot 10^{-2}$ was determined. It can be seen that the 2.2 MeV neutron capture gamma detection probability stays nearly flat for neutron energies $\lesssim 10$ MeV. This shows that the percentage of the neutrons reaching the water tank in this energy range is nearly independent of the energy of the simulated neutron. For energies above $\gtrsim 10$ MeV a rise of the distribution can be observed, owing to the further neutrons induced within the setup (the average nuclear binding energy per nucleon in lead is ≈ 8 MeV). These further neutrons

lead to a significantly higher neutron capture rate and therefore to a significantly higher 2.2 MeV gamma detection probability.

6.5.2.2 Starting position of neutrons

The dependence of the neutron detection probability on the starting x-position of the simulated neutrons within the left target wall was studied. A dependence on the y-and z-position was neither taken into account nor investigated. In Fig. 6.17 a cross section of the MINIDEX Run 2 setup together with a schematically drawn simulated neutron and its position within the setup is depicted. The germanium

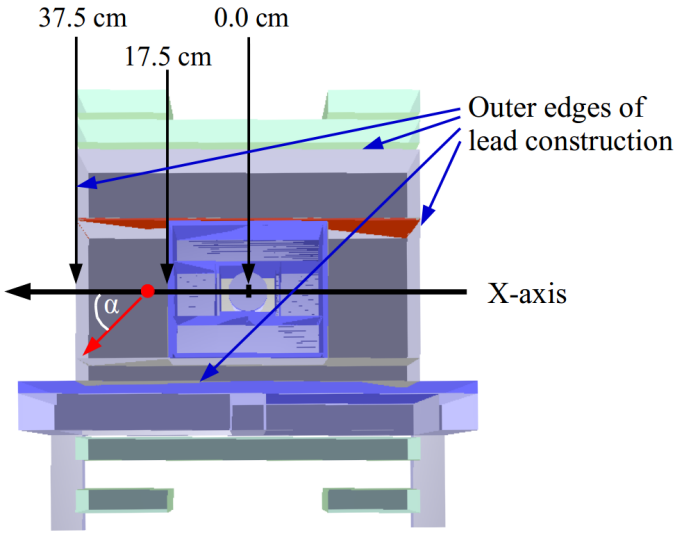

Figure 6.17: Cross section of the MINIDEX Run 2 setup. The red point schematically represents the starting position of a simulated neutron within the left target wall whereas the red arrow indicates its momentum direction. In black the x-axis and in white the angle α, defined as the angle between the momentum direction of the simulated neutron and the x-axis, is depicted.

detectors are located in the centre of the setup (i.e. at $x = 0.0$). At an x-position of 17.5 cm the water tank ends and the left target wall starts, extending up to an x-position of 37.5 cm. This means, the higher the x-position of the simulated neutrons is, the further away they are started (on average) from the water tank. In Fig. 6.18 the obtained dependence of the probability to detect a 2.2 MeV gamma on the starting x-position of the simulated neutrons is shown. The colours red, black and green represent three different simulated neutron energies. All displayed distributions are normalised to their respective integral. Owing to an

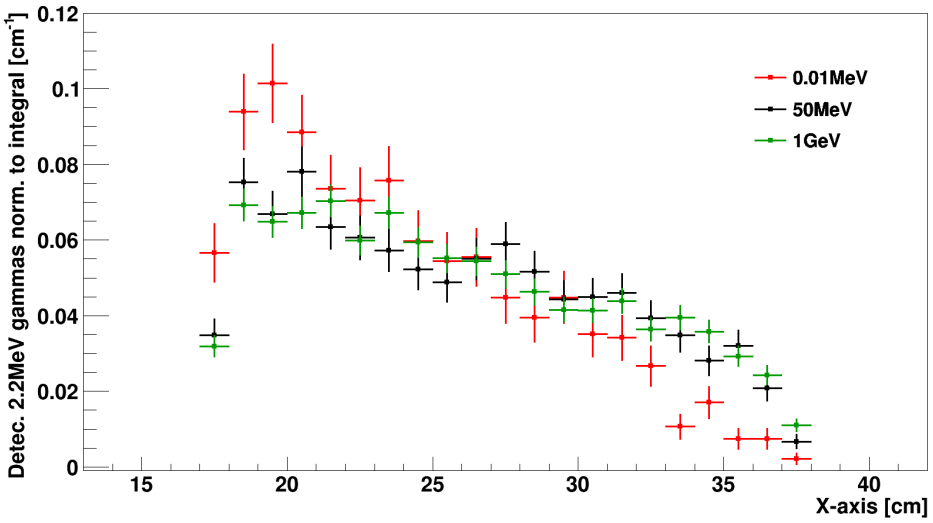

Figure 6.18: Dependence of the probability to detect a 2.2 MeV neutron capture gamma in the germanium detectors on the starting x-position of the simulated neutrons (see Fig. 6.17 for the location and the direction of the x-axis within the setup) for different simulated neutron energies. All distributions are normalised to their respective integral. The given uncertainties are statistical only.

increasing geometrical acceptance of the simulated neutrons to reach the water tank, the probability to detect a 2.2 MeV gamma rises for all three simulated neutron energies with a decreasing distance between the starting position and the water tank. The slope of the distributions for 50 MeV and 1 GeV neutrons is less steep than the one for 0.01 MeV neutrons. This results from the fact that 0.01 MeV neutrons do likely not induce further neutrons and hence themselves have to reach the water tank in order to create a 2.2 MeV gamma. For neutron energies $\gtrsim 10$ MeV it is likely that further neutrons are produced within the setup. These further neutrons significantly increase the 2.2 MeV gamma detection probability and therefore decrease the dependence on the simulated neutron to reach the water tank itself.

6.5.2.3 Starting angle of neutrons

The dependence of the 2.2 MeV neutron capture gamma detection probability on the angle between the momentum direction of the simulated neutrons and the x-axis of the setup, defined as α, was investigated. In Fig. 6.17 a simulated neutron (red point) and its corresponding momentum direction (red arrow) are schematically depicted. Note, momenta with values of $\cos(\alpha)$ between 0 and 1 point away

from the water tank whereas momenta with values of cos(α) between -1 and 0 move towards the water tank. The dependence of the probability to detect a 2.2 MeV neutron capture gamma on cos(α) is shown in Fig. 6.19. It is appar-

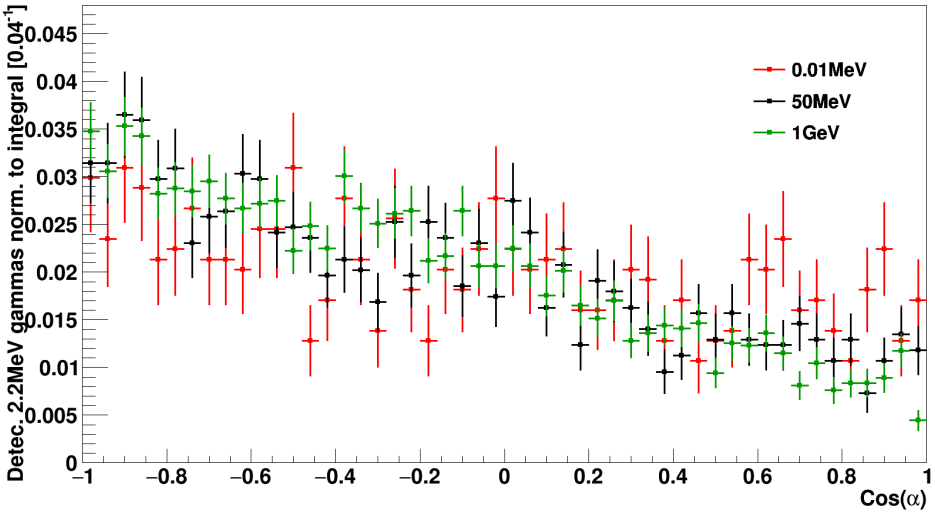

Figure 6.19: Dependence of the 2.2 MeV neutron capture gamma detection probability on cos(α) for different simulated neutron energies. Here, α represents the angle between the momentum direction of the simulated neutrons and the x-axis (see Fig. 6.17 for the location and the direction of the x-axis as well as the definition of α). All distributions are normalised to their respective integral. The shown uncertainties are statistical only.

ent that for all simulated neutron energies the probability to detect a 2.2 MeV gamma slightly decreases with an increasing value of cos(α). The distribution for 0.01 MeV neutrons (red) is less steep than the one for 1 GeV neutrons (green). This can be explained by the fact that low-energy neutrons (i.e. 0.01 MeV here) more likely scatter elastically in lead, and therefore easily change their momentum direction. In contrast to this, high-energy neutrons do not change their momentum direction so easily.

6.5.3 Neutron Production Multiplicity

The neutron production multiplicity $M_N^{Pro.}$, defined as the total number of neutrons produced for a single simulated neutron, was studied. All neutrons generated within the lead construction (see Fig. 6.17) are taken into account while the simulated neutron itself is not counted. Furthermore, in order to count the number of neutrons produced correctly, the following procedure has to be ap-

plied. When N neutrons are emitted in a neutron inelastic scattering reaction, then only a number of N-1 neutrons are actually produced and thus counted, as the reaction itself is triggered by an incident neutron.

In Fig. 6.20 (top panel) the $M_N^{Pro.}$ distribution is shown for four different simulated neutron energies. For each of the selected energies two different cases

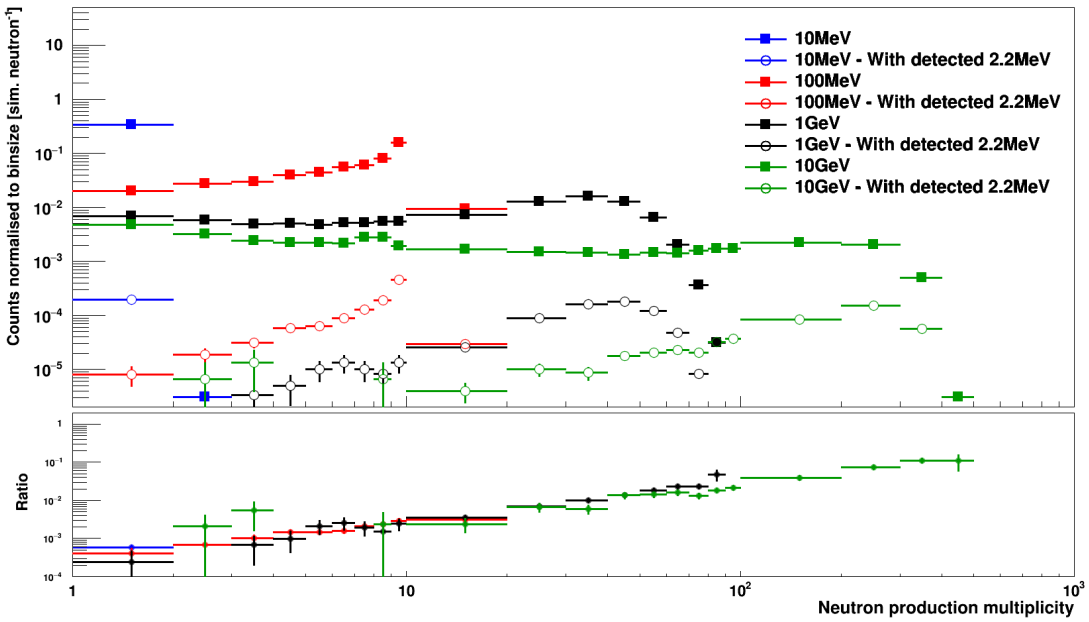

Figure 6.20: Neutron production multiplicity $M_N^{Pro.}$ (top panel) for simulated neutrons with different energies. $M_N^{Pro.}$ for all simulated neutrons is given in filled squares. For the subset of simulated neutrons, for which a 2.2 MeV gamma is detected in the germanium detectors, $M_N^{Pro.}$ is shown in open circles. In the bottom panel the ratios between $M_N^{Pro.}$ of the simulated neutrons with a detected 2.2 MeV gamma and $M_N^{Pro.}$ of all simulated neutrons are depicted. The given uncertainties are partially smaller than the size of the marker and are statistical only. See text for details.

are depicted. In the first case, represented by filled squares, $M_N^{Pro.}$ for all simulated neutrons is shown. In the second case, given by open circles, only simulated neutrons for which a 2.2 MeV neutron capture gamma was detected in the germanium detectors are shown. The highest observed $M_N^{Pro.}$ increases with the energy of the simulated neutrons. For simulated neutrons with an energy of 10 MeV (blue filled squares) a maximal $M_N^{Pro.}$ of 2 was found. For simulated 10 GeV neutrons (green filled squares) values of $M_N^{Pro.}$ up to ≈ 400 can be observed, owing to the larger available energy to induce further neutrons in the setup. It was found that for $\approx 66\,\%$ of all simulated 10 MeV neutrons, no further neutrons are induced.

For 100 MeV, 1 GeV and 10 GeV simulated neutrons, this number is reduced to $\approx 41\,\%$, $\approx 38\,\%$ and $\approx 36\,\%$, respectively. In the bottom panel of Fig. 6.20 the ratios between $M_N^{Pro.}$ of the simulated neutrons with a detected 2.2 MeV gamma and $M_N^{Pro.}$ of all simulated neutrons are depicted. A similar rise of the ratio with an increasing $M_N^{Pro.}$ can be observed for all simulated neutron energies. The consistent shapes of the distributions indicate that the probability to detect a 2.2 MeV gamma depends mainly on the total number of neutrons produced within the setup. This can be explained if the energies, the momentum directions and the positions of the further induced neutrons are consistent for the four simulated neutron energies.

The mean neutron production multiplicity $\overline{M}_N^{Pro.}$ for the four simulated neutron energies and the two investigated cases is given in Table 6.4. A correlation

Table 6.4: Mean neutron production multiplicity $\overline{M}_N^{Pro.}$ of simulated neutrons that were started in the left target wall of the MINIDEX Run 2 setup. $\overline{M}_N^{Pro.}$ for all simulated neutrons and for the subset of simulated neutrons, for which a 2.2 MeV gamma is detected in the germanium detectors, is given. In addition, the ratios between $\overline{M}_N^{Pro.}$ for simulated neutrons with a 2.2 MeV gamma and $\overline{M}_N^{Pro.}$ for all simulated neutrons are stated. All given uncertainties are statistical only.

Simulated neutron energy	Mean neutron production multiplicity		Ratio
	All	With detected 2.2 MeV gamma	
10 MeV	0.33574 ± 0.00031	0.582 ± 0.018	1.73 ± 0.05
100 MeV	4.303 ± 0.005	7.96 ± 0.07	1.850 ± 0.016
1 GeV	20.868 ± 0.026	41.43 ± 0.22	1.985 ± 0.011
10 GeV	108.25 ± 0.28	228.0 ± 1.1	2.106 ± 0.012

between an increasing energy of the simulated neutrons and an increasing $\overline{M}_N^{Pro.}$ is apparent. For the subsets of simulated neutrons with a detected 2.2 MeV gamma, $\overline{M}_N^{Pro.}$ is for all four simulated neutron energies by a factor of about 2 higher than the corresponding value for all simulated neutrons.

6.5.4 Conclusion of Neutron Simulation Study

A dependence of the probability to detect a 2.2 MeV neutron capture gamma on the position, the momentum direction and the energy of the simulated neutrons was found. Furthermore, it was shown that the neutron production multiplicity significantly increases with an increasing energy of the simulated neutron. These are important observations that are used to give a feedback on the reliability and the systematic effects of the neutron yield scaling procedure, used to determine the external neutron yield of lead and copper for MINIDEX (see Section 3.2.1 and Section 8.5).

Chapter 7

Determination of Measured Observables

The strategies to determine the neutron signals as well as the neutron signal multiplicity events from the experimental MINIDEX data sets are presented. These strategies are similar to some extent to the ones applied to the MC data sets, as described in the previous section.

7.1 Determination of Neutron Signals

The procedure applied to identify the neutron signals from the acquired experimental MINIDEX Run 2 and Run 3 data sets is illustrated in Fig. 7.1. After each

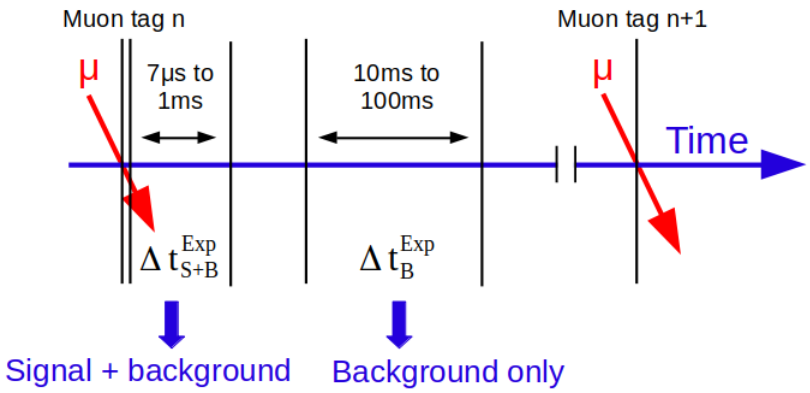

Figure 7.1: Schematic illustration of the experimental neutron signal determination procedure applied to the MINIDEX Run 2 and Run 3 experimental data sets. Events that occur between 7 μs and 1 ms after a muon tag are collected in Δt^{Exp}_{S+B}, the signal plus background time window. All events that occur between 10 ms and 100 ms after a muon tag are collected in Δt^{Exp}_{B}, the background-only time window. Taken from [94].

muon tag a signal plus background time window, Δt_{S+B}^{Exp}, is opened. In this time window all recorded energy depositions in the germanium detectors, occurring between 7 μs and 1 ms after the muon tags, are collected. Neutron signals as well as energy depositions from various background sources are collected in this time window. From 10 ms to 100 ms after each muon tag a second time window, Δt_{B}^{Exp}, is opened. In this second time window, energy depositions in the germanium detectors from background sources only are collected. If two consecutive muon tags appear within less than 100 ms, the length of Δt_{B}^{Exp} for the first muon tag is shortened accordingly. This shortening leads to an average reduction of the length of Δt_{B}^{Exp} by 9.4 % in Run 2. In Run 3 Δt_{B}^{Exp} is reduced in average by 3.2 % for the muon tags of each side individually. The smaller reduction for Run 3 results from an independent analysis of the muon tags from the two sides. Note, the plots within this section are shown for the experimental MINIDEX Run 2 data set as an example.

In Fig. 7.2(a) the time difference between observed energy depositions in the germanium detectors and the previous muon tag are depicted. Only events that appear at an energy within (2223.3 ± 3.7) keV, corresponding to the $\pm 3\,\sigma$ energy resolution of the combined germanium detectors (i.e. both individual germanium spectra added up) at 2.2 MeV, are taken into account. It is apparent that the number of detected events with an energy of ≈ 2.2 MeV is clearly enhanced in the first millisecond after the muon tags. The simulation predicts (see Section 6.2) that (98.7 ± 1.0) % of all 2.2 MeV gammas, resulting of the capture of muon-induced neutrons on hydrogen, can be detected in this first millisecond. Further, it can be seen that the number of events for time differences > 1 ms is constant. These events result, for example, from radioactive decays occurring in the setup or from muons (including their induced particles) that do not pass through the scintillators required for a muon tag. In Fig. 7.2(b) the distribution for all measured time differences < 3 ms is depicted. The sum of a falling exponential function plus a constant was fit from 7 μs to 3 ms to this distribution. The falling exponential function represents the time constant of the neutron signals, resulting from the propagation of the thermalised neutrons within the water and the plastic of the tank. The constant part of the fit function describes the background that is independent of the muon tags. The fit yields a mean delay of the neutron signals of (159 ± 8) μs. This value agrees within $2\,\sigma$ uncertainties with the (180 ± 8) μs predicted by the simulation. A large number of events were found in the first 10 μs after the muon tags (see first bin in Fig. 7.2(b)). These very early events are predicted by the simulation (see Section 6.2) and result predominantly from energy depositions of electrons and gammas, induced in the

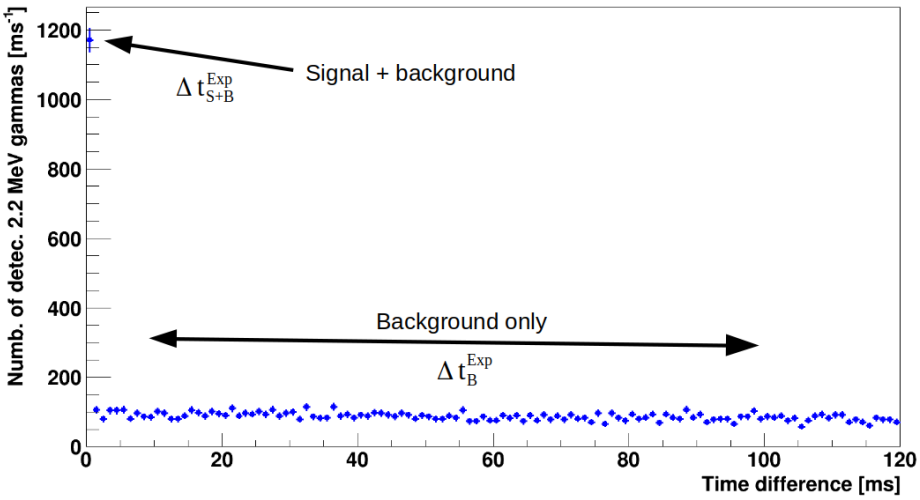

(a)

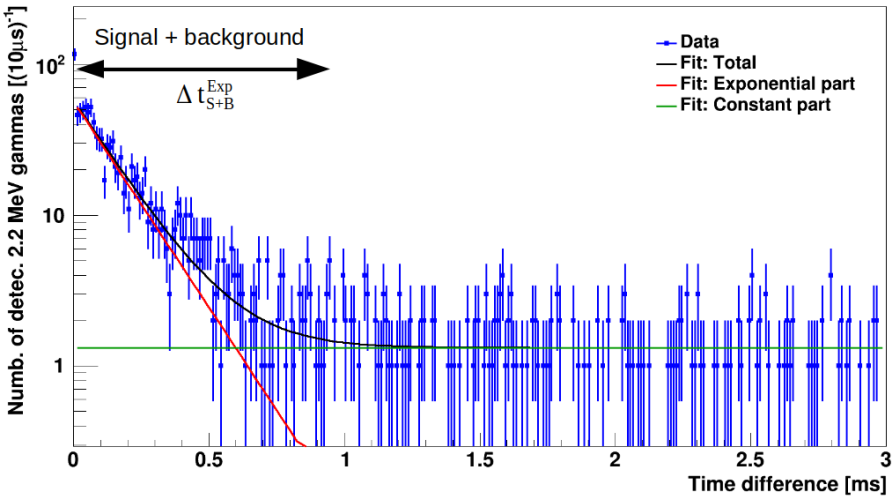

(b)

Figure 7.2: Measured time differences between energy depositions in the germanium detectors within (2223.3 ± 3.7) keV and the corresponding muon tag. The chosen energy window corresponds to the $\pm 3\,\sigma$ energy resolution of the combined germanium detectors at 2.2 MeV. In (a) all time differences < 120 ms are shown while in (b) a zoom on time differences < 3 ms is given. In (b) an applied fit function, representing the sum of a falling exponential function plus a constant, is depicted in black. The exponential part of the fit function (red) represents the neutron signals whereas the constant part (green) describes the background that is independent of muon tags. The exponential part of the fit yields a mean delay of the measured neutron signals of $(159 \pm 8)\,\mu$s. Only events of the experimental MINIDEX Run 2 data set are shown. The distributions of the two individual germanium detectors are added up. The given uncertainties are statistical only.

setup by the tagged muons. However, these events are rejected by the lower time cut of 7 μs of Δt_{S+B}^{Exp}. The 1 ms as a higher time cut on Δt_{S+B}^{Exp} was selected, as the simulation predicts that beyond this value only $< 2.3\,\%$ of the 2.2 MeV gammas, originating from the capture of muon-induced neutrons on hydrogen, can be detected. Although the neutron signals beyond 1 ms are not collected in Δt_{S+B}^{Exp}, they are considered in the systematics (see Section 8.3.1). Owing to the conservatively selected lower time cut of 10 ms for Δt_{B}^{Exp}, only events that are not related to a tagged muon are collected.

The measured neutron signal rate, R_{S}^{Exp}, is defined as the number of observed neutron signals per muon tag. For its determination, the energy depositions in the germanium detectors, collected within Δt_{S+B}^{Exp} and Δt_{B}^{Exp}, are summed up. In Fig. 7.3 the resulting spectra for the two time windows, called signal plus background spectrum (for Δt_{S+B}^{Exp}) and background-only spectrum (for Δt_{B}^{Exp}) in the following, are depicted. Here, only events in the germanium detectors of MINIDEX Run 2 with energies < 2800 keV are considered. Various gamma

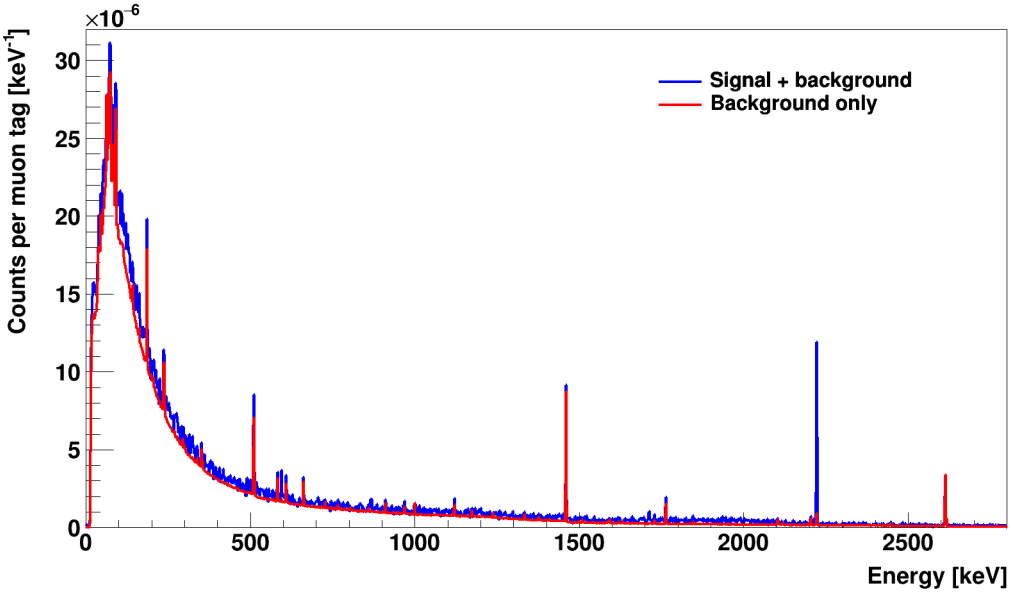

Figure 7.3: Measured energy spectra of events in the germanium detectors. In blue the events of the Δt_{S+B}^{Exp} time window are depicted whereas the events in the red spectrum correspond to Δt_{B}^{Exp}. Both spectra are normalised in a way to represent the number of measured events in the germanium detectors per muon tag. The spectra of the two individual germanium detectors are added up. Only events of the MINIDEX Run 2 data set are considered.

lines from natural radioactivity can be observed in the spectra, for examples the lines from the radioactive isotopes ^{40}K (1460.8 keV) and ^{208}Tl (2614.5 keV). Note that these two lines are used to calibrate the germanium detectors (see Section 5.1.3.1). At 2.2 MeV the gamma line from neutron capture on hydrogen can be seen in both spectra. This line is significantly increased in the case of the signal plus background spectrum, owing to the muon-induced neutrons. The signal plus background spectrum is normalised to the number of muon tags and represents an effective measurement time of 7.10 h in the case of the MINIDEX Run 2 data set. The background-only spectrum is normalised to 993 μs, the length of Δt_{S+B}^{Exp}. In the case of the MINIDEX Run 2 data set it represents an effective measurement time, LT_{Eff}, of 603.66 h. Both spectra are thus normalised in a way to represent the number of measured events in the germanium detectors per muon tag. In order to determine R_S^{Exp}, both spectra are individually fit from 2217 keV to 2228 keV with the sum of a Gaussian and a first order polynomial function. In Fig. 7.4 the two spectra are depicted together with the applied fits in the energy region around the 2.2 MeV neutron capture gamma line. The Gaussian functions of the fits represent the 2.2 MeV gammas from neutron capture on hydrogen that deposited their full energy in the germanium detectors. For the signal plus background spectrum these correspond predominantly to the 2.2 MeV neutron capture gammas related to tagged muons (i.e. neutron signals). However, also stochastic 2.2 MeV neutron capture gammas (background) are included. In the case of the background-only spectrum the 2.2 MeV neutron capture gammas correspond to stochastic background events only. In both cases, the first order polynomial function describes all other background events in the investigated energy range. This background component, which results predominantly from stochastic background gammas, is called stochastic gamma background in the following. R_S^{Exp} is determined by subtracting the area of the Gaussian applied to the background-only spectrum from the area of the Gaussian applied to the signal plus background spectrum.

The signal to background ratio of the measured neutron signals, $(S/N)^{Exp}$, was evaluated for both experimental data sets. For this purpose, the number of background events within an energy range of $\pm$ 5.2 keV (corresponds to $\pm\, 5\,\sigma$ energy resolution of germanium detectors at 2.2 MeV) around the 2.2 MeV gamma line were determined with the help of both fits from Fig. 7.4. Note, these background events include stochastic 2.2 MeV neutron capture gammas as well as all other background events in the $\pm\, 5\,\sigma$ energy range.

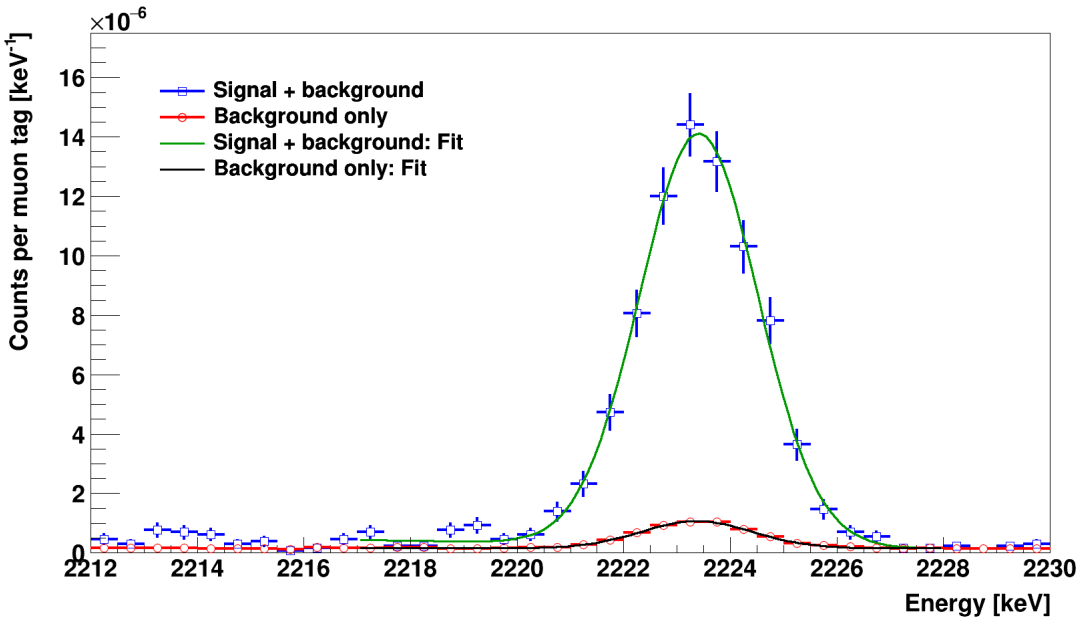

Figure 7.4: Measured energy spectra of events in the germanium detectors around the 2.2 MeV neutron capture gamma line. The spectra of the two individual germanium detectors are added up. In blue the signal plus background spectrum and in red the background-only spectrum is depicted. Both spectra are normalised to represent the number of measured events in the germanium detectors per muon tag. In order to determine R_S^{Exp}, the measured neutron signal rate, both spectra are individually fit with the sum of a Gaussian and a first order polynomial function (green and black). Only events of the experimental MINIDEX Run 2 data set are considered. The given uncertainties are partially smaller than the size of the marker and are statistical only.

In Fig. 7.5 the energy spectrum of the Big top scintillator is depicted for two different sets of events with a muon tag. While in blue all muon tags are shown, the red spectrum depicts only those events for which an energy deposition of (2223.3 ± 3.7) keV ($\pm 3\,\sigma$ energy resolution) was observed in the germanium detectors within the time cuts of Δt_{S+B}^{Exp}. Note that here a small number of events in the red spectrum results from background sources. It is apparent that the energy spectrum of the Big top scintillator is shifted to higher energies for muon tags with an energy deposition in the germanium detectors. A shift of the mean measured energy in the Big top scintillator by (2.9 ± 0.5) MeV was found. Events with a large number of muon-induced shower particles, originating from the passage of muons through the laboratory overburden and depositing large amounts of energy in the Big top scintillator, can lead to a significantly increased probability to detect a neutron signal. The observed shift of the mean

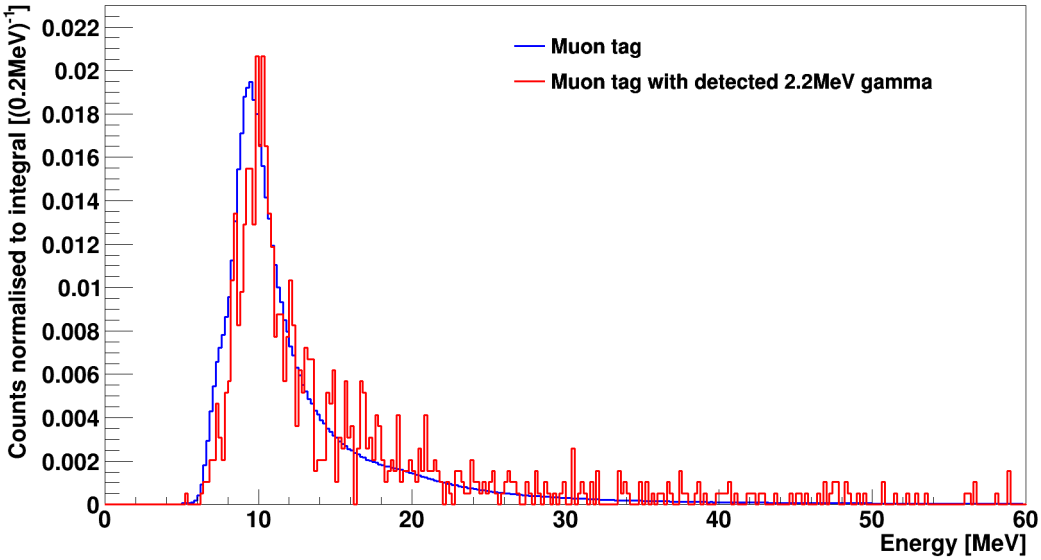

Figure 7.5: Measured energy spectrum of the Big top scintillator for all events with a muon tag (blue) and for the subset of events (red), for which an energy deposition in the germanium detectors within (2223.3 ± 3.7) keV ($\pm 3\,\sigma$ energy resolution) and within the time window Δt_{S+B}^{Exp} was observed. The mean measured energy in the Big top scintillator is by (2.9 ± 0.5) MeV higher in the case of a 2.2 MeV energy deposition in the germanium detectors. Both spectra are normalised to their respective integral. Only events of the experimental MINIDEX Run 2 data set are considered.

measured energy in the Big top scintillator could therefore indicate a significant contribution of such neutron signals to R_S^{Exp}. However, the Geant4 and the FLUKA simulations in Section 9.3 predict that the majority of detected neutron signals in MINIDEX Run 2 results from muon interactions within the target walls of the setup.

7.2 Determination of Neutron Signal Multiplicity Events

In a neutron signal multiplicity event at least two individual 2.2 MeV neutron capture gammas have to be detected in the high-purity germanium detectors for the same muon tag. The individual 2.2 MeV gammas can be detected in the same or two different germanium detectors. Only energy depositions that occur within the time window Δt_{S+B}^{Exp} (i.e. between 7 μs and 1 ms after each muon tag) for muon tags of the Run 2 data set are considered in the following.

Four different background contributions to the neutron signal multiplicity events have to be considered and evaluated:

1. Two 2.2 MeV gammas from the stochastic gamma background that is not related to neutron captures on hydrogen.

2. One 2.2 MeV gamma from the stochastic gamma background and one 2.2 MeV neutron capture gamma. The 2.2 MeV neutron capture gamma can either be a neutron signal or result from the stochastic neutron background.

3. Two 2.2 MeV gammas from the stochastic neutron background.

4. One neutron signal and one 2.2 MeV gamma from the stochastic neutron background.

The individual background contributions are assessed with the help of the energy spectrum depicted in Fig. 7.6. It represents all measured energy depositions in

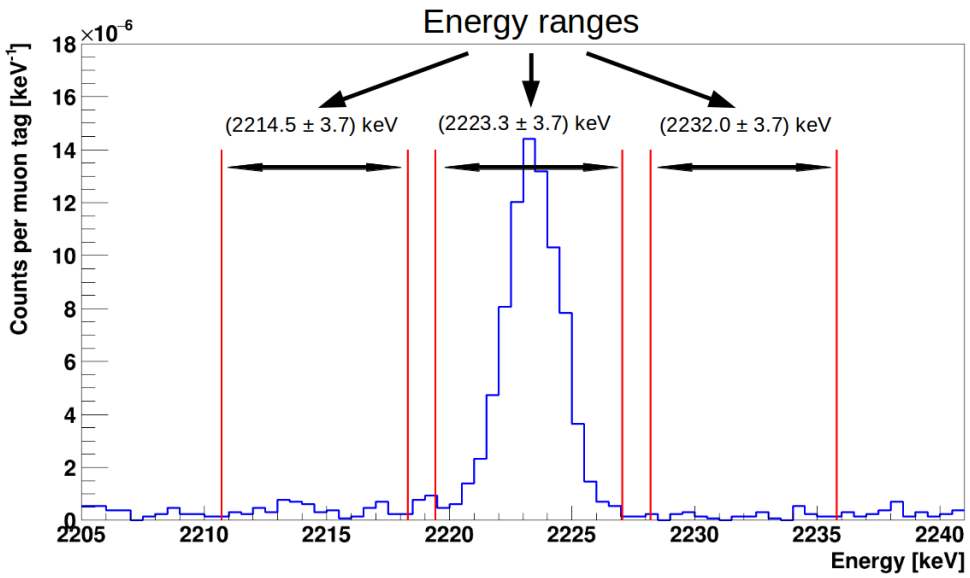

Figure 7.6: Measured energy spectrum of the germanium detectors around the 2.2 MeV neutron capture gamma line. Only energy depositions of MINIDEX Run 2 that occur within Δt_{S+B}^{Exp} are included. The spectra of the two individual germanium detectors are added up. Three energy ranges, used to determine the contribution of backgrounds to the number of neutron signal multiplicity events, are indicated. The spectrum is normalised to represent the number of measured energy depositions in the germanium detectors per muon tag.

the germanium detectors within Δt_{S+B}^{Exp}. The spectrum is normalised to represent the number of measured energy depositions in the germanium detectors per muon tag. Three energy ranges are defined in the spectrum at (2214.5 ± 3.7) keV, (2223.3 ± 3.7) keV and (2232.0 ± 3.7) keV. The width of the energy ranges corresponds to the $\pm 3\,\sigma$ energy resolution of the combined energy spectrum of the germanium detectors at 2.2 MeV. The events within the energy ranges of the spectrum are grouped into five different event classes, EC_I to EC_V. The classification of the different event classes is given in Table 7.1. The corresponding events are

Table 7.1: Classification of the different event classes (EC_i) by the type of events and the energy range. Also the method, used to determine the rate of events for the different event classes, is given. The last column states the obtained values for the rates of the different event classes. The given uncertainties are statistical only. For details see text.

Event class	Event type	Energy range [keV]	Determination method	Q_i $[10^{-6}]$ per muon tag
EC_I	Stochastic gamma background	2214.5 ± 3.7	Measured	2.94 ± 0.34
EC_{II}	Neutron signals	2223.3 ± 3.7	Fit	36.1 ± 1.3
EC_{III}	Stochastic neutron background	2223.3 ± 3.7	Fit	2.38 ± 0.05
EC_{IV}	Stochastic gamma background	2223.3 ± 3.7	Approximated	2.25 ± 0.21
EC_V	Stochastic gamma background	2232.0 ± 3.7	Measured	1.55 ± 0.24

classified by the event type as well as by the corresponding energy range.

The four different background contributions are determined with the help of the rates Q_i (see also Table 7.1), which represent the number of energy depositions in the germanium detectors per muon tag for the corresponding event class EC_i. The values for Q_{II} and Q_{III} are obtained from the fits depicted in Fig. 7.4. The Q_I and Q_V are directly determined from the rate of events in the energy ranges (2214.5 ± 3.7) keV and (2232.0 ± 3.7) keV of Fig. 7.6, respectively. The rate Q_{IV} was approximated by $2\,Q_{IV} = Q_I + Q_V$. All determined individual background contributions, which are given at the end of the section, are expressed as N_j, the

number of expected background events for the full MINIDEX Run 2 data set. Note that in principle the background contributions N_1 and N_2 can be determined directly by measurement. However, limited statistics require their calculation.

The first background contribution depends on the rate Q_{IV} and $\#MT_{Run2}$, the total number of muon tags in the Run 2 data set. The expected number of events for the first background, N_1, can be calculated [138] by

$$N_1 = 2\,(Q_{IV})^2\,\#MT_{Run2} \tag{7.1}$$

$$= 2\,(\frac{Q_I + Q_V}{2})^2\,\#MT_{Run2}. \tag{7.2}$$

Furthermore, this background was searched for in the Run 2 data set. For this purpose, it was requested that two energy depositions in region EC_I or EC_V are detected within Δt^{Exp}_{S+B} of the same muon tag. However, no such coincident event was found.

The second background contribution depends on the rates Q_{II}, Q_{III} and Q_{IV}. The expected number of events for the second background, N_2, can be calculated by

$$N_2 = 2\,Q_{IV}\,(Q_{II} + Q_{III})\,\#MT_{Run2} \tag{7.3}$$

$$= 2\,(\frac{Q_I + Q_V}{2})\,(Q_{II} + Q_{III})\,\#MT_{Run2}. \tag{7.4}$$

This background can in principle also be directly determined by measurement. This was carried out by requesting an energy deposition within $(2223.3 \pm 3.7)\,keV$ (EC_{II}, EC_{III} or EC_{IV}) and a further one in EC_I or EC_V within Δt^{Exp}_{S+B} of the same muon tag. Note, this procedure overestimates the background slightly, as all events from EC_{II}, EC_{III} and EC_{IV} are included instead of the ones from EC_{II} and EC_{III} only. Nevertheless, no such coincident event could be identified.

The third background contribution is determined by the rate Q_{III}. The expected number of events for the third background, N_3, can be calculated by

$$N_3 = 2\,(Q_{III})^2\,\#MT_{Run2}. \tag{7.5}$$

The fourth background contribution depends on the rates Q_{II} and Q_{III}. The expected number of such events, N_4, can be calculated by

$$N_4 = 2\,Q_{II}\,Q_{III}\,\#MT_{Run2}. \tag{7.6}$$

In Table 7.2 the calculated expected number of background events, N_j, for the different backgrounds are given. The calculated total background contribution to the neutron signal multiplicity events of the full MINIDEX Run 2 data set is $\approx 10^{-2}$, which is $\ll 1$. Consequently the contribution of backgrounds can be neglected. Furthermore, no background event was directly measured, which is in good agreement with the predictions. The measured neutron signal multiplicity events are evaluated as R_M^{Exp}, the number of neutron signal multiplicity events per muon tag.

Table 7.2: Calculated expected number of background events, N_j, to the neutron signal multiplicity events of the MINIDEX Run 2 data set. The N_j are labelled accordingly to the numbering in the text. The given uncertainties are statistical only. See text for details.

	Calculated
Total	$(9.8 \pm 0.5) \cdot 10^{-3}$
N_1	$(2.61 \pm 0.34) \cdot 10^{-4}$
N_2	$(4.5 \pm 0.4) \cdot 10^{-3}$
N_3	$(2.93 \pm 0.08) \cdot 10^{-4}$
N_4	$(4.74 \pm 0.19) \cdot 10^{-3}$

Chapter 8

Results and Discussion

In the following, the resulting measured and simulated number of neutron signals and neutron signal multiplicity events as well as the corresponding neutron signal and neutron signal multiplicity event rates (R_S and R_S) are given, compared and discussed. Also the systematic uncertainties are discussed and quantified.

8.1 Measured and Simulated Neutron Signals

In the experimental lead data sets of Run 2 and Run 3 a total number of $3.39 \cdot 10^7$ muon tags ($2.57 \cdot 10^7$ from Run 2 and $0.82 \cdot 10^7$ from Run 3) and 1195 ± 38 neutron signals (932 ± 34 from Run 2 and 263 ± 18 from Run 3) were identified. For lead from Run 2 the signal to background ratio of the measured neutron signals, $(S/N)^{Exp}$, was determined to be 6.7 ± 0.5. $(S/N)^{Exp}$ for the measured lead neutron signals from Run 3 was found to be 5.7 ± 0.8. For the MC lead data sets of Run 2 and Run 3 a total number of $3.81 \cdot 10^7$ muon tags ($2.12 \cdot 10^7$ from Run 2 and $1.69 \cdot 10^7$ from Run 3) and 1285 neutron signals (712 from Run 2 and 573 from Run 3) have been obtained.

The analysis of the muon tags for the two individual sides of the MC MINIDEX Run 2 data set yielded values for R_S^{Sim} that are in agreement within statistical uncertainties. In addition, R_S^{Sim} for the muon tags on the lead side of the Run 3 setup is in agreement within statistical uncertainties with R_S^{Sim} from Run 2. The analysis of the corresponding experimental data sets confirmed these observations. Hence, the experimental lead data sets as well as the MC lead data sets were respectively combined.

Using the combined experimental and MC data set, R_S^{Exp} and R_S^{Sim} for lead were determined to be $(3.52 \pm 0.11) \cdot 10^{-5}$ and $(3.37 \pm 0.09) \cdot 10^{-5}$, respectively.

In the experimental data set of copper $8.36 \cdot 10^6$ muon tags and 106 ± 12 neutron signals were identified. For the measured neutron signals of copper a

value of 2.4 ± 0.4 was determined for $(S/N)^{Exp}$. The analysis of the MC data set of copper resulted in a number of $1.75 \cdot 10^7$ muon tags and 309 neutron signals. Using the measured and simulated values for copper, R_S^{Exp} and R_S^{Sim} were determined to be $(1.27 \pm 0.14) \cdot 10^{-5}$ and $(1.77 \pm 0.10) \cdot 10^{-5}$, respectively.

It should be noted that the number of 2.2 MeV gammas, found for the individual germanium detectors for any experimental or MC data set, agrees well with the expectations. The number of detected 2.2 MeV gammas is expected to be different for the individual germanium detectors, resulting from the different detector masses (see Section 4.3.2).

8.2 Measured and Simulated Neutron Signal Multiplicity Events

In the experimental MINIDEX Run 2 data set of lead 5 neutron signal multiplicity events were identified. In comparison to this, in the MINIDEX Run 2 MC lead data set 26 neutron signal multiplicity events were determined. All experimentally obtained neutron signal multiplicity events result from the detection of exactly two 2.2 MeV neutron capture gammas for the same tagged muon. However in the MC data set two neutron signal multiplicity events with three detected 2.2 MeV neutron capture gammas for the same tagged muon were found. Together with the corresponding number of muon tags, R_M^{Exp} and R_M^{Sim} were determined to be $(0.19\,^{+\,0.11}_{-\,0.09}) \cdot 10^{-6}$ and $(1.23 \pm 0.24) \cdot 10^{-6}$, respectively.

8.3 Investigation of Systematic Uncertainties on Neutron Signal Rates

Various sources of systematic uncertainties on the measured and simulated neutron signal rates R_S were identified and investigated. This investigation is presented in the following and is split into Section 8.3.1 and Section 8.3.2 for R_S^{Exp} and R_S^{Sim}, respectively. At first, a list of the investigated systematics is given in both sections. Afterwards, the individual sources are discussed and their influences on the corresponding R_S determined. At the end of both sections the obtained total systematic uncertainties are given.

8.3.1 Systematic Uncertainties of the Experimental Data Analysis

The systematic uncertainties on R_S^{Exp}, δR_S^{Exp}, of the experimental data analysis of lead and copper are discussed. The following individual systematics have been investigated:

- Accidental coincidences in the muon tag determination procedure
- Scintillator energy resolution and stability of scintillator signal gain
- Energy reconstruction procedure of scintillator pulses
- Energy calibration of scintillator panels
- Time stamps of energy depositions in scintillators
- Time stamps of energy depositions in germanium detectors
- Fitting of energy region around 2.2 MeV neutron capture gamma line
- Length and position of Δt_{S+B}^{Exp}
- Length and position of Δt_{B}^{Exp}
- Positioning of scintillator panels
- Positioning, size and dead layer thickness of germanium detectors
- Presence of an additional neutron detector in the vicinity of the setup

Accidental Coincidences in the Muon Tag Determination Procedure

In the determination of muon tags in the experimental data analysis, contributions from backgrounds were not considered. Energy depositions from background sources that are seen by the scintillators originate mainly from radioactivity as well as muon-induced shower particles which are not correlated to the actual investigated muon. However, these energy depositions can lead to so-called accidental muon tags. Both backgrounds are expected to have a constant rate (for any of the scintillators) over the whole measurement time. Their influence on R_S^{Exp}, resulting from accidental muon tags, is assessed the following way. The highest probability for an accidental muon tag is for the case in which three scintillators on one side of the setup observe energy depositions from the same muon or any of its induced particles, while the fourth scintillator observes an energy deposition from a background source. The contribution of such accidental muon tags to the total muon tag rate is estimated. As an example for the case in

which Big top, Big bot and Small1 observe a coincident signal (fulfilling the muon tag determination procedure conditions, see Section 5.2) and Small3 detects an accidental signal, the accidental coincidence rate can be calculated [138] as

$$\mathrm{R}_{\mathrm{Acc}}^{\mathrm{Exp}} = 2 \cdot \mathrm{R}_{\mathrm{TBS1}}^{\mathrm{Exp}} \cdot \mathrm{R}_{\mathrm{S3}}^{\mathrm{Exp}} \cdot \Delta\mathrm{T}. \tag{8.1}$$

Here $\mathrm{R}_{\mathrm{TBS1}}^{\mathrm{Exp}}$ is the rate of events for which the three scintillators Big top, Big bot and Small1 detect a coincident signal. This rate was found to be $2.03\,\mathrm{s}^{-1}$. Note, the statistical uncertainty for any rate given in this accidental coincidences study is $< 1\,‰$. The quantity $\mathrm{R}_{\mathrm{S3}}^{\mathrm{Exp}}$ represents the rate of all events for which energy depositions above 5 MeV are observed in the Small3 scintillator. The rate of these events was determined to be $8.68\,\mathrm{s}^{-1}$. The ΔT in Eq. (8.1) stands for the maximal time difference of 60 ns allowed in the muon tag determination procedure (see Section 5.2). With the stated values an accidental muon tag rate of $2.11 \cdot 10^{-6}\,\mathrm{s}^{-1}$ was determined. The contributions of all other configurations, for which three scintillators detect correlated signals and one scintillator measures an accidental but coincident energy deposition, are similar. Furthermore, all other cases in which more than one scintillator at the same time detects an accidental coincident energy deposition are less probable. As a result, the overall accidental muon tag rate is by many orders of magnitude smaller than the actual muon tag rate of $1.14\,\mathrm{s}^{-1}$. The influence of the accidental muon tags on $\mathrm{R}_{\mathrm{S}}^{\mathrm{Exp}}$ can be consequently neglected.

Scintillator Energy Resolution and Stability of Scintillator Signal Gain

The energy resolution of the used scintillators was investigated in Section 5.1.2.3. Upper limits on the energy resolution of the small and big scintillators of 1.2 MeV and 1.5 MeV were determined, respectively. Further, in Section 5.1.2.4 the stability of the scintillator signal gain was studied. It was observed that slight signal gain changes in the scintillators resulted in shifts of the Landau distributions. The maximal observed shifts in any scintillator and any run were found to be < 200 keV. The influence of both effects on $\mathrm{R}_{\mathrm{S}}^{\mathrm{Exp}}$ was investigated. This was carried out by simultaneously increasing/decreasing the energy cuts, used in the muon tag determination procedure (see Section 5.2), by 1.4 MeV for the small and 1.7 MeV for the big scintillators (sum of scintillator energy resolution and maximal shift of Landau position), respectively. Lower energy cuts lead to an increased background collection whereas higher energy cuts result in a loss of actual muons. The determined systematic uncertainties on $\mathrm{R}_{\mathrm{S}}^{\mathrm{Exp}}$ ($\delta\mathrm{R}_{\mathrm{S:\,energy\,res.}}^{\mathrm{Exp}}$),

expressed in number of 10^{-5} 2.2 MeV gammas per muon tag, are $+0.07$ and $+0.03$ for lead and copper, respectively.

Energy Reconstruction Procedure of Scintillator Pulses

The energy reconstruction procedure of scintillator pulses has an effect on the consideration of scintillator events in the muon tag determination procedure (see Section 5.2), due to the scintillator energy cuts. The energy reconstruction of the measured scintillator pulses was carried out with a trapezoidal filter. For this filter a gap time of 32 ns and a peak time of 16 ns was selected. The precision of the energy reconstruction algorithm depends on the width and the rise time of the measured PMT pulses. The dependence of R_S^{Exp} on the selected gap and peak time was studied with the help of simulation. The simulated deposited energies in the scintillators were integrated for 24 ns and 40 ns, instead of the standard 32 ns. With the obtained different scintillator events, the MC data analysis was repeated and the systematic uncertainties on R_S^{Sim} for lead and copper were determined in percentage terms. These simulation predicted percentages were afterwards applied to R_S^{Exp}. The resulting experimental systematic uncertainties on R_S^{Exp} ($\delta R_{S:\,\text{energy recon.}}^{Exp}$), expressed in number of 10^{-5} 2.2 MeV gammas per muon tag, are $^{+0.08}_{-0.03}$ and ± 0.01 for lead and copper, respectively.

Energy Calibration of Scintillator Panels

The energy calibration of the scintillators was performed with the help of the simulation (see Section 5.1.2.1), using the scintillator spectra without any coincidence. However, the muon tag determination procedure selects special muons. For these muons a maximal deviation of ≈ 200 keV (towards lower energies) in the measured spectra compared to the simulated spectrum was found. This holds for all scintillators and both runs with only two exceptions. In the case of a muon tag on the left side of the setup a deviation of up to ≈ 1700 keV for the top scintillators and ≈ 1500 keV for the bot scintillator towards lower energies was observed. This huge deviation can be explained by a locally reduced light collection efficiency in the corners on the left side of the big scintillators, the side where the PMTs are located (see Section 5.2). A reduced light collection and a therefore smaller reconstructed energy can lead to unidentified muons in the experimental data sets. As a correct energy calibration was assumed for the scintillators, the observed deviations have to be investigated. This was carried out by reducing the energy cuts of the scintillators in the muon tag determination procedure ac-

cordingly to the observed values. The determined systematic uncertainties on R_S^{Exp} ($\delta R^{Exp}_{S:\,\text{energy cal.}}$), expressed in number of 10^{-5} 2.2 MeV gammas per muon tag, are $+0.03$ and -0.01 for lead and copper, respectively.

Time Stamps of Energy Depositions in Scintillators

For the determination of the muon tags in the experimental data analysis it was assumed that the time stamps of energy depositions in the scintillators are precise. However, the timing accuracy of energy depositions in the scintillators depends on different quantities. The ones dominating the precision are the time resolution of the ADC and the accuracy of the time stamp reconstruction algorithm. The time resolution of 4 ns is determined by the 250 MHz sampling rate of the ADC. For the reconstructed time stamps of energy depositions in the scintillators, a maximal variation of 5 ns was taken [125]. To investigate the influence of both quantities, the allowed maximal time difference in the muon tag determination procedure (see Section 5.2) was varied. Instead of the standard value of ± 30 ns the time window was decreased/increased by 10 ns to ± 20 ns/± 40 ns, respectively. In order to maximise the effect, all three allowed maximal time differences in the muon tag determination procedure were set simultaneously to either ± 20 ns or ± 40 ns. Changed time windows lead to different background rejection and muon identification efficiencies. The obtained systematic uncertainties on R_S^{Exp} ($\delta R^{Exp}_{S:\,\text{scint. timing}}$), expressed in number of 10^{-5} 2.2 MeV gammas per muon tag, are $+0.01$ and -0.01 for lead and copper, respectively.

Time Stamps of Energy Depositions in Germanium Detectors

In the data analysis it was assumed that the time stamps of the germanium detectors are precisely determined by the reconstruction algorithm. Precise time stamps are important for the collection of 2.2 MeV neutron capture gammas in the time window Δt^{Exp}_{S+B} (see Section 7.1) and thus for R_S^{Exp}. It was observed that the determined time stamps of energy depositions in the germanium detectors are only precise within 1 μs[1]. Note, for Δt^{Exp}_{S+B} a lower time cut of 7 μs was chosen in the analysis. Consequently, an energy deposition that occurs for example at

[1]This value was determined by analysing the distribution of time differences between coincident energy depositions > 10 MeV in the germanium detectors and energy depositions > 5 MeV in the Big top scintillator, resulting from the passage of muons through them. Note that the time stamps of energy depositions in the scintillators, as discussed beforehand, are precise within ≈ 10 ns.

6.5 μs after a muon tag might still be collected in Δt_{S+B}^{Exp}. The influence of the imprecise time stamps was investigated by decreasing/increasing the lower time cut of Δt_{S+B}^{Exp} by 1 μs to 6 μs/8 μs and repeating the analysis. The resulting systematic uncertainties on R_S^{Exp} ($\delta R_{S:\,ger.\,timing}^{Exp}$), expressed in number of 10^{-5} 2.2 MeV gammas per muon tag, are ± 0.02 for both lead and copper, respectively.

Fitting of Energy Region Around 2.2 MeV Neutron Capture Gamma Line

The influence of the applied fit function as well as the chosen fit range, used for the determination of the number of 2.2 MeV neutron capture gammas from the experimental germanium spectra (see Section 7.1), on R_S^{Exp} was investigated. Both quantities were individually studied. First, the fit range for the germanium spectra, used for the time windows Δt_{S+B}^{Exp} and Δt_{B}^{Exp}, was increased from (2217 - 2228) keV to (2215 - 2235) keV. Repeating the analysis yields the systematic uncertainties $\delta R_{S:\,fit\,range}^{Exp}$ on R_S^{Exp}. Second, the influence of the fit function that describes the stochastic background contribution was investigated. In contrast to the first order polynomial function, chosen in the standard analysis, a constant function was selected. The analysis was repeated and the systematic uncertainties $\delta R_{S:\,fit\,function}^{Exp}$ on R_S^{Exp} were obtained. The determined values for the systematic uncertainties $\delta R_{S:\,fit\,range}^{Exp}$ and $\delta R_{S:\,fit\,function}^{Exp}$ for lead, expressed in number of 10^{-5} 2.2 MeV gammas per muon tag, are $+0.04$ and -0.02. For copper both systematic uncertainties were found to be negligible.

Length and Position of Δt_{S+B}^{Exp}

The influence of the length and the position of Δt_{S+B}^{Exp} (see Section 7.1) on R_S^{Exp} was studied. First the maximal accepted time difference between a muon tag and an energy deposition in the germanium detectors was doubled from 1 ms to 2 ms. This allows to test the influence of an increased background collection on R_S^{Exp}. Furthermore, it tests if 2.2 MeV neutron captures gammas, resulting from neutrons that are correlated to the tagged muon, beyond 1 ms were missed in the standard analysis. Note, the maximum accepted time difference was not decreased, as this would lead to a significant loss of 2.2 MeV neutron capture gammas. The resulting systematic uncertainties on R_S^{Exp} ($\delta R_{S:\,time\,window}^{Exp}$), expressed in number of 10^{-5} 2.2 MeV gammas per muon tag, are $+0.04$ and -0.01 for lead and copper, respectively. Second, it was investigated if the lower time cut of Δt_{S+B}^{Exp} (7 μs in the standard analysis) rejects all prompt muon-induced back-

grounds. For this purpose, the time difference of energy depositions observed in the germanium detectors (in an energy range of 2100 keV to 2300 keV) and the previous muon tag were plotted. Afterwards, the distribution was fit with a falling exponential function. The fit yields a background contribution of $< 10^{-14}$ muon-induced prompt germanium energy depositions with energies of 2.2 MeV (energy resolution of germanium detectors is taken into account) and a timing of $> 6\,\mu$s after a muon tag. Thus, this component can be neglected.

Length and Position of Δt_B^{Exp}

In the analysis of the experimental data sets the time window Δt_B^{Exp}, used to determine the stochastic 2.2 MeV neutron capture gamma background (see Section 7.1), collects all events in the germanium detectors between 10 ms and 100 ms after each muon tag. It is assumed that the rate of stochastic 2.2 MeV neutron capture gammas is constant. To investigate the dependence of R_S^{Exp} on the chosen length and position of Δt_B^{Exp}, it was shortened and shifted at the same time. Instead of collecting all events between 10 ms and 100 ms, 100 ms and 150 ms were chosen as boundaries of the time window. The determined systematic uncertainties for lead and copper were found to be negligible.

Positioning of Scintillator Panels

The influence of an imprecise positioning of the scintillators on R_S^{Exp} was investigated. A poor alignment of the scintillators might lead to an increased or decreased identification of special muons. Such special muons could be ones that do not only pass through the target walls but also through other parts of the setup, like the plastic tank or the water. Neutrons that are produced by these muons might have a significantly higher or lower 2.2 MeV neutron capture gamma detection probability. An imprecise scintillator positioning might therefore influence R_S^{Exp}. The influence of the scintillator alignment was investigated with the help of a dedicated simulation of the MINIDEX Run 2 setup. In this simulation, the position of Small3 and Small4 were simultaneously shifted by 2 cm in x-and y-direction (see Fig. 4.2, Small3: in positive x-and y-direction, Small4: in negative x-and y-direction). This modified setup configuration was simulated and a $\approx 5\,\%$ higher muon tag rate was observed. However, no systematic uncertainty due to the shifted scintillators for R_S^{Sim} above statistical uncertainty was found. As a consequence of the simulation prediction, the systematic uncertainty for

R_S^{Exp} of lead can be also neglected. The corresponding systematic uncertainties for copper is also deduced from this investigations.

Positioning, Size and Dead Layer Thickness of Germanium Detectors

The positioning of the germanium detectors within the plastic water tank is known within a few cm. Mathematical considerations were carried out to investigate the influence of the positioning of the germanium detectors on the 2.2 MeV gamma detection efficiency. Only a small change of the efficiency was found. Consequently, no systematic uncertainty for R_S^{Exp} was considered due to the positioning of the germanium detectors.

Further, the influence of the dead layer thickness (on the n+ contact) and the size of the germanium crystals on R_S^{Exp} was investigated. The dead layer of the used germanium crystals is specified by the producer to be (1.0 ± 0.5) mm [128]. When considering the uncertainty on the dead layer thickness, the fully active volume of both germanium detectors varies by $\pm 3.0\,\%$. The uncertainty on the dimensions of the germanium crystals is given by the producer to be 0.5 mm [139]. Taking this uncertainty into account changes the fully active volume of both germanium detectors by $\pm 2.2\,\%$. A different fully active detector volume leads to a different 2.2 MeV gamma detection probability. Together with the expectation that the detection efficiency of 2.2 MeV gammas scales linearly with the fully active detector volume, the investigated detector quantities lead to relative systematic uncertainties on R_S^{Exp} of $\pm 3.0\,\%$ and $\pm 2.2\,\%$. As these values are independent of the target material, they are used for lead and copper. The corresponding values for the systematic uncertainties due to the dead layer ($\delta R^{Exp}_{S:\,\text{dead layer}}$), expressed in number of 10^{-5} 2.2 MeV gammas per muon tag, are ± 0.11 and ± 0.04 for lead and copper, respectively. Similarly, the values for the systematic uncertainties due to the germanium crystal size ($\delta R^{Exp}_{S:\,\text{cryst. size}}$), also expressed in number of 10^{-5} 2.2 MeV gammas per muon tag, are ± 0.08 and ± 0.03 for lead and copper, respectively.

Presence of an Additional Neutron Detector in the Vicinity of the Setup

For the first ≈ 6 months of MINIDEX Run 2 data taking an additional neutron detector, using gadolinium doped liquid scintillator [120], was installed next to the MINIDEX setup. The influence of the neutron detector on R_S^{Exp} was investigated. For this purpose, a dedicated simulation was performed and a MC data

set was generated. In this simulation the neutron detector was implemented next to the MINIDEX setup. The analysis of the generated MC data set showed that the presence of the additional neutron detector has no influence on R_S^{Sim}. Furthermore, the acquired experimental data set of MINIDEX Run 2 was split up into two subsets, one with and one without the neutron detector in the vicinity of the MINIDEX setup. Afterwards, both subsets were independently analysed. No difference above statistical uncertainty was found, confirming the simulation predictions. As a consequence of the simulation prediction as well as the experimental finding, the systematic uncertainty for R_S^{Exp} due to the presence of the neutron detector in the vicinity of the MINIDEX setup can be neglected.

Total Systematic Uncertainty of Experimental Data Analysis

The determined total systematic uncertainties on R_S^{Exp}, $\delta R_{S:\,total}^{Exp}$, are given in Table 8.1. In addition, all non-negligible individual contributions to $\delta R_{S:\,total}^{Exp}$ are stated. Note that the values for $\delta R_{S:\,total}^{Exp}$ result from the quadratic addition of the corresponding individual systematic uncertainties.

8.3.2 Systematic Uncertainties of the Monte Carlo Data Analysis

Different sources of systematic uncertainties of the MC data analysis on R_S^{Sim} were investigated. Compared to the experiment, in the simulation the events that are searched for can be unambiguously identified and selected. Furthermore, no quantities like detector instabilities or radioactive backgrounds have to be taken into account. As a consequence, only the following two sources of systematic uncertainties have been investigated:

- Physics list
- Density of soil in laboratory overburden

Physics List

The influence of the chosen physics list on R_S^{Sim} was investigated. In Geant4 different physics lists are recommended for the same simulation task (see Section 3.1 for details). For this purpose, the implemented MINIDEX Run 2 setup was also simulated with the Shielding physics list. The same pre-recorded muon events as for the standard simulation (see Section 6.1.1) were used as input. A MC data set

Table 8.1: Total as well as individual systematic uncertainties on R_S^{Exp} for lead and copper. The total uncertainties result from the quadratic addition of the corresponding individual uncertainties. All stated uncertainties are expressed in number of 10^{-5} 2.2 MeV gammas per muon tag.

	Lead	Copper
	$[10^{-5}]$	
$\delta R^{Exp}_{S:\,\text{total}}$	$^{+0.19}_{-0.14}$	± 0.06
$\delta R^{Exp}_{S:\,\text{energy res.}}$	$+0.07$	$+0.03$
$\delta R^{Exp}_{S:\,\text{energy recon.}}$	$^{+0.08}_{-0.03}$	± 0.01
$\delta R^{Exp}_{S:\,\text{energy cal.}}$	$+0.03$	-0.01
$\delta R^{Exp}_{S:\,\text{scint. timing}}$	$+0.01$	-0.01
$\delta R^{Exp}_{S:\,\text{ger. timing}}$	± 0.02	± 0.02
$\delta R^{Exp}_{S:\,\text{fit range}}$	$+0.04$	—
$\delta R^{Exp}_{S:\,\text{fit function}}$	-0.02	—
$\delta R^{Exp}_{S:\,\text{time window}}$	$+0.04$	-0.01
$\delta R^{Exp}_{S:\,\text{dead layer}}$	± 0.11	± 0.04
$\delta R^{Exp}_{S:\,\text{cryst. size}}$	± 0.08	± 0.03

with an effective lifetime of ≈ 68 days was generated for the implemented Run 2 setup with the Shielding physics list. The analysis of this MC data sets yielded a value of $(3.48 \pm 0.22\,(\text{stat})) \cdot 10^{-5}$ for R_S^{Sim}. This value is in agreement within statistical uncertainties with $(3.37 \pm 0.09\,(\text{stat})) \cdot 10^{-5}$, the corresponding value of R_S^{Sim} determined with the MaGe Default physics list (see Section 8.4). As a consequence, no systematic uncertainty for R_S^{Sim} of lead due to the chosen physics list was considered.

Density of Soil in Laboratory Overburden

The density of the soil in the overburden of the Tübingen underground laboratory is only known to a precision of $\approx 0.2\,\text{g}\,\text{cm}^{-3}$ (see Section 6.1.1). An increased or decreased soil density changes the propagation and interaction of the simulated muons and muon-induced particles in the laboratory overburden. The density of the soil in the overburden has thus a direct influence on the

energy and angular spectrum of the particles reaching the underground laboratory. Furthermore, it also influences the flux and composition of the incident particles. The influence of a different soil density on R_S^{Sim} was investigated. For this purpose, the implemented MINIDEX Run 2 setup was simulated two further times. The pre-recorded muon events, obtained with FLUKA for a $\pm 0.2\,g\,cm^{-3}$ increased/decreased soil density, were used as input. With the implemented MINIDEX Run 2 setup, Monte Carlo data sets with an effective lifetime of ≈ 80 days were generated with Geant4 for both cases. The effective MC lifetimes were determined by applying the normalisation procedure described in Section 6.1.5. It was found that the mean energy of tagged muons is increased/decreased by 0.2 GeV in the case of a higher/lower soil density, respectively. However, no difference above statistical uncertainty was observed for R_S^{Sim}. Therefore, no systematic uncertainty for R_S^{Sim} of lead due to the inaccurate knowledge of the soil density is taken into account.

Total Systematic Uncertainty of the Monte Carlo Data Analysis

Both investigated sources of systematic uncertainty on R_S^{Sim} of lead yielded no systematics above the statistical uncertainties. For copper the same conclusions are deduced from the discussed investigations. In order to be conservative, for lead and copper the corresponding statistical uncertainties of R_S^{Sim} are taken as total systematic uncertainties. The resulting total systematic uncertainties δR_S^{Sim}, expressed in number of 10^{-5} 2.2 MeV gammas per muon tag, are ± 0.09 and ± 0.10 for lead and copper, respectively.

8.4 Neutron Signal Rates and Neutron Signal Multiplicity Event Rates

The obtained measured and simulated neutron signal rates R_S for lead and copper, including the determined systematic uncertainties, are given in Table 8.2. The measured neutron signal rate R_S^{Exp} for lead was found to be in agreement with R_S^{Sim}, the corresponding value predicted by simulation. With these values the mismatch factor MF_S for lead was determined to be $1.04\,^{+0.10}_{-0.09}$ (combined statistical and systematical uncertainty). In contrast to the good agreement for lead the simulation overpredicts the measured neutron signal rate for copper. The observed overprediction yields a mismatch factor MF_S of 0.72 ± 0.14 for copper. In order to cross-check Geant4 predictions for lead, detailed investigations

Table 8.2: Measured and Geant4 predicted neutron signal rate R_S for lead and copper and the neutron signal multiplicity event rate R_M for lead. The given values were obtained for tagged muons with a mean kinetic energy of (8.7 ± 0.2) GeV for lead and (8.5 ± 0.2) GeV for copper at the position before they enter the setup. R_M was determined for the experimental and MC data set of MINIDEX Run 2 only.

	R_S $[10^{-5}]$ per muon tag	
	Experiment	Geant4
Lead	$3.52 \pm 0.11\,(\text{stat}) \,^{+0.19}_{-0.14}\,(\text{syst})$	$3.37 \pm 0.09\,(\text{stat}) \pm 0.09\,(\text{syst})$
Copper	$1.27 \pm 0.14\,(\text{stat}) \pm 0.06\,(\text{syst})$	$1.77 \pm 0.10\,(\text{stat}) \pm 0.10\,(\text{syst})$
	R_M $[10^{-6}]$ per muon tag	
	Experiment	Geant4
Lead	$0.19 \,^{+0.11}_{-0.09}\,(\text{stat}) \,^{+0.06}_{-0.03}\,(\text{syst})$	$1.23 \pm 0.24\,(\text{stat}) \pm 0.09\,(\text{syst})$

of muon interactions and neutron production were performed with the help of FLUKA (see Chapter 9).

In Table 8.2 also the determined neutron signal multiplicity event rates R_M^{Exp} and R_M^{Sim} for lead of MINIDEX Run 2 are presented. For R_M^{Exp} the same sources of systematic uncertainties apply as for R_S^{Exp}. In addition, the influence of the uncertainty of the germanium detector dead time ($(20.3 \pm 0.1)\,\mu$s, see Section 4.3.3) on R_M^{Exp} was investigated. Neutron signal multiplicity events, for which two 2.2 MeV gammas are detected in the same germanium detector, are affected by this uncertainty. However, variations of the dead time within the uncertainties show that the resulting systematical uncertainty on R_M^{Exp} is by at least two orders of magnitude lower than the statistical uncertainty. As a consequence, for R_M^{Exp} only the squared (conservative approach to account for the double 2.2 MeV neutron capture gammas) total systematic uncertainty of R_S^{Exp} (in percentage terms) was taken. Furthermore, the same sources of systematic uncertainties as for R_S^{Sim} apply for R_M^{Sim}. The corresponding squared total systematic uncertainty of R_S^{Sim} (in percentage terms) was therefore taken as the systematic uncertainty for R_M^{Sim}. A significant overprediction of the measured neutron signal multiplicity event rate by a factor of $6.5 \,^{+4.0}_{-3.3}\,(\text{stat}) \,^{+2.1}_{-1.1}\,(\text{syst})$ was determined for the simulation. In addition, two neutron signal multiplicity events with three 2.2 MeV neutron capture gammas for the same muon tag were found in the MC data set, while in the experimental data set no such event was observed. In Section 6.3 it was shown that R_M^{Sim} for lead strongly depends on the muon-nuclear neutron

multiplicity. The overprediction of neutron signal multiplicity events by the simulation therefore hints towards a too high muon-nuclear neutron multiplicity. A further hint for an imprecise description of the muon-nuclear neutron multiplicity by the simulation is given in Section 9.1.

8.5 External Neutron Yield

With the obtained values of Y_{Ext}^{Sim} (see Section 6.4), the external neutron yield predicted by simulation, and the beforehand determined mismatch factor MF_S (see Section 8.4) the external neutron yield Y_{Ext} for lead and copper was calculated with Eq. (3.2). The results are given in Table 8.3. Y_{Ext} for lead was

Table 8.3: External neutron yield Y_{Ext} for lead and copper in MINIDEX, determined with Eq. (3.2). The values for the external neutron yield predicted by simulation Y_{Ext}^{Sim} (see Section 6.4) and the mismatch factor MF_S (see Section 8.4) are given as well. The stated uncertainties are the total ones except for Y_{Ext}^{Sim} for which only statistical uncertainties are given.

	Lead	Copper
Y_{Ext} $[10^{-5}\,g^{-1}\,cm^2]$ neutrons per muon tag	$7.2\,^{+0.7}_{-0.6}$	2.1 ± 0.4
Y_{Ext}^{Sim} $[10^{-5}\,g^{-1}\,cm^2]$ neutrons per muon tag	6.96 ± 0.02	2.93 ± 0.02
MF_S	$1.04\,^{+0.10}_{-0.09}$	0.72 ± 0.14

found to be by a factor of $3.4\,^{+0.8}_{-0.7}$ higher than for copper. In Fig. 8.1 the kinetic energy spectra of the neutrons emitted from the selected lead and copper surfaces are depicted. These spectra were obtained by scaling the simulated spectra (see Section 6.4) with the corresponding value of MF_S. It is apparent that for nearly all energies the number of emitted neutrons from the lead surface is higher than the number of neutrons leaving the copper surface. Only for energies at a few tens of keV and above a few hundreds of MeV the number of emitted neutrons is similar. The predicted mean kinetic energy of the neutrons leaving the lead and copper surface is (4.9 ± 0.2) MeV and (8.9 ± 0.3) MeV, respectively. The corresponding angular distributions of the emitted neutrons, which are independent of the scaling with MF_S, are the simulated ones shown in Section 6.4.

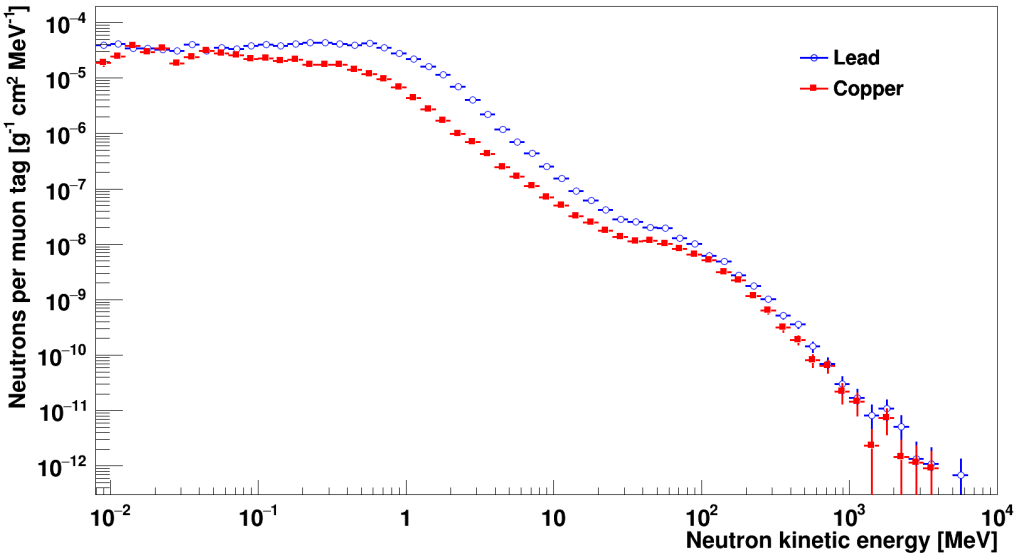

Figure 8.1: Simulated kinetic energy spectra of muon-induced neutrons leaving the lead and copper surfaces perpendicular to the x-axis (see Fig. 6.13). Only events with a muon tag are considered. In order to take discrepancies between measured and simulated observable into account, the simulated spectra were scaled with the corresponding mismatch factor MF_S. The depicted neutrons were predominantly produced by muons and muon-induced particles in the target walls of the MINIDEX Run 3 setup. The simulated muons have a mean energy of (8.7 ± 0.2) GeV for lead and (8.5 ± 0.2) GeV for copper at the position before they enter the target walls. The simulated neutrons emitted from the lead and copper surface are predicted to have a mean energy of (4.9 ± 0.2) MeV and (8.9 ± 0.3) MeV, respectively. The given uncertainties are partially smaller than the size of the marker and are statistical only.

Note that the applied scaling procedure scales all neutrons, independent of the precise or imprecise description of the individual neutron production processes in the simulation. The study in Chapter 9 and the discussed findings of recent publications (see Section 3.3) indicate that the Geant4 simulated neutron production processes in MINIDEX Run 2 are imprecise. Together with a significantly energy dependent neutron detection efficiency in MINIDEX (see Section 6.5.2), this leads to the introduction of systematic uncertainties on the external neutron yield which are very difficult to assess. Consequently, the stated external neutron yields for lead and copper should be treated carefully.

The determined external neutron yield for lead is by a factor $3.5\,^{+2.8}_{-1.8}$ lower than the value predicted by the fit (fit of external neutron yields versus the corresponding mean muon energy) that was carried out in [72] and discussed in Section 3.2.2. However, due to the discussed deficiencies of the neutron yield (see

also Section 3.2.1, Section 6.4 and Section 6.5) no conclusive feedback can be drawn. For copper, due to the lack of experimental data sets of muon-induced neutrons, no fit of the correlation between the external neutron yield and the mean muon energy is available for comparison.

Chapter 9

Geant4 and FLUKA Predictions for Muon-Induced Neutron Production in Lead

In the following, a detailed comparison of Geant4 and FLUKA predicted muon interactions and neutron production in the lead target walls of the MINIDEX Run 2 setup is presented. Note that large parts of this chapter are taken from [94] and that all presented FLUKA simulations within this chapter were carried out separately [2].

A simulation of the Run 2 setup, making use of the same pre-recorded muon events (see Section 6.1.1), was carried out with the FLUKA Monte Carlo program. The FLUKA predicted neutron signal rate R_S^{Sim} is $(3.60 \pm 0.13\,(\text{stat})) \cdot 10^{-5}$ and agrees well, both with the experimental neutron signal rate R_S^{Exp} and the value for R_S^{Sim} obtained with Geant4.

Despite the agreement, a more detailed comparison of simulation predictions for the muon-induced neutron production in lead by the two programs was carried out. This comparison is motivated by recent publications [116, 118] (see Section 3.3), pointing out discrepancies between Geant4 predictions and experimental findings for the neutron production by photo-nuclear inelastic scattering reactions in high-Z materials (tungsten, gold and lead). At the same time, FLUKA predictions were reported to describe experimental observations reasonably well.

Only muon interactions inside the lead target walls for events with a muon tag were selected for this study. The predictions for the muon interactions and the resulting secondary particles are compared in Section 9.1. All neutrons generated as a consequence of the initial muon interactions in the lead target walls were recorded at the point of their creation and removed from the simulation. The

effects of neutron transport and re-interactions are excluded by this approach. These first generation neutrons are produced almost exclusively by photo-nuclear and muon-nuclear reactions for both simulation programs. Findings for the first generation neutrons from the Geant4 and FLUKA simulations are presented in Section 9.2. The recorded first generation neutrons were then used as input to Geant4 and FLUKA simulations of the MINIDEX Run 2 setup, in the last step of the comparison. The contribution of the first generation neutrons to the neutron signal rate R_S^{Sim} for Geant4 and FLUKA is discussed in Section 9.3.

9.1 Muon Interactions

At first, only secondaries, defined as particles produced directly by muons inside the lead target walls, were analysed. The four main processes by which muons lose energy during their passage through matter (see Section 2.1.2) are: bremsstrahlung, electron-positron pair production, ionisation (i.e. muon-electron scattering) and muon-nuclear reactions. The energy spectra of secondaries generated by muons for the first three processes, i.e. electrons, positrons and photons, are depicted in Fig. 9.1(a)[1]. Note, most plots throughout Chapter 9 show lethargy [140]. Good agreement for the Geant4 and FLUKA predicted distributions is found with only small deviations for secondaries at energies above a few GeV. In Fig. 9.1(b) the energy spectra of the most frequently produced secondaries for muon-nuclear reactions are compared. The main features of the distributions are similar while for energies above a few hundred MeV there are significant deviations in the predictions for the production rates of the individual secondaries. In Table 9.1 the production rates of secondaries, generated in muon-nuclear reactions, for energies above and below 20 MeV are given for both simulation tools. It can be seen that FLUKA and Geant4 predictions differ significantly, depending on the particle type and energy range. This is especially apparent for the predicted rate of gammas with energies $> 20\,\text{MeV}$.

In Fig. 9.2 the muon-nuclear neutron multiplicity (see Section 6.3.2) is shown. A mean muon-nuclear neutron multiplicity of 13.19 ± 0.05 and 10.98 ± 0.05 was found for Geant4 and FLUKA, respectively. The total rate of muon-nuclear reactions in Geant4 and FLUKA was determined to be $(158.0 \pm 0.9) \cdot 10^{-5}$ and $(153.3 \pm 1.0) \cdot 10^{-5}$. While the total rate is similar, especially for muon-nuclear

[1] Only electrons, positrons and gammas with energies $> 8\,\text{MeV}$ are shown. The reason is that if the energy of the secondaries falls below $\approx 8\,\text{MeV}$ only a negligible number of neutrons are produced within lead. This energy threshold for the neutron production was determined independently for Geant4 and FLUKA.

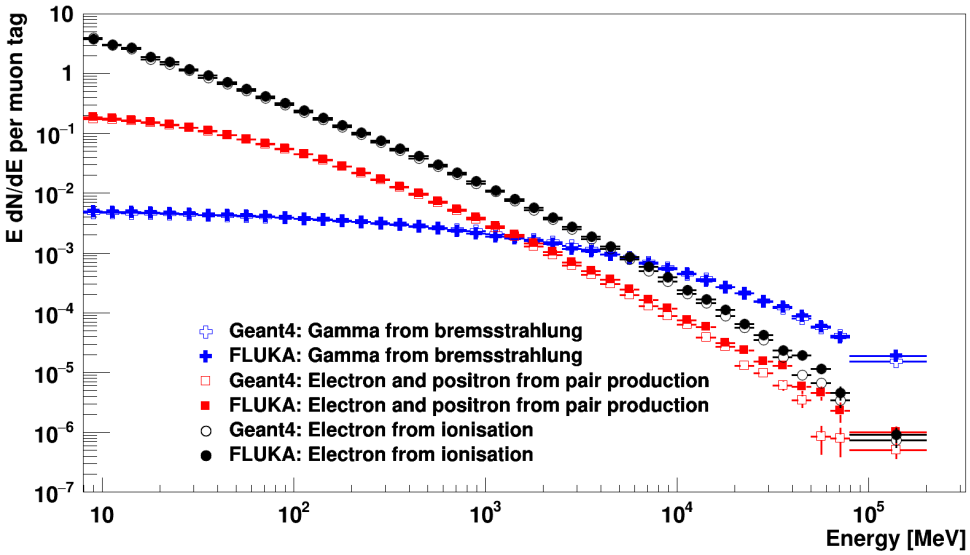

(a)

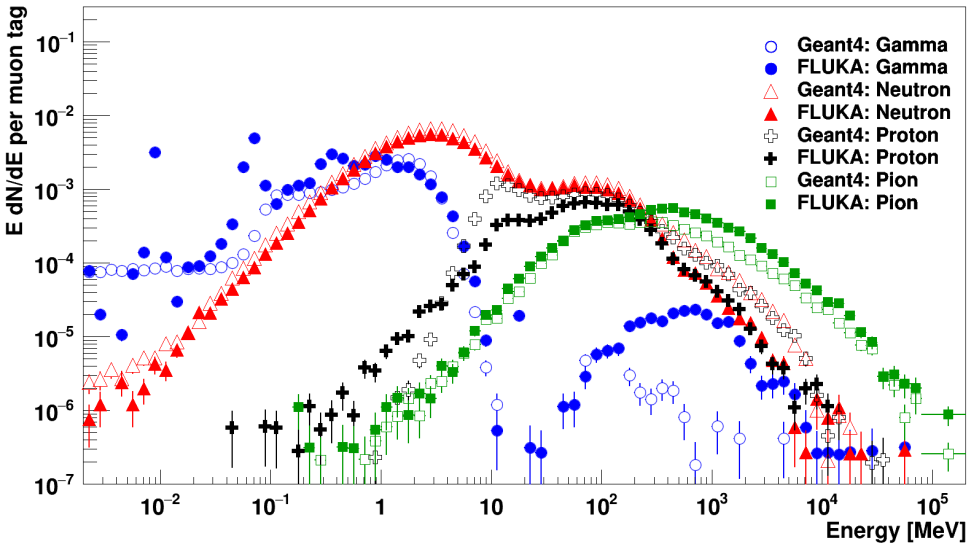

(b)

Figure 9.1: Differential energy spectra of secondaries multiplied by energy (E). The secondaries were generated by tagged muons in the lead target walls of the MINIDEX Run 2 setup. The spectra obtained with Geant4 and FLUKA are displayed by open and filled markers, respectively. In (a) the secondaries from bremsstrahlung (blue), electron-positron pair production (electrons and positrons are plotted together, red) and ionisation (black) are depicted. In (b) gammas (blue), neutrons (red), protons (black) and pions (green) generated by muon-nuclear reactions are shown. In Table 9.1 the production rate of secondaries, generated in muon-nuclear reactions, are presented. Assigned uncertainties are partially smaller than the size of the marker and are statistical only.

Table 9.1: Most frequently produced secondaries predicted by Geant4 and FLUKA in muon-nuclear reactions within the lead target walls of MINIDEX Run 2. The rates for Geant4 and FLUKA are expressed in number of 10^{-5} secondaries per muon tag. In addition, the ratios between the FLUKA and Geant4 predicted rate of secondaries are given. The stated uncertainties are statistical only.

	Geant4	FLUKA	Ratio
	$[10^{-5}]$ per muon tag		
Gamma ≤ 20 MeV	577.0 ± 1.6	964.5 ± 2.5	1.67 ± 0.01
Gamma > 20 MeV	0.39 ± 0.04	5.30 ± 0.19	13.6 ± 1.5
Neutron ≤ 20 MeV	1697.9 ± 2.8	1418.1 ± 3.0	0.84 ± 0.01
Neutron > 20 MeV	306.9 ± 1.2	265.8 ± 1.3	0.87 ± 0.01
Proton ≤ 20 MeV	109.6 ± 0.7	31.1 ± 0.5	0.28 ± 0.01
Proton > 20 MeV	227.5 ± 1.0	155.6 ± 1.0	0.68 ± 0.01
Pion ≤ 20 MeV	3.13 ± 0.12	4.19 ± 0.17	1.34 ± 0.07
Pion > 20 MeV	129.3 ± 0.8	182.8 ± 1.1	1.41 ± 0.01

reactions with high neutron multiplicities large discrepancies are found. Note that for the used version of FLUKA the rate of muon-nuclear reactions with low neutron multiplicities is likely to be underpredicted [115].

9.2 First Generation Neutron Production

In a second step, all muon-induced neutrons were recorded at the position of their creation and subsequently removed from the simulation. These neutrons, called first generation neutrons in the following, were either produced directly by a muon (i.e. in muon-nuclear reactions) or indirectly by any muon-induced particle (except neutrons). Hence, neutron transport and neutron re-interactions were excluded by this approach. Only neutrons that were generated in the lead target walls were selected and compared between Geant4 and FLUKA. In Fig. 9.3 the resulting energy spectra of the first generation neutrons of the four investigated muon interactions are depicted. For Geant4 the indirectly produced neutrons account for $(42.44 \pm 0.12)\,\%$ of the total rate of first generation neutrons from muon-nuclear reactions whereas for FLUKA a value of $(36.24 \pm 0.15)\,\%$ was found. It is evident from Fig. 9.3 that the mean energy of first generation neutrons pre-

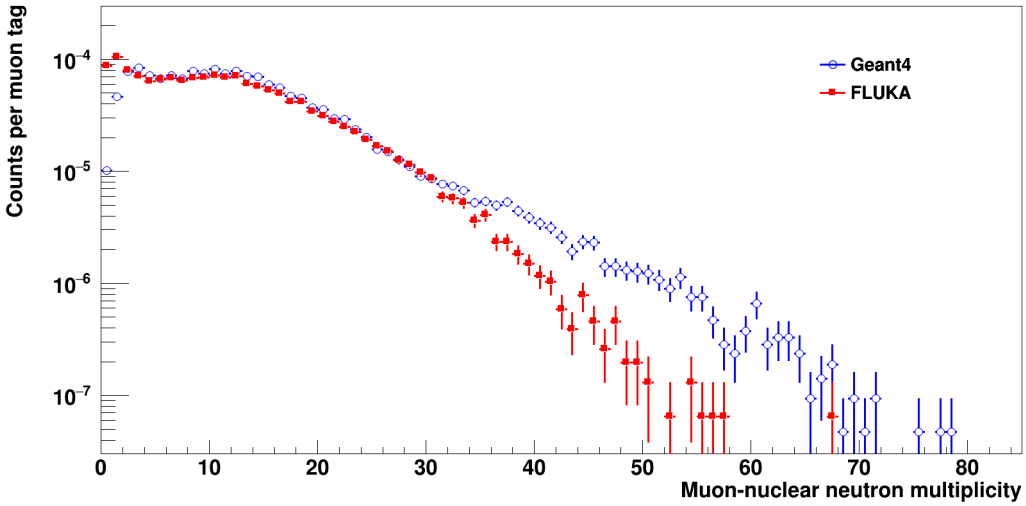

Figure 9.2: Multiplicity of neutrons produced directly by muons in muon-nuclear reactions. Only reactions that occurred in the lead target walls of the MINIDEX Run 2 setup for events with a muon tag are included. The distributions obtained with Geant4 and FLUKA are represented by open and filled markers, respectively. The maximum observed number of muon-nuclear reactions within the same muon tag for Geant4 and FLUKA is one. The mean muon-nuclear neutron multiplicity predicted by Geant4 and FLUKA is 13.19 ± 0.05 and 10.98 ± 0.05, respectively. Assigned uncertainties are partially smaller than the size of the marker and are statistical only.

dicted by Geant4 and FLUKA for each of the four investigated muon interactions is inconsistent. For muon-nuclear reactions a value of $\approx 25\,\text{MeV}$ and $\approx 20\,\text{MeV}$ was obtained for Geant4 and FLUKA, respectively, whereas for the other muon interactions deviating values between 1.5 MeV and 5 MeV were determined. In Table 9.2 the rate of first generation neutrons per muon tag for energies above and below 20 MeV are presented for Geant4 and FLUKA for the different muon interactions. The rate of first generation neutrons predicted by Geant4 for muon-nuclear reactions is higher by $(31.89 \pm 0.26)\,\%$ than the corresponding rate from FLUKA. The Geant4 predicted combined rate of first generation neutrons from the other three muon interaction processes is smaller than the FLUKA predicted rate by $(51.41 \pm 0.10)\,\%$.

Furthermore, by studying the processes leading to the production of first generation neutrons in the case of ionisation, pair production and bremsstrahlung, it was found that for Geant4 and FLUKA $> 94\,\%$ of these neutrons are produced in photo-nuclear reactions. This means that in the case of ionisation and pair production the electrons and positrons in general do not generate neutrons directly.

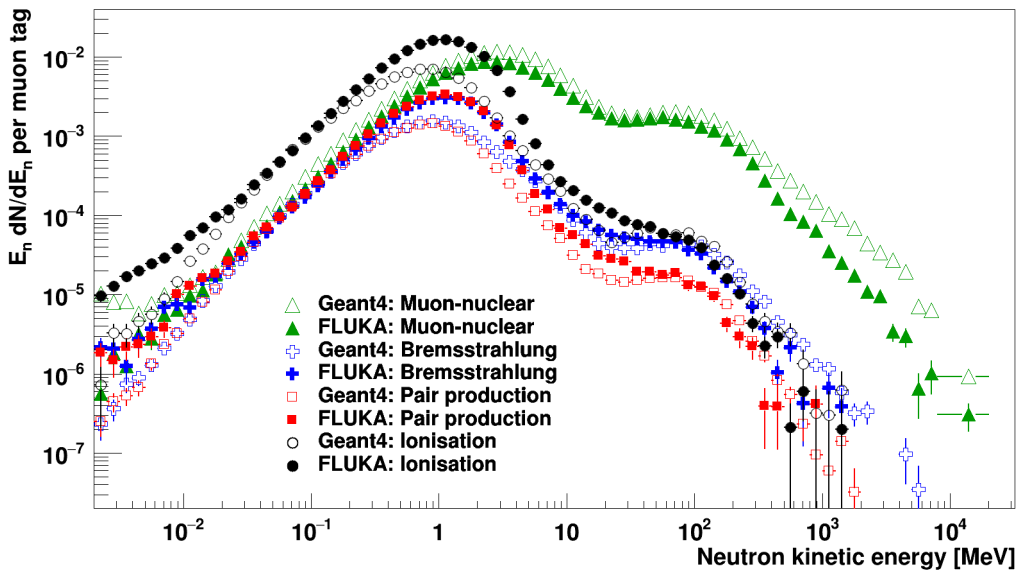

Figure 9.3: Differential kinetic energy spectra of first generation neutrons multiplied by kinetic energy (E_n). Only first generation neutrons that were generated in the lead target walls of the MINIDEX Run 2 setup are included. The kinetic energy spectra predicted by Geant4 and FLUKA are displayed by open and filled markers, respectively. The first generation neutrons for the four investigated muon interaction processes are displayed. The assigned uncertainties are partially smaller than the size of the marker and are statistical only. In Table 9.2 the rate of first generation neutrons for the four muon interactions processes are presented.

Typically the electrons and positrons lead to the generation of photons which then interact inelastically with nuclei and produce neutrons. As an example, for ionisation in Fig. 9.4 the contribution of photo-nuclear reactions to the production of the first generation neutrons is shown. It is apparent that for both MC tools the vast majority of first generation neutrons from ionisation results from photo-nuclear reactions. However, the contribution of photo-nuclear reactions to the production of first generation neutrons decreases with an increasing kinetic energy of the neutrons. In the depicted case the first generation neutrons from photo-nuclear processes make up for $(99.59 \pm 0.17)\,\%$ and $(98.64 \pm 0.30)\,\%$ of all first generation neutrons for Geant4 and FLUKA, respectively.

Table 9.2: Rate of first generation neutrons predicted by Geant4 and FLUKA for the four investigated muon interaction processes in the lead target walls of MINIDEX Run 2. The rates for Geant4 and FLUKA are expressed in number of 10^{-5} first generation neutrons per muon tag. In addition, the ratios between the FLUKA and Geant4 predictions are given. All stated uncertainties are statistical only.

	Geant4	FLUKA	Ratio
	$[10^{-5}]$ per muon tag		
Muon-nuclear $\leq 20\,\mathrm{MeV}$	2991 ± 5	2256.4 ± 3.3	0.75 ± 0.01
Muon-nuclear $> 20\,\mathrm{MeV}$	491.8 ± 1.9	384.4 ± 1.4	0.78 ± 0.01
Bremsstrahlung $\leq 20\,\mathrm{MeV}$	382.2 ± 1.7	649.4 ± 1.8	1.70 ± 0.01
Bremsstrahlung $> 20\,\mathrm{MeV}$	10.13 ± 0.28	9.86 ± 0.22	0.97 ± 0.03
Pair production $\leq 20\,\mathrm{MeV}$	324.7 ± 1.6	677.5 ± 1.8	2.09 ± 0.01
Pair production $> 20\,\mathrm{MeV}$	3.43 ± 0.16	4.03 ± 0.14	1.17 ± 0.07
Ionisation $\leq 20\,\mathrm{MeV}$	1578.9 ± 3.5	3403 ± 4	2.16 ± 0.01
Ionisation $> 20\,\mathrm{MeV}$	12.81 ± 0.31	14.00 ± 0.26	1.09 ± 0.03

9.3 Neutron Signal Rate Contribution

Finally, all first generation neutrons recorded in the previous step were simulated in Geant4 and FLUKA in order to determine the individual contributions of the four investigated muon interactions to the predicted neutron signal rate of the full simulation R_S^{Sim}. In this case neutron transport and neutron re-interactions are considered. In order to obtain a high statistic, the first generation neutrons were simulated multiple times. In Table 9.3 the resulting contributions are given together with R_S^{Sim}. The sum of detected 2.2 MeV gammas resulting from all first generation neutrons corresponds to $(65.2 \pm 1.8)\,\%$ and $(66.5 \pm 2.5)\,\%$ of R_S^{Sim} for Geant4 and FLUKA, respectively. The remaining approximately one third of 2.2 MeV gammas result for example from neutrons produced as a consequence of muon interactions outside the target walls. While the fractions agree well, the contributions of the first generation neutrons from the individual muon interaction processes do not agree. In Geant4 the first generation neutrons from muon-nuclear reactions lead to $(47.1 \pm 1.3)\,\%$ of R_S^{Sim} while the first generation neutrons from the other three muon interaction processes contribute only $(18.1 \pm 0.5)\,\%$. In comparison, the first generation neutrons from muon-nuclear reactions in FLUKA

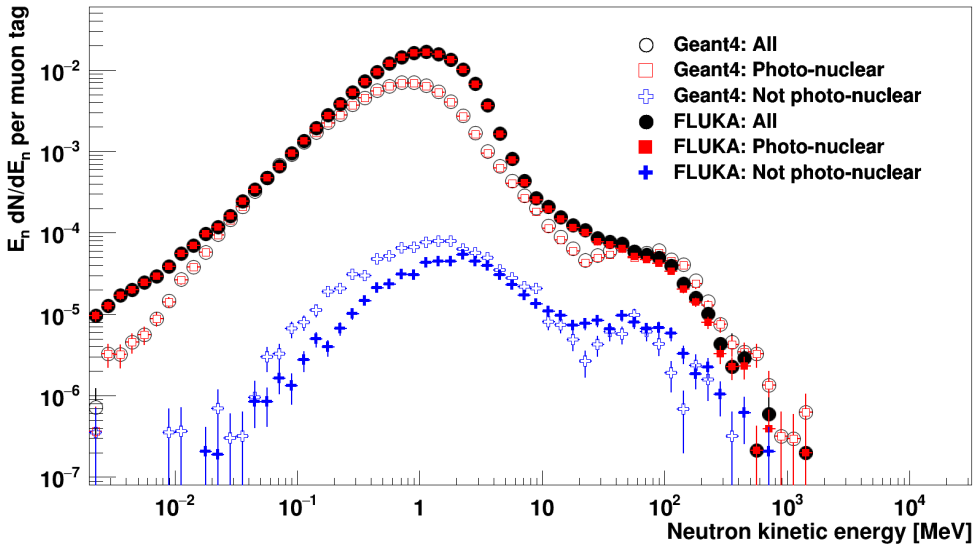

Figure 9.4: Differential kinetic energy spectra of first generation neutrons from ionisation multiplied by kinetic energy (E_n). Only first generation neutrons that were generated in the lead target walls of the MINIDEX Run 2 setup are considered. The kinetic energy spectra predicted by Geant4 and FLUKA are displayed by open and filled markers, respectively. In black all first generation neutrons from ionisation are displayed while in red the subsets of first generation neutrons produced in photo-nuclear reactions are shown. The blue spectra depict the remaining first generation neutrons from ionisation that were generated in any other inelastic scattering reaction (e.g. electron-nuclear inelastic scattering). The assigned uncertainties are partially smaller than the size of the marker and are statistical only.

lead to $(30.4 \pm 1.2)\,\%$ of R_S^{Sim}, while the first generation neutrons from the other three muon interaction processes make up for $(36.1 \pm 1.4)\,\%$.

9.4 Conclusion of Geant4 and FLUKA Comparison Study

The presented Geant4 and FLUKA simulation study together with recent publications (see Section 3.3) and the agreement of FLUKA with the measurement indicate that Geant4, when used with Geant4 recommended or standard physics lists (see Section 3.1), significantly underpredicts the neutron production in lead by photo-nuclear reactions for muon energies at shallow depths. Since Geant4 at the same time does reproduce the measured neutron signal rate R_S^{Exp}, it may imply that the neutron production in muon-nuclear reactions is significantly over-

Table 9.3: Contributions of the first generation neutrons in lead from the different muon interaction processes to the neutron signal rate of the full simulation R_S^{Sim} in Geant4 and FLUKA. All presented rates are expressed in number of 10^{-5} neutron signals per muon tag. The given uncertainties are statistical only.

	Geant4	FLUKA
	$[10^{-5}]$ per muon tag	
R_S^{Sim}	3.37 ± 0.09	3.60 ± 0.13
First generation neutrons	2.198 ± 0.013	2.393 ± 0.021
Muon-nuclear	1.588 ± 0.011	1.093 ± 0.014
Bremsstrahlung	0.109 ± 0.001	0.194 ± 0.006
Pair production	0.086 ± 0.001	0.187 ± 0.006
Ionisation	0.415 ± 0.006	0.919 ± 0.013

predicted by Geant4. However, an inaccurate treatment of the transport and interactions of hadrons by Geant4, which depends on the chosen physics list, could also contribute. The observed difference of high muon-nuclear neutron multiplicities between Geant4 and FLUKA is in agreement with the findings of Section 8.4. The presented simulation study therefore strengthens the hints for an imprecise description of the muon-nuclear neutron multiplicity in Geant4.

Chapter 10

Muon Capture on Lead

In Run 4 of the MINIDEX project the neutron production induced by muon capture on lead was studied. This was carried out by comparing experimental findings to simulation predictions. The muon capture study was carried out in the context of a master thesis [126], where a more detailed description of the performed study can be found. In the following, a brief overview of the investigations is given. Explicitly speaking, the dedicated setup, the acquired data sets, the experimental signature, the MC simulations, the analysis strategies as well as the obtained results and conclusions are presented.

10.1 Setup and Working Principle

In order to measure neutrons induced by muon captures on lead with MINIDEX, a few modifications of the setup from the previous run (Run 3, see Fig. 4.1) had to be made. The copper on the left side of the setup was exchanged with lead. Further, the two small scintillators on top of the target as well as the two small scintillators below were removed. Two new scintillators, called telescope scintillators in the following, were placed on top of the setup to form a "muon telescope". Muons that pass through the muon telescope and stop within the setup can be identified. The signature of a stopped muon are coincident signals in both telescope scintillators as well as the Big top scintillator, while no signal is observed in the Big bot scintillator. The telescope scintillators are 2.1 cm thick and have a size of 12.0 cm × 22.5 cm. They are made out of BC-408 (polyvinyl-toluene: $C_{10}H_{11}$). The two scintillators of the muon telescope are separated by blocks of styrofoam.

The structure of the muon capture setup is depicted in Fig. 10.1(a). Here, only the positions of the telescope scintillators, which are centred on top of the target, are displayed. All other parts of the setup are located exactly at the same

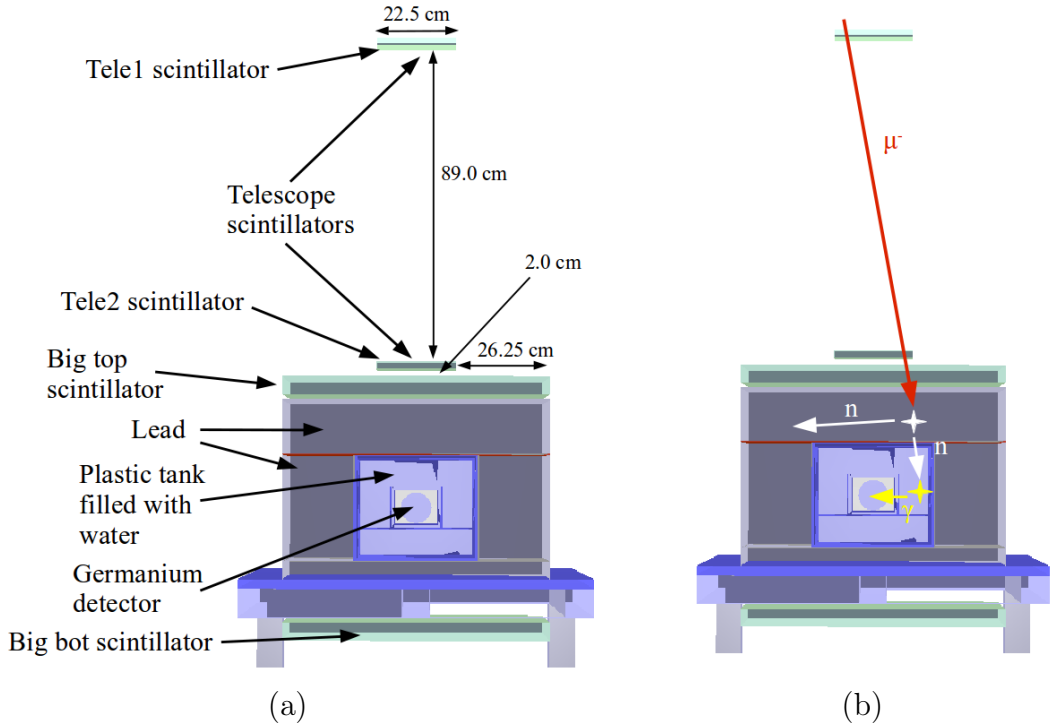

Figure 10.1: Illustration of the muon capture setup in (a). Only the positions of the telescope scintillators, which are centred on top of the target, are given. All other parts of the setup are located at the same position as in Run 2 and Run 3 (see Section 4.1). In (b) the working principle of the setup is depicted. A negatively charged muon (μ) that stops within the setup can get captured on a lead nucleus within the target. Following this capture, neutrons (n) can get emitted. If one of these neutrons reaches the water tank, it can get thermalised and captured on hydrogen afterwards. The excited deuterium nucleus emits a 2.2 MeV neutron capture gamma (γ) which can be detected by one of the two installed high-purity germanium detectors.

position as in Run 2 and Run 3 (see Section 4.1). In Fig. 10.1(b) the working principle of the measurement of muon-induced neutrons, originating from muon capture on lead, is schematically illustrated: Muons (μ) that stop within the setup are identified with the help of the four installed scintillators. Negatively charged muons at rest can get captured on lead nuclei within the target. Subsequently to this capture, the de-excitation of the nuclei can lead to the emission of neutrons (n). If these neutrons reach the water tank, they can get thermalised and captured on hydrogen afterwards. Within nanoseconds after this capture a 2.2 MeV gamma is released by the excited nucleus. This gamma can be detected by one of the two installed high-purity germanium detectors.

In order to select only muons that stop within the setup, a minimal distance between the two telescope scintillators is required. The extrapolation of all muon

paths through both telescope scintillators is required to pass through the Big bot scintillator as well. The minimum distance satisfying this requirement is 63.5 cm. In order to cope with inaccuracies due to possible imprecise scintillator alignments, the distance was enlarged to 89 cm. A picture of the fully assembled muon capture setup can be seen in Fig. 10.2. The whole setup (including the

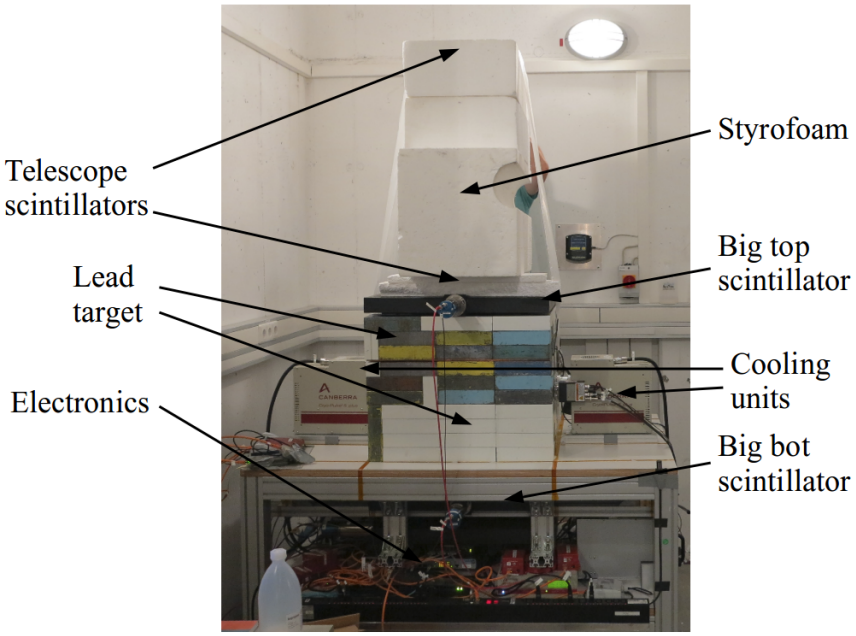

Figure 10.2: Picture of the fully assembled MINIDEX muon capture setup. The two telescope scintillators are hidden by the styrofoam blocks whereas the Big bot scintillator is nearly fully covered by the tabletop.

support structure) has a footprint of $\approx 1\,\mathrm{m}^2$ and a height of $\approx 2.5\,\mathrm{m}$.

10.2 Experimental Data Analysis

During the runtime of the muon capture measurement from September 2017 to April 2018, called MINIDEX Run 4, a data set corresponding to a lifetime of 158.83 days was acquired. The detection of muon-induced neutrons is centred around the measurement of 2.2 MeV neutron capture gammas that follow a tagged muon. The experimental analysis strategy is presented in the following.

10.2.1 Muon Capture Tag

In order to measure muon-induced neutrons originating from muon capture on lead, muons that stop inside the setup have to be identified. This is achieved by requesting energy depositions above individual energy cuts within ± 30 ns in all three scintillators on top of the target. At the same time it is required that no energy above a corresponding energy cut is deposited in the Big bot scintillator within ± 30 ns. All four scintillators were calibrated with the help of the muon spectra obtained by simulation. This was carried out by setting the position of the most probable value of the Landau distribution for each scintillator to the corresponding value predicted by simulation (≈ 10 MeV for the big scintillators and ≈ 4.5 MeV for the telescope scintillators). The used energy cuts of the muon capture tag determination procedure are given in Table 10.1.

Table 10.1: Energy cuts of the four MINIDEX muon capture setup scintillators, applied in the muon capture tag determination procedure. The energy cuts are used to discriminate muons that pass through the scintillators from energy depositions induced by backgrounds.

	Tele1	Tele2	Big top	Big bot
Energy cut [MeV]	3.1	2.8	6.9	6.5

In Fig. 10.3 the energy spectrum obtained with the Tele1 scintillator for all events with a muon capture tag is depicted. The peak of the Landau distribution is located at an energy of ≈ 4.5 MeV. The corresponding spectrum obtained with the Tele2 scintillator looks similar. A total number of 201747 muon capture tags have been identified in the experimental data set.

10.2.2 Determination of Measured Muon Capture Induced Neutron Signals

The signature of a muon capture induced neutron signal is the full energy deposition of a 2.2 MeV gamma (from neutron capture on hydrogen) in the germanium detectors within a short time after a muon capture tag. These neutron captures do not originate solely from neutrons induced by muon captures on lead, but result also from other muon-induced neutron production processes. This is discussed in detail in Section 10.3.4. Different kinds of backgrounds, like neutrons and gammas from radioactivity as well as neutrons induced by muons that did

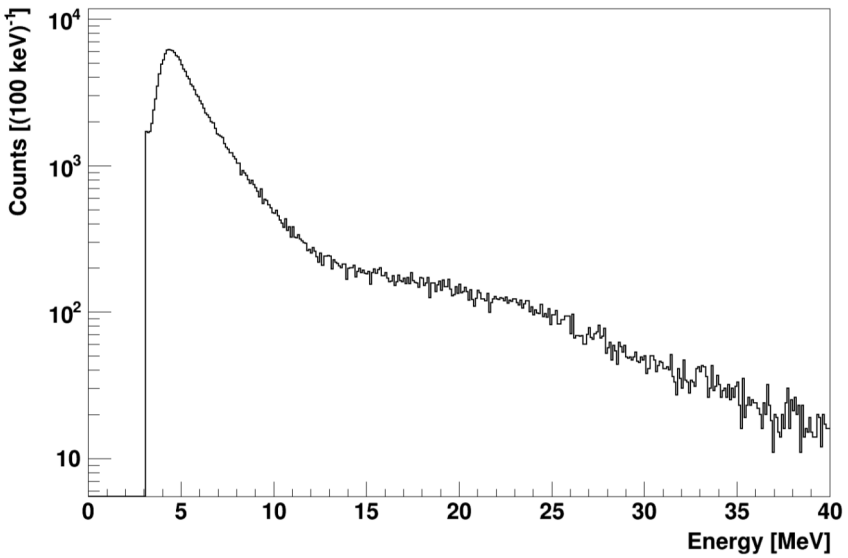

Figure 10.3: Measured energy spectrum of the Tele1 scintillator for all identified muon capture tags. Taken from [126].

not generate a muon capture tag, are present. In order to determine the number of muon capture induced neutron signals, the background contributions have to be determined. To collect the signal, like for Run 2 and Run 3 (see Section 7.1) a signal time window (ΔT^{Exp}_{S+B}) is opened from 7 μs to 1 ms after each muon capture tag. Within this time window muon capture induced neutron signals as well as energy depositions from background sources are collected. The lower as well as the higher time limit of ΔT^{Exp}_{S+B} was chosen to avoid backgrounds. A second time window, the background time window ΔT^{Exp}_{B}, is opened after the muon capture tags. This time window is located from 10 ms to 100 ms after the muon capture tags and collects uncorrelated background events only (i.e. events with no correlation to a muon capture tag). Note, if a second muon capture tag occurs within less than 100 ms, the length of ΔT^{Exp}_{B} is adjusted accordingly.

The obtained germanium spectrum for ΔT^{Exp}_{S+B} from the measurement is shown in blue in Fig. 10.4. It represents an effective measurement time of 198.4 s. The peak from the 2.2 MeV neutron capture gammas is clearly visible. Furthermore, some energy depositions from backgrounds can be seen in the vicinity of the 2.2 MeV gamma peak. In order to determine the number of muon capture induced neutron signals from this spectrum, a region of interest (ROI) that fully encloses the 2.2 MeV gamma peak is defined. It is 10.7 keV wide (corresponding to the $\pm 5\,\sigma$ energy resolution of the germanium detectors at 2.2 MeV) and ranges

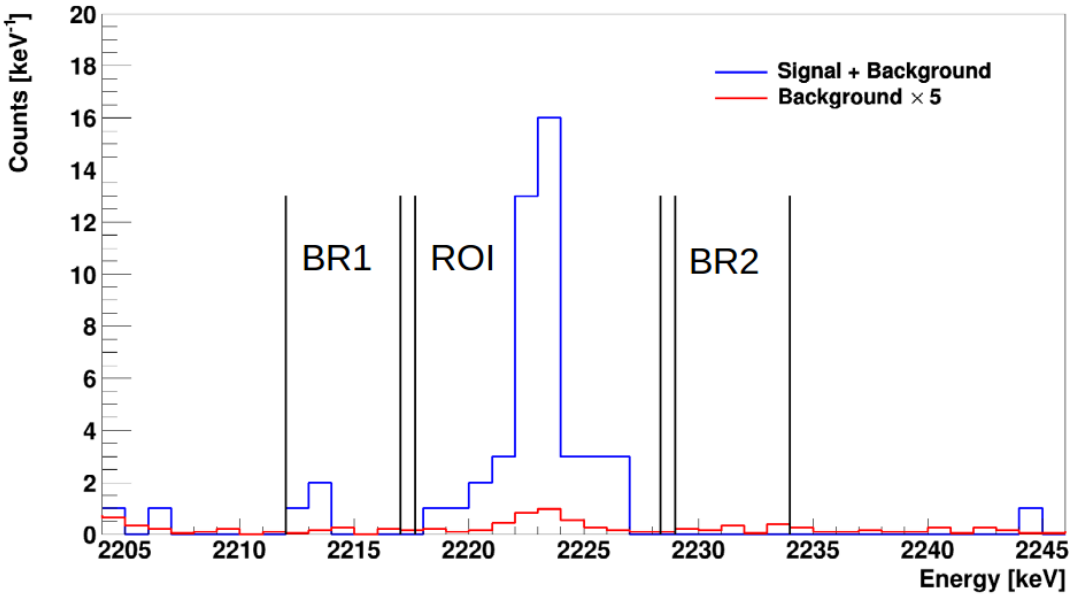

Figure 10.4: Measured energy spectra of events recorded within the two time windows that are used to determine the muon capture induced neutron signals. In blue the spectrum for the signal time window ΔT_{S+B}^{Exp} is shown. It represents an effective measurement time of 198.4 s. The Region of Interest (ROI) as well as two regions on the side of the 2.2 MeV gamma peak (BR1 and BR2), used to determine specific background contributions, are given as well. Further, the spectrum for the background time window ΔT_{B}^{Exp} is depicted in red. It represents an effective measurement time of 4.99 h and is scaled to 198.4 s, the effective measurement time of ΔT_{S+B}^{Exp}. Note, for visibility reasons, the red spectrum is scaled up by a factor of 5. See text for details.

from 2217.65 keV to 2228.35 keV. In the ROI a total number of 45 events have been identified. The background in the ROI has two components.

The first component are events in the ROI which are not correlated to a neutron capture on hydrogen. This component can be determined with the help of events in control regions on the side of the 2.2 MeV gamma peak and under the assumption of a constant background. These regions are indicated in Fig. 10.4 by BR1 and BR2. A contribution of $2.9\,^{+2.5}_{-1.2}$ background events to the ROI was determined for this component.

The second component arises due to stochastic 2.2 MeV neutron capture gamma background events. The rate of these events is expected to be constant over the whole measurement period. This background component is assessed with the help of the spectrum for ΔT_{B}^{Exp}, which is depicted in red in Fig. 10.4. It represents an effective measurement time of 4.99 h and is scaled to 198.4 s, the effective measurement time of ΔT_{S+B}^{Exp}. Using the same energy regions (ROI,

BR1 and BR2) as for ΔT^{Exp}_{S+B} yields a contribution of 0.4 ± 0.1 2.2 MeV neutron capture gamma background events.

The final number of muon capture induced neutron signals, determined for the experimental data set, is 42^{+8}_{-6}.

10.3 Monte Carlo Simulations and Monte Carlo Data Analysis

All simulations in the context of the MINIDEX muon capture investigations that are presented within this thesis, were carried out with Geant4, as described in Section 3.1. In the following, the generated MC data set and the applied analysis strategy is introduced. Further, the muon captures and the origin of the detected muon capture induced neutron signals are studied in detail.

10.3.1 Monte Carlo Data Set

The pre-recorded muon events from the virtual sphere, obtained from FLUKA simulations (see Section 6.1.1), were used as an input to Geant4 simulations of the MINIDEX muon capture setup. The pre-recorded muon events were simulated multiple times. However, each time a different random seed number was given to the Geant4 particle generator. The muons within the simulated pre-recorded muon events have a mean muon energy of (9.0 ± 0.2) GeV on a $0.5\,m^2$ horizontal plane directly above the setup. A MC data set corresponding to an effective MC lifetime of (168 ± 5) days has been generated. This lifetime was determined by dividing the number of energy depositions obtained by the simulation for the Big bot scintillator with the corresponding rate of measured energy depositions. The used measured (black) and simulated (red) spectrum can be seen in Fig. 10.5. For the normalisation, only measured and simulated energy depositions in the Big bot scintillator with energies above 6.5 MeV were taken into account. Furthermore, the measured spectrum is corrected for backgrounds not included in the simulation. These backgrounds were determined by fitting an exponential function (green) to the measured energy spectrum from 2.0 MeV to 6.5 MeV and extrapolating for energies >6.5 MeV. It can be seen that the resulting corrected experimental spectrum (blue) is in good agreement with the spectrum from simulation. The determined background subtracted experimental rate of energy depositions in the Big bot scintillator is $(28.5 \pm 0.9)\,s^{-1}$.

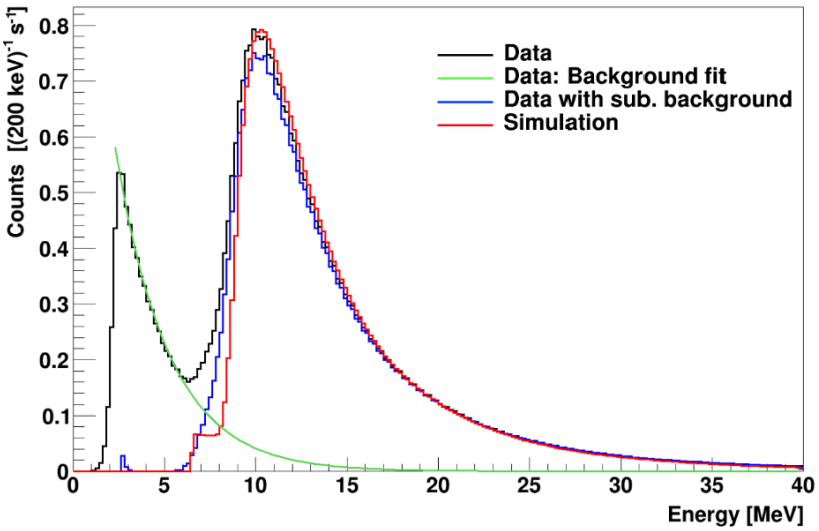

Figure 10.5: Measured and simulated energy spectrum of the Big bot scintillator. The black spectrum shows all measured energy depositions in the Big bot scintillator whereas the red spectrum represents the corresponding energy depositions predicted by the simulation. The background in the experimental spectrum is subtracted with the help of an exponential fit (green). The blue and the red spectrum are used to determine the effective MC lifetime of the generated MC data set. Taken from [126].

10.3.2 Muon Capture Tag

The identification of events with a muon capture tag in the MC data set is carried out in the same way as for the experimental data set (see Section 10.2.1). For the three scintillators on top of the setup, energy depositions above the experimentally determined energy cuts (see Table 10.1) and within a narrow ± 30 ns time window are requested. At the same time it is required that for the Big bot scintillator no energy above the corresponding energy cut and within ± 30 ns is detected. With these conditions 114072 muon capture tags have been identified in the MINIDEX muon capture MC data set.

10.3.3 Muon Capture Induced Neutron Signals

The number of simulated muon capture induced neutron signals are determined with a similar strategy as was used for the experimental data (see Section 10.2.2). In a time window from 7 μs to 1 ms after a muon capture tag 2.2 MeV gammas are collected in the germanium detectors. The simulation predicts that $> 94\,\%$ of all muon capture induced neutron signals can be detected within this time window. As any muon capture induced neutron signal can be identified unambiguously

in the simulation, no backgrounds have to be considered. The number of muon capture induced neutron signals can be directly determined from the events with a 2224.37 keV energy deposition in the germanium detectors. In total 52 muon capture induced neutron signals have been identified in the investigated MC data set.

10.3.4 Composition of Muon Capture Induced Neutron Signals

In order to study the background for the neutron production by muon captures on lead, the composition and the origin of the simulated muon capture induced neutron signals were investigated.

At first it was determined by simulations, what percentage of predicted muon capture induced neutron signals originate from actual muon captures. This is necessary as all kinds of particle interactions, not related to a muon capture, can lead to the production of muon-induced neutrons. For this purpose, two dedicated simulations were carried out. Both simulations use the same set of pre-recorded muon events (see Section 6.1.1) as input. However, for one of the simulations all particles produced directly by muon captures were removed from the simulation directly after their creation[1]. Thus, in this simulation all detected muon capture induced neutron signals have to originate from other sources than muon capture. Two MC data sets with effective MC lifetimes of (80 ± 3) days have been generated. In each of these data sets a number of ≈ 65000 muon capture tags was found. In the simulation with the muon capture process turned on, a number of 32 muon capture induced neutron signals were found. In contrast to this, in the simulation with the muon capture process turned off, only 1 muon captured induced neutron signal was observed. With these numbers it was determined that $(96.9\,^{+3.1}_{-4})$ % of all simulated muon capture induced neutron signals originate from muon captures within the setup.

In a second step it was determined on which material within the setup a muon was captured, in the case of a detected muon capture induced neutron signal. For this purpose, a further simulation was carried out. The emitted particles of 18085 muon capture processes, recorded for one of the simulations in the first step, were used as an input. In order to obtain a better statistic, the particles from these 18085 muon captures were simulated 200 times. Note that each time a different random seed number was given to the Geant4 particle

[1]The removed particles from this simulation correspond to 18085 muon capture processes. These particles were recorded and are used as an input to a further simulation.

generator. A total number of 4427 muon capture induced neutron signals were obtained, with 4278 resulting from muon captures on lead and 149 from muon captures on other materials within the setup (e.g. water or germanium). With the obtained numbers it was determined that (96.6 ± 0.3) % of all observed muon capture induced neutron signals originate from muon captures on lead. These findings are in agreement with expectations, as the muon capture rate depends in first order on Z^4, with Z representing the atomic number [71].

Combining the discussed simulation predictions for both steps, it can be concluded that $(93.6\,^{+3.0}_{-3.9})$ % of all detected muon capture induced neutron signals originate from muon captures on lead. Therefore, the muon capture setup and the corresponding analysis is suitable for the investigation of the neutron production by muon captures on lead.

10.3.5 Characteristics of Muon Capture Processes in MINIDEX

In Fig. 10.6(a) the simulated kinetic energy spectrum of muons at the position before entering the lead target of the setup is shown. In the spectrum only events

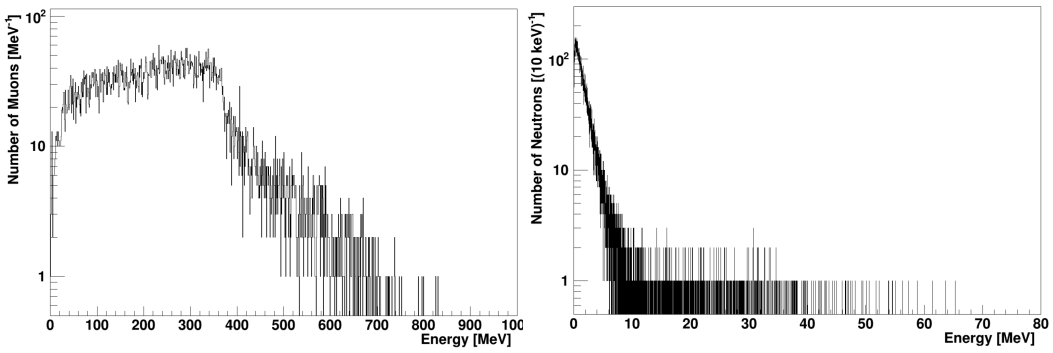

(a) (b)

Figure 10.6: Simulated kinetic energy spectrum of muons entering the lead target of the setup in (a). Only muons that are captured within the setup are considered. A mean muon energy of (238 ± 2) MeV and a maximal muon energy of ≈ 850 MeV was found. In (b) the simulated kinetic energy spectrum of neutrons emitted in muon captures within the setup, are shown. The vast majority of these neutrons originates from muon captures on lead. Taken from [126].

that are correlated to a muon capture tag and that undergo capture within the setup are shown. A mean energy of (238 ± 2) MeV and a maximal energy of

850 MeV is obtained for these muons. The shape of the spectrum is determined by the geometry of the setup as well as by the energy and the angular distribution of the simulated muons. As an example, a muon that passes through lead only and stops within the setup, can have higher energies than a muon that passes through parts of the water tank and stops within the setup. In Fig. 10.6(b) the kinetic energy spectrum of neutrons emitted in muon capture reactions within the setup, in the case of a muon capture tag, is shown. A mean energy of (2.07 ± 0.02) MeV, a maximal energy of ≈ 65 MeV and a most probable energy of (0.41 ± 0.06) MeV was found for these neutrons.

In Fig. 10.7 the average number of emitted particles in muon capture reactions is depicted. Also here, only events for which a muon capture tag was

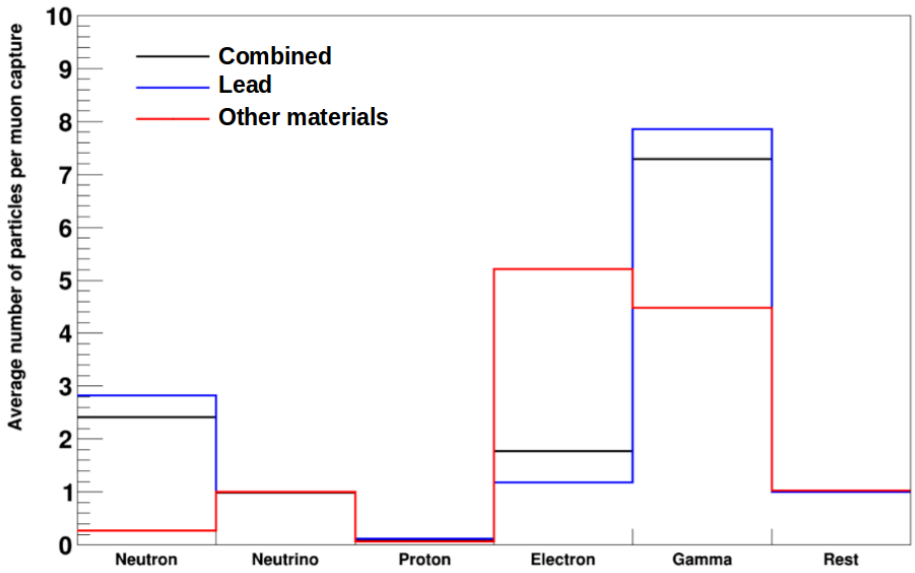

Figure 10.7: Average number of emitted particles per muon capture on different materials within the MINIDEX muon capture setup, as predicted by the simulation. In blue the numbers for a muon capture on lead are given, while in red the values for a muon capture on other materials inside the setup (e.g. water or germanium) are depicted. In the case of a muon capture on lead, on average 10.91 ± 0.04 times more neutrons are emitted compared to a capture on other materials within the setup. Also the average number of emitted particles for muon captures on any of the materials within the setup is given in black. Note, the majority of particles that are filled in the "Rest" column are recoiling nuclei. Adapted from [126].

found are considered. In blue the average numbers for the particles from muon captures on lead are given, while in red the numbers for muon captures on other

materials inside the setup (e.g. water or germanium) are presented. A significant difference in the number of emitted particles, especially for neutrons, is apparent. For muon captures on lead an average of 2.805 ± 0.002 neutrons are released. In the case of a muon capture on other materials inside the setup only 0.257 ± 0.001 neutrons are emitted on average.

10.4 Results and Discussion

In the following, the experimental and simulation results are compared and discussed. In order to be independent of the absolute muon flux in the laboratory, the number of muon capture induced neutron signals (measured and simulated) is evaluated as the muon capture induced neutron signal rate. The measured and simulated rates are therefore expressed in number of muon capture induced neutron signals per muon capture tag.

10.4.1 Experimental and Simulation Results

The determined results of the experimental and the MC data set, are summarised in Table 10.2. It can be seen that the experimental muon capture tag rate is by a

Table 10.2: Determined results of the experimental and the MC data set of the MINIDEX muon capture setup. The muon capture induced neutron signal rates are expressed in number of muon capture induced neutron signals per muon capture tag. The stated lifetime for the simulation is an effective lifetime.

	Experiment	Simulation
Lifetime [d]	158.83	(168 ± 5)
Number of muon capture tags	201747	114072
Number of muon capture induced neutron signals	$42\,^{+8}_{-6}\,(\text{stat})$	52
Muon capture tag rate $[10^{-3}\,\text{s}^{-1}]$	14.7	7.8
Muon capture induced neutron signal rate $[10^{-4}]$	$2.07\,^{+0.37}_{-0.30}\,(\text{stat})\,^{+0.14}_{-0.07}\,(\text{syst})$	$4.6 \pm 0.6\,(\text{stat}) \pm 0.6\,(\text{syst})$

factor of ≈ 2 higher than the one predicted by simulation. Further, it is observable that the measured muon capture induced neutron signal rate is underpredicted by the simulation by a factor of $2.2\,^{+0.8}_{-0.7}$ (combined statistical and systematical uncertainty). For the measured and simulated muon capture induced neutron signal rates a detailed investigation of systematic uncertainties has been carried out (see [126]). For the determined number of muon capture induced neutron signals in the experimental data set a signal to background ratio of $13\,^{+10}_{-5}$ has been obtained.

10.4.2 Discussion of Results

The observed discrepancies between the measured and the simulated muon capture tag rate as well as between the muon capture induced neutron signal rates were studied. It was investigated if the observed discrepancy between the rates is significant. For this purpose, the spectra of the individual scintillators from the experimental and the MC data set were compared. First, the spectra of events for which a muon capture tag was found were compared. As an example, the spectra of the Big top and the Tele2 scintillator are depicted in Fig. 10.8. All depicted spectra are normalised to the corresponding number of muon capture tags. It is apparent that the shape of the measured Big top scintillator spectrum does agree well with the simulated one, even though the corresponding muon capture tag rate is different. The same behaviour was found for the Big bot scintillator. In contrast to this, the measured spectrum of the Tele2 scintillator is not well reproduced by the simulation. Especially for energies in the range of (15 - 20) MeV the simulated spectrum differs significantly from the measured spectrum. An investigation of the Tele1 scintillator revealed a similar situation. Further, a comparison of all four scintillator spectra without any scintillator coincidence request confirmed these observations. In the case of the Big bot scintillator, the good agreement between the measured and the simulated spectrum can be found in Section 10.3.1.

The discussed comparisons show that the measured telescope scintillator spectra can not be reliably reproduced by the simulation. This indicates deficiencies in understanding the response of the telescope scintillators, which could result from non-linearities. As a consequence, a quantitative comparison of measured and simulated muon capture events is not possible. The observed difference between the measured and the predicted muon capture induced neutron signal rate has therefore to be treated carefully. In order to give a reliable feedback on the predictive power of Geant4 describing muon captures on lead, a more precise

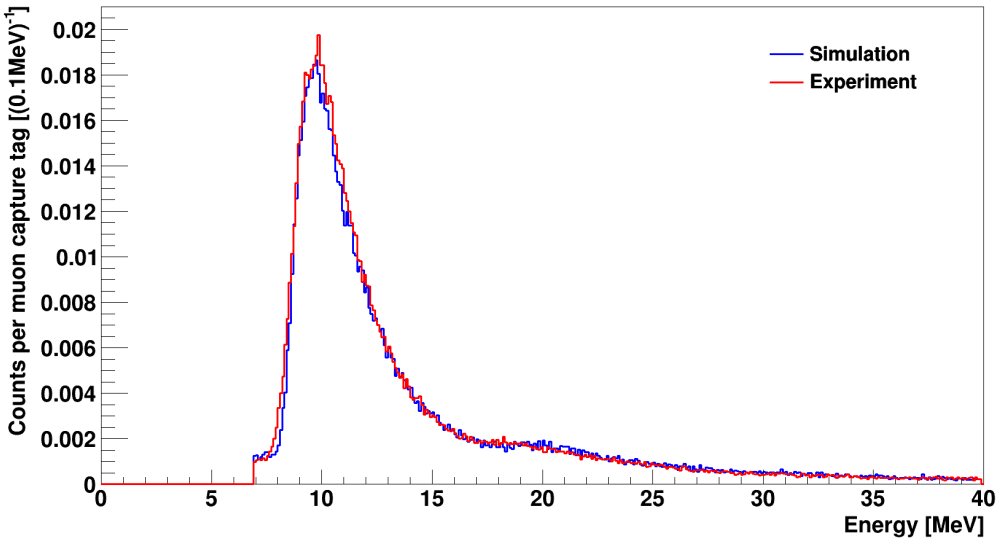

(a)

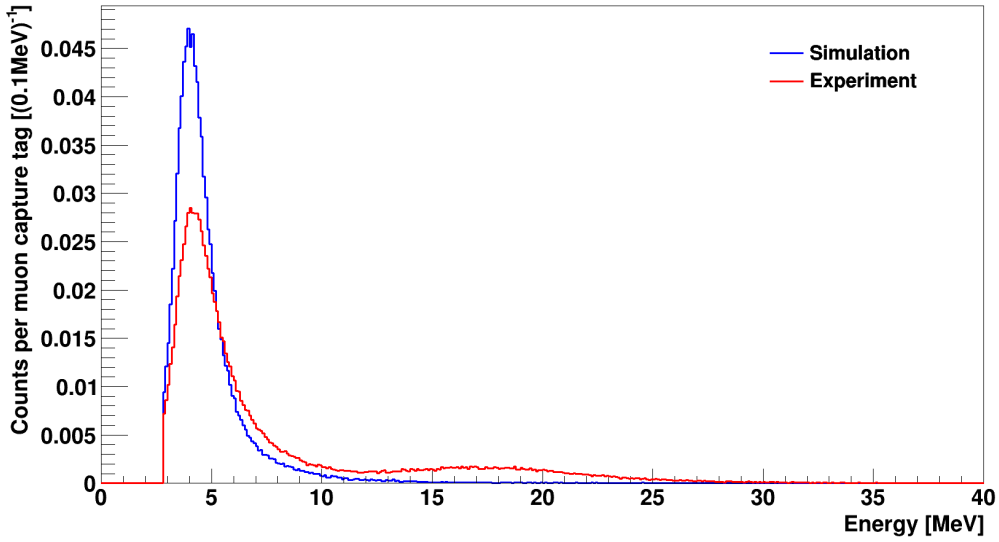

(b)

Figure 10.8: Measured and simulated energy spectrum of the Big top scintillator (top) and the Tele2 scintillator (bottom). Only events for which a muon capture tag was found are considered. All spectra are normalised to the corresponding number of muon capture tags.

understanding of the telescope scintillators is crucial. However, this is outside the scope of this thesis. Nevertheless, it should be pointed out that muon-induced neutrons, originating from muon capture on lead, were successfully measured. This clearly shows that the design of the MINIDEX muon capture setup and the corresponding analysis strategy is suitable for the study of neutrons induced by muon captures.

Chapter 11

Conclusions and Outlook

For future low-background experiments, like those searching for neutrinoless double beta decay or dark matter, a significant reduction as well as a reliable understanding of all relevant background contributions is crucial. Muon-induced neutrons are one of the more critical background sources. Current simulation tools do not consistently and reliably enough reproduce experimental findings of muon-induced neutrons. In order to improve the predictive power of MC tools, experimental data sets of muon-induced neutrons are needed. These data sets can be used to evaluate and gauge the MC tools. The MINIDEX runs discussed within this thesis provide such valuable experimental data sets for the high-Z materials lead and copper at a mean muon energy of $(8.7 \pm 0.2)\,\mathrm{GeV}$ and $(8.5 \pm 0.2)\,\mathrm{GeV}$, respectively. These materials are of special interest with regards to muon-induced neutrons, as they are often used in low-background experiments to shield the target detectors from ambient background radiation.

MINIDEX is located at the Tübingen Shallow Underground Laboratory, which provides a vertical shielding depth of $(13.2 \pm 0.8)\,\mathrm{mwe}$ at the position of the setup. Muon-induced neutrons are identified in MINIDEX by the detection of 2.2 MeV neutron capture gammas that follow tagged muons. From the measurement a rate of 2.2 MeV gammas, expressed in number of 10^{-5} 2.2 MeV gammas per muon tag, of $3.52 \pm 0.11\,(\mathrm{stat})\,^{+0.11}_{-0.05}\,(\mathrm{syst})$ and $1.27 \pm 0.14\,(\mathrm{stat})\,^{+0.04}_{-0.03}\,(\mathrm{syst})$ was determined for lead and copper, respectively. MC data sets of the MINIDEX setups were generated with the MC tool Geant4. The rate of 2.2 MeV neutron capture gammas for lead, obtained with Geant4, was found to be in good agreement with the measured rate. Based on this agreement, an external neutron yield of $(7.2\,^{+0.7}_{-0.6}) \cdot 10^{-5}\,\mathrm{g}^{-1}\,\mathrm{cm}^2$ neutrons per tagged muon was obtained for lead. Measured and simulated events for lead, for which more than one 2.2 MeV neutron capture gamma was detected for the same muon tag, were compared. Results of this comparison hint towards a too high multiplicity of neutrons directly emitted in muon-nuclear inelastic scattering reactions in Geant4. For copper the mea-

sured rate of 2.2 MeV neutron capture gammas was found to be overpredicted by (39 ± 28) % by Geant4. Taking this disagreement into account, an external neutron yield of $(2.1 \pm 0.4) \cdot 10^{-5}\,\mathrm{g}^{-1}\,\mathrm{cm}^2$ neutrons per tagged muon was determined for copper.

Results from a complementary simulation of the MINIDEX Run 2 setup with the FLUKA MC tool were used to cross-check the Geant4 results. The rate of 2.2 MeV neutron capture gammas for events with a lead muon tag, obtained with FLUKA, was also found to be in good agreement with the measured value. Geant4 and FLUKA predictions for muon interactions and the subsequent neutron production were compared in detail. Large differences for the neutron production in photo-nuclear inelastic scattering reactions between the two simulation codes were found. Further, significant discrepancies for the predicted rate and energy of neutrons, protons, pions and gammas, produced in muon-nuclear inelastic scattering reactions, have been observed. When taking into account earlier published observations [116, 118] it seems that photo-nuclear and muon-nuclear inelastic scattering reactions in lead (for muon energies at shallow depths) are imprecisely described by Geant4. Geant4 appears to underpredict the neutron production in photo-nuclear inelastic scattering reactions while at the same time overpredicts the neutron production in muon-nuclear inelastic scattering reactions. Furthermore, the study also hints towards a too high multiplicity of neutrons directly emitted in muon-nuclear inelastic scattering reactions in Geant4.

Muon-induced neutrons from muon captures on lead were successfully measured with MINIDEX and Geant4 predictions were compared to the experimental findings. In order to give a feedback on the reliability of Geant4 for simulating muon-induced neutrons from muon capture on lead, further investigations and improved experimental components are required.

From the discussed studies it can be concluded that the predictions of Geant4 with regards to muon-induced neutrons in high-Z materials should be treated carefully, especially at shallow underground depths. It is recommended to consider additional systematic uncertainties and to cross-check Geant4 predictions with complementary MC tools like FLUKA. In general, whenever radiation backgrounds from muon-nuclear or photo-nuclear inelastic scattering reactions are expected for an experiment, simulation predictions should be evaluated carefully.

MINIDEX is currently upgraded to allow for a simultaneous measurement of muon-induced neutrons from through-going and captured muons. For this purpose, additional scintillators are currently brought into service and will be soon installed in the MINIDEX setup, which is still located at the Tübingen Shallow

Underground Laboratory. The chosen targets for the next MINIDEX runs are lead, iron and aluminum, materials often used in low-background experiments. The long term plans of MINIDEX are to measure further materials relevant to low-background experiments, such as concrete and marble. Furthermore, it would be possible to move the MINIDEX setup to a different underground location. As the muon spectrum significantly depends on the shielding depth of an underground site, a different setup location provides the possibility to study muon-induced neutrons at a different mean muon energy.

List of Figures

List of Tables

Bibliography

[1] I. Abt et al., *The Muon-Induced Neutron Indirect Detection EXperiment, MINIDEX*, Astropart. Phys. **90** (2017) 1 – 13.

[2] A. Empl. Private communication.

[3] S. Chatrchyan et al., *Observation of a new boson at a mass of 125 GeV with the CMS experiment at the LHC*, Phys. Lett. B **716** no. 1, (2012) 30–61.

[4] G. Aad et al., *Observation of a new particle in the search for the Standard Model Higgs boson with the ATLAS detector at the LHC*, Phys. Lett. B **716** no. 1, (2012) 1–29.

[5] L. Wolfenstein, *Neutrino oscillations in matter*, Phys. Rev. D **17** (1978) 2369–2374.

[6] A. Giuliani and A. Poves, *Neutrinoless double-beta decay*, Adv. High Energy Phys. **2012** (2012) 38.

[7] E. Majorana, *A symmetric theory of electrons and positrons*, Soryushiron Kenkyu Electron. **63** no. 3, (1981) 149–162.

[8] F. T. Avignone III et al., *Double beta decay, Majorana neutrinos, and neutrino mass*, Rev. Mod. Phys. **80** no. 2, (2008) 481.

[9] S. M. Bilenky, *Neutrinoless double beta-decay*, Phys. Part. Nuclei **41** no. 5, (2010) 690–715.

[10] J. Suhonen and O. Civitarese, *Weak-interaction and nuclear-structure aspects of nuclear double beta decay*, Phys. Rep. **300** no. 3-4, (1998) 123–214.

[11] G. Benato, *Effective Majorana mass and neutrinoless double beta decay*, Eur. Phys. J. C **75** no. 11, (2015) 563.

[12] S. M. Bilenky and C. Giunti, *Neutrinoless Double-Beta Decay: a Probe of Physics Beyond the Standard Model*, Int. J. Mod. Phys. **A30** no. 04n05, (2015) 1530001.

[13] S. M. Bilenky et al., *Constraints from neutrino oscillation experiments on the effective Majorana mass in neutrinoless double β-decay*, Phys. Lett. B **465** no. 1-4, (1999) 193–202.

[14] S. M. Bilenky and C. Giunti, *Neutrinoless double-beta decay: a probe of physics beyond the standard model*, Int. J. Mod. Phys. A **30** no. 04n05, (2015) 1530001.

[15] A. S. Barabash, *Double-beta decay: Present status*, Phys. Atomic Nuclei **73** no. 1, (2010) 162–178.

[16] W. Rodejohann, *Neutrino-less Double Beta Decay and Particle Physics*, Int. J. Mod. Phys. E **20** no. 09, (2011) 1833–1930.

[17] S. Schönert et al., *The GERmanium Detector Array (GERDA) for the search of neutrinoless $\beta\beta$ decays of ^{76}Ge at LNGS*, Nucl. Phys. B Proc. Suppl. **145** (2005) 242 – 245.

[18] C. E. Aalseth et al., *The MAJORANA neutrinoless double-beta decay experiment*, Phys. Atomic Nuclei **67** no. 11, (2004) 2002–2010.

[19] C. Alduino et al., *First Results from CUORE: A Search for Lepton Number Violation via $0\nu\beta\beta$ Decay of* ^{130}Te, Phys. Rev. Lett. **120** (2018) 132501.

[20] M. Auger et al., *Search for Neutrinoless Double-Beta Decay in ^{136}Xe with EXO-200*, Phys. Rev. Lett. **109** (2012) 032505.

[21] A. Gando et al., *Limit on Neutrinoless $\beta\beta$ Decay of ^{136}Xe from the First Phase of KamLAND-Zen and Comparison with the Positive Claim in ^{76}Ge*, Phys. Rev. Lett. **110** (2013) 062502.

[22] S. Biller et al., *A New Technique to Load* ^{130}Te *in Liquid Scintillator for Neutrinoless Double Beta Decay Experiments*, J. Phys. Conf. Ser. **888** no. 1, (2017) 012084.

[23] A. Basharina-Freshville, *Search for the neutrinoless double beta decay of ^{100}Mo with the NEMO3 detector and calorimeter research and development for the SuperNEMO experiment.* Ph.D. thesis, UCL (University College London), 2012. `http://discovery.ucl.ac.uk/1343630/1/1343630.pdf`.

[24] R. Arnold et al., *Limits on different majoron decay modes of ^{100}Mo and ^{82}Se for neutrinoless double beta decays in the NEMO-3 experiment*, Nucl. Phys. A **765** no. 3, (2006) 483 – 494.

[25] R. Arnold et al., *Measurement of the $2\nu\beta\beta$ decay half-life of ^{150}Nd and a search for $0\nu\beta\beta$ decay processes with the full exposure from the NEMO-3 detector*, Phys. Rev. D **94** (2016) 072003.

[26] Zsigmond, A. J. for the GERDA collaboration, Talk at the Neutrino 2018, Heidelberg, *New results from GERDA Phase II*, June, 2018.

[27] A. Gando et al., *Search for Majorana Neutrinos Near the Inverted Mass Hierarchy Region with KamLAND-Zen*, Phys. Rev. Lett. **117** (2016) 082503.

[28] R. Arnold et al., *Results of the search for neutrinoless double-β decay in ^{100}Mo with the NEMO-3 experiment*, Phys. Rev. D **92** (2015) 072011.

[29] N. Abgrall et al., *The Large Enriched Germanium Experiment for Neutrinoless Double Beta Decay (LEGEND)*, AIP Conf. Proc. **1894** no. 1, (2017) 020027.

[30] J. B. Albert et al., *Sensitivity and Discovery Potential of nEXO to Neutrinoless Double Beta Decay*, Phys. Rev. **C97** no. 6, (2018) 065503.

[31] R. Arnold et al., *Probing New Physics Models of Neutrinoless Double Beta Decay with SuperNEMO*, Eur. Phys. J. **C70** (2010) 927–943.

[32] F. Zwicky, *Die rotverschiebung von extragalaktischen nebeln*, Helv. Phys. Acta **6** (1933) 110–127.

[33] K. G. Begeman et al., *Extended rotation curves of spiral galaxies: Dark haloes and modified dynamics*, Mon. Not. Roy. Astron. Soc. **249** no. 3, (1991) 523–537.

[34] C. Tortora, P. Jetzer, and N. R. Napolitano, *Dark matter and alternative recipes for the missing mass*, J. Phys. Conf. Ser. **354** no. 1, (2012) 012021.

[35] J. R. Brownstein and J. W. Moffat, *The Bullet Cluster 1E0657-558 evidence shows modified gravity in the absence of dark matter*, Mon. Not. Roy. Astron. Soc. **382** no. 1, (2007) 29–47.

[36] D. Clowe et al., *A Direct Empirical Proof of the Existence of Dark Matter*, Astrophys. J. Lett. **648** no. 2, (2006) L109. `http://stacks.iop.org/1538-4357/648/i=2/a=L109`.

[37] P. Noterdaeme et al., *The evolution of the cosmic microwave background temperature-measurements of TCMB at high redshift from carbon monoxide excitation*, Astron. Astrophys. **526** (2011) L7.

[38] J. C. Mather et al., *Measurement of the cosmic microwave background spectrum by the COBE FIRAS instrument*, Astrophys. J. **420** (1994) 439–444.

[39] G. Hinshaw et al., *Nine-year Wilkinson Microwave Anisotropy Probe (WMAP) observations: cosmological parameter results*, Astrophys. J. Suppl. Ser. **208** no. 2, (2013) 19.

[40] P. A. R. Ade et al., *Planck 2013 results. XVI. Cosmological parameters*, Astron. Astrophys. **571** (2014) A16.

[41] H. Baer et al., *Dark matter production in the early Universe: beyond the thermal WIMP paradigm*, Phys. Rept. **555** (2014) 1–60.

[42] M. L. Perl et al., *The search for stable, massive, elementary particles*, Int. J. Mod. Phys. A **16** no. 12, (2001) 2137–2164.

[43] K. Freese et al., *Colloquium: Annual modulation of dark matter*, Rev. Mod. Phys. **85** (2013) 1561–1581.

[44] V. Sanglard et al., *Final results of the EDELWEISS-I dark matter search with cryogenic heat-and-ionization Ge detectors*, Phys. Rev. D **71** (2005) 122002.

[45] G. Angloher et al., *Results from 730 kg days of the CRESST-II Dark Matter search*, Eur. Phys. J. C **72** no. 4, (2012) 1971.

[46] E. Aprile et al., *Dark Matter Results from 225 Live Days of XENON100 Data*, Phys. Rev. Lett. **109** (2012) 181301.

[47] P. Agnes et al., *First results from the DarkSide-50 dark matter experiment at Laboratori Nazionali del Gran Sasso*, Phys. Lett. B **743** (2015) 456 – 466.

[48] R. Bernabei and other, *New results from DAMA/LIBRA*, Eur. Phys. J. C **67** no. 1, (2010) 39–49.

[49] J. Beringer et al., *Review of Particle Physics*, Phys. Rev. D **86** (2012) 010001.

[50] D. S. Akerib and others., *First Results from the LUX Dark Matter Experiment at the Sanford Underground Research Facility*, Phys. Rev. Lett. **112** (2014) 091303.

[51] T. M. Undagoitia and L. Rauch, *Dark matter direct-detection experiments*, J. Phys. G **43** no. 1, (2016) 013001. `http://stacks.iop.org/0954-3899/43/i=1/a=013001`.

[52] AIP Publishing, *The large enriched germanium experiment for neutrinoless double beta decay (LEGEND)*, vol. 1894. 2017.

[53] T. J. Dunai, *Cosmogenic nuclides: principles, concepts and applications in the earth surface sciences*. Cambridge University Press, 2010.

[54] M. M. Block and F. Halzen, *Forward hadronic scattering at 7 TeV: An update on predictions for the LHC*, Phys. Rev. D **83** (2011) 077901.

[55] C. Patrignani, P. D. Group, et al., *Review of particle physics*, Chin. Phys. C **40** no. 10, (2016) 100001.

[56] *Fermi acceleration in astrophysical jets*. Springer Netherlands, 2007.

[57] P. Blasi, *The origin of galactic cosmic rays*, Astron. Astrophys. Rev. **21** no. 1, (2013) 70.

[58] A. Abramowski et al., *Acceleration of petaelectronvolt protons in the Galactic Centre*, Nature **531** (2016) 476.

[59] V. S. Ptuskin et al., *Diffusion and drift of very high energy cosmic rays in galactic magnetic fields*, Astron. Astrophys. **268** (1993) 726–735. http://adsabs.harvard.edu/full/1993A%26A...268..726P.

[60] "Cosmic Rays - Extensive Air Showers." https://www.hawc-observatory.org/science/cosmicrays.php. Webpage.

[61] C. Costa, *The prompt lepton cookbook*, Astropart. Phys. **16** no. 2, (2001) 193 – 204.

[62] M. Ambrosio et al., *Vertical muon intensity measured with MACRO at the Gran Sasso laboratory*, Phys. Rev. D **52** (1995) 3793–3802.

[63] M. Aglietta et al., *Neutrino-induced and atmospheric single-muon fluxes measured over five decades of intensity by LVD at Gran Sasso Laboratory*, Astropart. Phys. **3** no. 4, (1995) 311 – 320.

[64] K. Nakamura and P. D. Group, *Rev. Part. Phys.*, J. Phys. G **37** no. 7A, (2010) 075021.

[65] A. G. Bogdanov et al., *Geant4 simulation of production and interaction of muons*, IEEE Trans. Nucl. Sci. **53** no. 2, (2006) 513–519.

[66] A. S. Malgin and O. G. Ryazhskaya, *Neutrons from muons underground*, Phys. Atomic Nuclei **71** no. 10, (2008) 1769–1781.

[67] O. M. Horn, *Simulations of the muon-induced neutron background of the EDELWEISS-II experiment for Dark Matter search.* Ph.D. thesis, University of Karlsruhe, 2007. http://bibliothek.fzk.de/zb/berichte/FZKA7391.pdf.

[68] D.-M. Mei and A. Hime, *Muon-induced background study for underground laboratories*, Phys. Rev. D **73** (2006) 053004.

[69] Y.-F. Wang et al., *Predicting neutron production from cosmic-ray muons*, Phys. Rev. D **64** (2001) 013012.

[70] J. A. Formaggio and C. Martoff, *Backgrounds To Sensitive Experiments Underground*, Annu. Rev. Nucl. Part. Sci. **54** no. 1, (2004) 361–412.

[71] D. F. Measday, *The nuclear physics of muon capture*, Phys. Rep. **354** no. 4, (2001) 243 – 409.

[72] H. M. Kluck, *Measurement of the Cosmic-Induced Neutron Yield at the Modane Underground Laboratory.* Ph.D. thesis, KIT, Karlsruhe, 2013.

[73] D. Hilscher et al., *Neutron production by hadron-induced spallation reactions in thin and thick Pb and U targets from 1 to 5 GeV*, Nucl. Instrum. Methods Phys. Res. **414** no. 1, (1998) 100 – 116.

[74] R. Brugnera and A. Garfagnini, *Status of the GERDA experiment at the Laboratori Nazionali del Gran Sasso*, Adv. High Energy Phys. **2013** (2013) 15.

[75] G. Angloher et al., *Results on low mass WIMPs using an upgraded CRESST-II detector*, Eur. Phys. J. C **74** no. 12, (2014) 3184.

[76] K.-H. Ackermann et al., *The GERDA experiment for the search of $0\nu\beta\beta$ decay in ^{76}Ge*, Eur. Phys. J. C **73** no. 3, (2013) 2330.

[77] *Status of the GERDA experiment aimed to search for neutrinoless double beta decay of 76Ge.* 2008. `https://inspirehep.net/record/805956/files/arXiv:0812.4194.pdf`.

[78] H. Kraus et al., *EURECA*, PoS **IDM2010** (2011) 109.

[79] L. Pandola et al., *Monte Carlo evaluation of the muon-induced background in the GERDA double beta decay experiment*, Nucl. Instr. Meth. Phys. Res. A **570** no. 1, (2007) 149 – 158.

[80] I. Barabanov et al., *Cosmogenic activation of germanium and its reduction for low background experiments*, Nucl. Instrum. Methods Phys. Res. B **251** no. 1, (2006) 115 – 120.

[81] A. Muenster, *Absolute α - Radioactivity Determination of Scintillating $CaWO_4$ Crystals for Direct Dark Matter Search*, Master's thesis, Technical University Munich, 2013.

[82] M. Agostini et al., *Results on Neutrinoless Double-β Decay of ^{76}Ge from Phase I of the GERDA Experiment*, Phys. Rev. Lett. **111** (2013) 122503.

[83] A. N. Annenkov et al., *Development of $CaMoO_4$ crystal scintillators for a double beta decay experiment with ^{100}Mo*, Nucl. Instrum. Methods Phys. Res. A **584** no. 2, (2008) 334 – 345.

[84] Q. R. Ahmad et al., *Direct Evidence for Neutrino Flavor Transformation from Neutral-Current Interactions in the Sudbury Neutrino Observatory*, Phys. Rev. Lett. **89** (2002) 011301.

[85] D. Budjas et al., *Gamma-ray spectrometry of ultra low levels of radioactivity within the material screening program for the GERDA experiment*, Appl. Radiat. Isot. **67** no. 5, (2009) 755 – 758.

[86] G. Heusser, *Low-Radioactivity Background Techniques*, Annu. Rev. Nucl. Part. Sci. **45** no. 1, (1995) 543–590.

[87] M. Boswell et al., *MaGe-a Geant4-based Monte Carlo application framework for low-background germanium experiments*, IEEE Trans. Nucl. Sci. **58** no. 3, (2011) 1212–1220.

[88] S. Agostinelli et al., *GEANT4: A Simulation toolkit*, Nucl. Instrum. Meth. **A506** (2003) 250–303.

[89] "Geant4 Collaboration, Reference Physics Lists." `https://geant4.web.cern.ch/node/155`.

[90] D. Wright, "Shielding Physics List Description." Website, 2017-12-07. `http://www.slac.stanford.edu/comp/physics/geant4/slac_physics_lists/shielding/physlistdoc.html`.

[91] "Geant4 Collaboration, Use Cases - Reference Physics Lists." `https://geant4.web.cern.ch/node/302`.

[92] Geant4 Collaboration, *Muon-nuclear Interactions*, 2018. `http://geant4-userdoc.web.cern.ch/geant4-userdoc/UsersGuides/PhysicsReferenceManual/html/photolepton_hadron/muonNuclear.html`. Physics reference manual, Webpage.

[93] Geant4 Collaboration, *Gamma-nuclear Interactions*, 2018. `http://geant4-userdoc.web.cern.ch/geant4-userdoc/UsersGuides/PhysicsReferenceManual/html/photolepton_hadron/gammaNuclear.html`. Physics reference manual, Webpage.

[94] R. Kneißl et al., *Muon-induced neutrons in lead and copper at shallow depth*, `arXiv:1901.05309 [physics.ins-det]`.

[95] A. Ferrari et al., *FLUKA: A multi-particle transport code (Program version 2005)*,.

[96] T. T. Böhlen et al., *The FLUKA Code: Developments and Challenges for High Energy and Medical Applications*, Nuclear Data Sheets **120** (2014) 211 – 214.

[97] G. V. Gorshkov and V. A. Zyabkin, *Production of neutrons in Pb, Cd, Fe, and Al under the influence of cosmic-ray muons at a depth of 150 m water equivalent*, Sov. J. Nucl. Phys. **7** (1968) 470–474.

[98] L. Reichhart et al., *Measurement and simulation of the muon-induced neutron yield in lead*, Astropart. Phys. **47** (2013) 67–76.

[99] S. Abe et al., *Production of radioactive isotopes through cosmic muon spallation in KamLAND*, Phys. Rev. C **81** (2010) 025807.

[100] M. o. Adams, *Nuclear Decay Following Deep Inelastic Scattering of 470 GeV Muons*, Phys. Rev. Lett. **74** (1995) 5198–5201.

[101] V. Chazal et al., *Investigations of fast neutron production by 190 GeV/c muon interactions on different targets*, Nucl. Instrum. Methods Phys. Res. A **490** no. 1, (2002) 334 – 343.

[102] L. Bergamasco, S. Costa, and P. Picchi, *Experimental results on neutron production by muons at 4300 m w.e.*, Il Nuovo Cimento A **13** no. 2, (1973) 403–412.

[103] F. Boehm et al., *Neutron production by cosmic-ray muons at shallow depth*, Phys. Rev. D **62** (2000) 092005.

[104] A. Lindote et al., *Simulation of neutrons produced by high-energy muons underground*, Astropart. Phys. **31** no. 5, (2009) 366 – 375.

[105] A. S. Malgin, *Phenomenology of muon-induced neutron yield*, Phys. Rev. C **96** (2017) 014605.

[106] A. Malgin and A. S. Malgin, *Phenomenology of muon-induced neutron yield*, Phys. Rev. **C96** no. 1, (2017) 014605.

[107] A. Empl et al., *A Fluka study of underground cosmogenic neutron production*, J. Cosmol. Astropart. Phys. **2014** no. 08, (2014) 064.

[108] L. Bergamasco, *Experimental results on the pion and neutron production by muons at 60 and 110 m w.e.*, Il Nuovo Cimento B **66** no. 1, (1970) 120–128.

[109] F. P. An et al., *Cosmogenic neutron production at Daya Bay*, Phys. Rev. **D97** no. 5, (2018) 052009.

[110] R. Hertenberger, M. Chen, and B. L. Dougherty, *Muon-induced neutron and pion production in an organic liquid scintillator at a shallow depth*, Phys. Rev. C **52** (1995) 3449–3459.

[111] G. Bellini et al., *Cosmogenic Backgrounds in Borexino at 3800 m water-equivalent depth*, J. Cosmol. Astropart. Phys. **2013** no. 08, (2013) 049.

[112] R. Lemrani et al., *Low-energy neutron propagation in MCNPX and GEANT4*, Nucl. Instrum. Methods Phys. Res. A **560** no. 2, (2006) 454 – 459.

[113] H. M. Araujo et al., *Muon-induced neutron production and detection with GEANT4 and FLUKA*, Nucl. Instrum. Meth. **A545** (2005) 398–411.

[114] M. Selvi, *The LVD Core Facility: A Study of LVD as muon veto and active shielding for dark matter experiments*, PoS **IDM2008** (2008) 081, `arXiv:0811.2884 [hep-ex]`.

[115] *FLUKA: Predictive power for cosmogenic backgrounds*, vol. 1672. 2015.

[116] W. Luo et al., *A data-based photonuclear simulation algorithm for determining specific activity of medical radioisotopes*, Nucl. Sci. Tech. **27** no. 5, (2016) 113.

[117] "Exchange format experimental nuclear reaction database." `https://www-nds.iaea.org/exfor/exfor.htm`.

[118] L. Quintieri et al., *Quantification of the validity of simulations based on Geant4 and FLUKA for photo-nuclear interactions in the high energy range*, EPJ Web Conf. **153** (2017) 06023.

[119] "International Atomic Energy Agency - Nuclear Data Services." https://www-nds.iaea.org.

[120] Q. Du et al., *Direct measurement of neutrons induced in lead by cosmic muons at a shallow underground site*, Astropart. Phys. **102** (2018) 12 – 24.

[121] M. Palermo, *The Muon-Induced Neutron Indirect-Detection EXperiment: MINIDEX*. Ph.D. thesis, Ludwig Maximilian University of Munich, 2016. http://nbn-resolving.de/urn:nbn:de:bvb:19-195759.

[122] I. A. E. Agency, *Database Of Prompt Gamma Rays From Slow Neutron Capture For Elemental Analysis*, 2007. http://www-pub.iaea.org/MTCD/publications/PDF/Pub1263_web.pdf.

[123] "Crystal Scintillators." https://www.crystals.saint-gobain.com/products/crystal-scintillation. Webpage.

[124] Saint-Gobain Ceramics & Plastics, *Premium Plastic Scintillators*, Aug, 2016. https://www.crystals.saint-gobain.com/sites/imdf.crystals.com/files/documents/sgc-bc400-404-408-412-416-data-sheet.pdf. Data sheet.

[125] ET Enterprises, *9266B series data sheet*, Aug, 2010. http://et-enterprises.com/images/data_sheets/9266B.pdf. Data sheet.

[126] O. Plaul, *Measurement of Neutrons from Muon Capture on Lead with MINIDEX*, Master's thesis, Technical University Munich, 2018.

[127] Mirion Technologies, *Germanium Detectors*, Sep, 2016. https://www.mirion.com/products/germanium-detectors. Data sheet.

[128] Mirion Technologies, *Extended Range Coaxial Ge Detectors*, Nov, 2016. https://www.mirion.com/products/xtra-extended-range-coaxial-ge-detectors. Data sheet.

[129] Mirion Technologies, *Cryo-Pulse 5 Plus*, Sep, 2017. https://www.mirion.com/products/cryo-pulse-5-plus-electrically-refrigerated-cryostat. Data sheet.

[130] FAST ComTex, *Model NHQ202M to NHQ206L Dual High Voltage Power Supplies*. https://www.fastcomtec.com/fwww/datashee/hv/nhq2.pdf. Data sheet.

[131] struck innovative systems, *SIS3316 Family - 16 Channel VME Digitizer - 16 Channel Desktop Digitizer*. http://www.struck.de/sis3316-2014-03-20.pdf. Last updated: 20th March 2014.

[132] Super Micro Computer, *SuperServer 5018D-MTF, Specifications*. http://www.supermicro.com/products/system/1u/5018/SYS-5018D-MTF.cfm. Webpage.

[133] "AquaPlumb - Water Level Sensors." https://www.vegetronix.com/Products/AquaPlumb/. Webpage.

[134] D. Wetterdienst, "Archiv Monats- und Tageswerte." https://www.dwd.de/DE/leistungen/klimadatendeutschland/klarchivtagmonat.html.

[135] G. Battistoni et al., *FLUKA as a new high energy cosmic ray generator*, Nucl. Instrum. Methods Phys. Res. A **626 - 627** (2011) S191 – S192.

[136] I. Abt et al., *Neutron interactions as seen by a segmented germanium detector*, Eur. Phys. J. A **36** no. 2, (2008) 139–149.

[137] L. Vanhoefer, *Limitations of Rare Event HPGe Experiments due to Muon-Induced Neutron Background*. Ph.D. thesis, Technical University of Munich, 2018.

[138] L. Janossy, *Rate of n-fold Accidental Coincidences*, Nature **153** (1944) 165.

[139] Mirion Technologies. Email to author by H. Krueger, Sep, 2018.

[140] International Atomic Energy Agency, *Neutron Fluence Measurements*. No. 107 in Technical Reports Series. Vienna, 1970. http://www-pub.iaea.org/books/IAEABooks/1206/Neutron-Fluence-Measurements.

Acknowledgements

Many people helped me during my time at Max Planck Institute for Physics to accomplish my PhD and to successfully finish this thesis. Here I wanna take the opportunity to thank all of them.

First of all I want to thank my supervisor and mentor Dr. Béla Majorovits for letting me join and work in the GERDA group. I honestly have to admit, the subject I was working on was most of the time very interesting and promising. I have learned quite a lot over the last years, not only in physics but in all kinds of subjects. Thanks for the great support, the valuable guidance and the many fruitful discussions.

I would also like to thank the second referee of my thesis, Prof. Dr. L. Oberauer as well as the chairman of my PhD thesis defence, Prof. Dr. A. Ibarra.

A special person I would like to thank is Toni. I totally appreciated working with you over the last years. You contributed so much to the content and especially the success of this thesis and my PhD. Your kindness and willingness are outstanding and I am happy that we have become friends.

My sincere thank you to all members of the GERDA, LEGEND and MADMAX groups as well as the GERDA collaboration. Especially Anna, Barbara, Chris, Connor, Felix, Heng-Ye, Laura, Lukas, Lucia, Martin, Peter and Stefan. It was a lot of fun spending time with you guys. A special thanks goes to Jonny and Qiang for the nice time and all the great things we did together. Also thanks to my master student Oliver. I think we both had a really good time and learned quite a lot during the year you spend at our institute. I wanna thank Xiang and Oliver S. for their nice support, the good discussions and all the things they taught me. I also learned quite a lot from Dr. Iris Abt. Thanks for this as well.

Special thanks goes to Béla, Anna and Katharina for reading my thesis and their valuable and helpful comments. You definitely increased the quality of this thesis.

I would like to thank the groups of Prof. Dr. Josef Jochum and Prof. Dr. Peter Grabmayr for providing us space and help in their underground laboratory at the University of Tübingen. My special thanks goes to Igor for his relentless support and hospitality over the last years.

Also I wanna thank all my friends outside the MPP for their mental support over the last years. This especially includes my best friends in Munich, Chris, Dominik, Markus, Stephan, Tobias and Vanessa, which actually supported me quite a lot.

Without the mental and financial support of my parents during my whole life, accomplishing a PhD would not have been possible. I am deeply grateful to have them. At the end I would like to take the possibility to thank the most important person, Katharina, my girlfriend and the best friend I could imagine. With you anything is achievable in life.